OCCASION

This publication has been made available to the public on the occasion of the 50th anniversary of the United Nations Industrial Development Organisation.

DISCLAIMER

This document has been produced without formal United Nations editing. The designations employed and the presentation of the material in this document do not imply the expression of any opinion whatsoever on the part of the Secretariat of the United Nations Industrial Development Organization (UNIDO) concerning the legal status of any country, territory, city or area or of its authorities, or concerning the delimitation of its frontiers or boundaries, or its economic system or degree of development. Designations such as "developed", "industrialized" and "developing" are intended for statistical convenience and do not necessarily express a judgment about the stage reached by a particular country or area in the development process. Mention of firm names or commercial products does not constitute an endorsement by UNIDO.

FAIR USE POLICY

Any part of this publication may be quoted and referenced for educational and research purposes without additional permission from UNIDO. However, those who make use of quoting and referencing this publication are requested to follow the Fair Use Policy of giving due credit to UNIDO.

CONTACT

Please contact publications@unido.org for further information concerning UNIDO publications.

For more information about UNIDO, please visit us at www.unido.org

UNITED NATIONS INDUSTRIAL DEVELOPMENT ORGANIZATION
Vienna International Centre, P.O. Box 300, 1400 Vienna, Austria
Tel: (+43-1) 26026-0 · www.unido.org · unido@unido.org

Urgent

16158

Distr.
LIMITED

IPCT.19 (SPEC.)
3 March 1987

ENGLISH

UNITED NATIONS
INDUSTRIAL DEVELOPMENT ORGANIZATION

SOLAR CELL MATERIALS AND FABRICATION TECHNOLOGIES*

prepared by

K. W. Böer **

31

---

* This document has been reproduced without formal editing.

** Professor, University of Delaware, Newark, Delaware 19716, USA

1 Abstract

A review is given of commercially interesting solar cells and such other cells which may acquire commercial interest in the near future. The review contains a summary of the relevant theory, the status of the present technology with attention to critical material parameters, cell and panel processing, achieved efficiency and other performance data, economical aspects and status of the present commercialization. It also discusses emerging technologies and research and development trends. It includes listings of R & D centers and industries in the USA and several other countries. The review gives examples of commercial applications and summarizes the recent market development.

Table of Contents

1 Introduction

The direct conversion of light into electric energy through photovoltaic effect, known in semiconductors for more than a century[1], became of interest for commercial solar energy conversion with the invention of the higher efficiency (6%) Si and CdS/Cu_2S solar cells[2,3] in 1954 and their first successful deployment in satellites, starting with Vanguard I in 1957. This was followed in rapid succession with larger and larger, finally multi kW-panels (Fig. 1), made mostly from Si single crystals with typically ~10% panel efficiency, which was reached in 1963 and maintained for the next decade with best cell efficiencies near 12%. The production cost[4] of these panels dropped from >500 $/W in 1958 to ~100 $/W in 1971.

At that time there was little commercial interest except for a modest space program market* of $\lesssim$100 kW/y. The only other solar cell materials with promise were single crystal GaAs of slightly higher efficiency flown by some USSR space crafts and the CdS/Cu_2S polycrystalline thin-film cell, further developed by the Clevite-group[5]. A more extensive commercial use† of GaAs was impeded since it is substantially more expensive than Si. The initial development of CdS/Cu_2S by the Clevite corporation was discontinued because of cell degradation and its incomplete understanding.

As a result of comprehensive studies sponsored by NSF and NASA and by the National Academy of Sciences, it became evident in 1972 that a substantial reduction in production cost to approach 1$/W‡ and an increase of efficiencies beyond 10% for thin-film and beyond 20% for single crystal cells were feasible[6]. With significant government support mainly in the USA, Japan, and Western Europe, rapid progress was made and essentially all technical goals set in 1972 have been achieved and surpassed (thin-film efficiency 12% for CdS/$CuInSe_2$ and 13% for a-Si, single crystal AM1 efficiency 23% for Si and 23% for AlGaAs/GaAs; recent Si-cells in concentrators have achieved 27% conversion efficiency)[7]. The economic goal (updated for competing with the increased electric energy generation cost and inflationary devaluation of the dollar) seems to be within reach and large quantities of solar panels sell currently for ~5 $/W. The life expectancies of better Si-panels (conservatively estimated) are well in excess of 20 years.

---

* Up to 1971 approximately 600 US and 400 Soviet spacecrafts were powered with solar cells[8].

† Except for use in concentrators.

‡ Here and in many other cited publications the reference is made to the US dollar, which however, because of inflation has a sliding value. In order to assist in comparison we have added a table giving the annual inflation rate and the cumulative changes of the $ value from 1974 to 1985.

Table 1

Year	Average Annual Inflation Rate (%)	Cumulative	Year	Average Annual Inflation Rate (%)	Cumulative
1974	9.7	1.000	1980	9.3	1.561
1975	9.3	1.097	1981	9.4	1.706
1976	5.2	1.205	1982	6.0	1.808
1977	5.8	1.264	1983	4.2	1.970
1978	7.4	1.337	1984	3.6	2.049
1979	8.7	1.436	1985	4.0 (est.)	2.132

Source: Department of Commerce, Survey of Current Business, June 1985.

Figure 1: Space applications of solar cells and history of progress (Hughes).

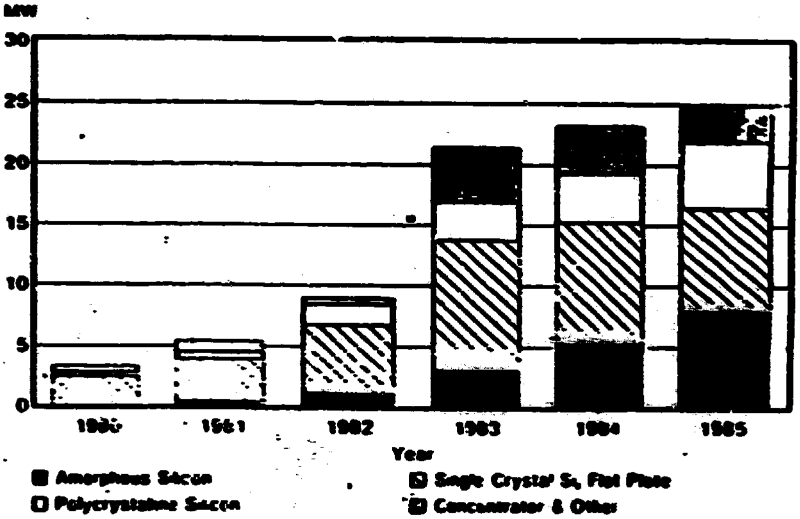

Figure 2: World shipment of photovoltaic devices (SERI in review, April 1986).

Further projections suggest single crystal efficiencies in excess of 25% of AM1 and above 30% in concentrators, thin-film efficiencies >15%, life expectancies >25 years (for single crystal cells) and production cost below 2 $/W for single crystal *panels* and below 1 $/W for thin-film *panels* in 1986 dollars.

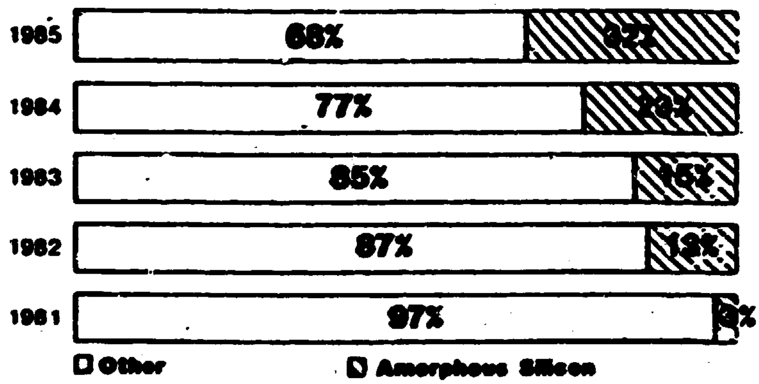

Figure 3: World market share of amorphous silicon solar cells (SERI in review, April 1986).

At the present time solar cell systems compete economically with diesel-driven generators in remote applications (see Sec. 3.5). With the above given projections large scale terrestrial solar energy conversion in conjunction with power utilities has a very realistic potential beyond the presently already available markets, which have absorbed in excess of 80MW (Fig. 2) and produced revenues in excess of 1B$ during the last 5 years. Most of this market was supplied with crystalline Si solar cells, however, with a substantially increasing market share of α-Si (Fig. 3).

In order to assist in judgment of possible further cell development we will start this review by a short summary of the theory of solar cells. Then a review of recent achievements in the research and development of the more promising types of solar cells is given with an overview of the present production methods and deployment examples of solar cells, panels and conversion systems, including an evaluation of present commercialization and a listing of current producers. We will close this review with some prospects for developing countries and long-term implications.

2 Solar Cell Types and Materials

The photovoltaic effect in modern solar cells is based on the separation of excess carriers in the built-in field of a pn-junction within a semiconductor (Fig. 4). The excess (over thermal equilibrium) carriers are created by absorbed sunlight. Their separation creates a photo-emf which makes the solar cell act like a battery and permits through an external circuit the extraction of almost all of these excess carriers (the collection efficiency approaches 1 in better cells).

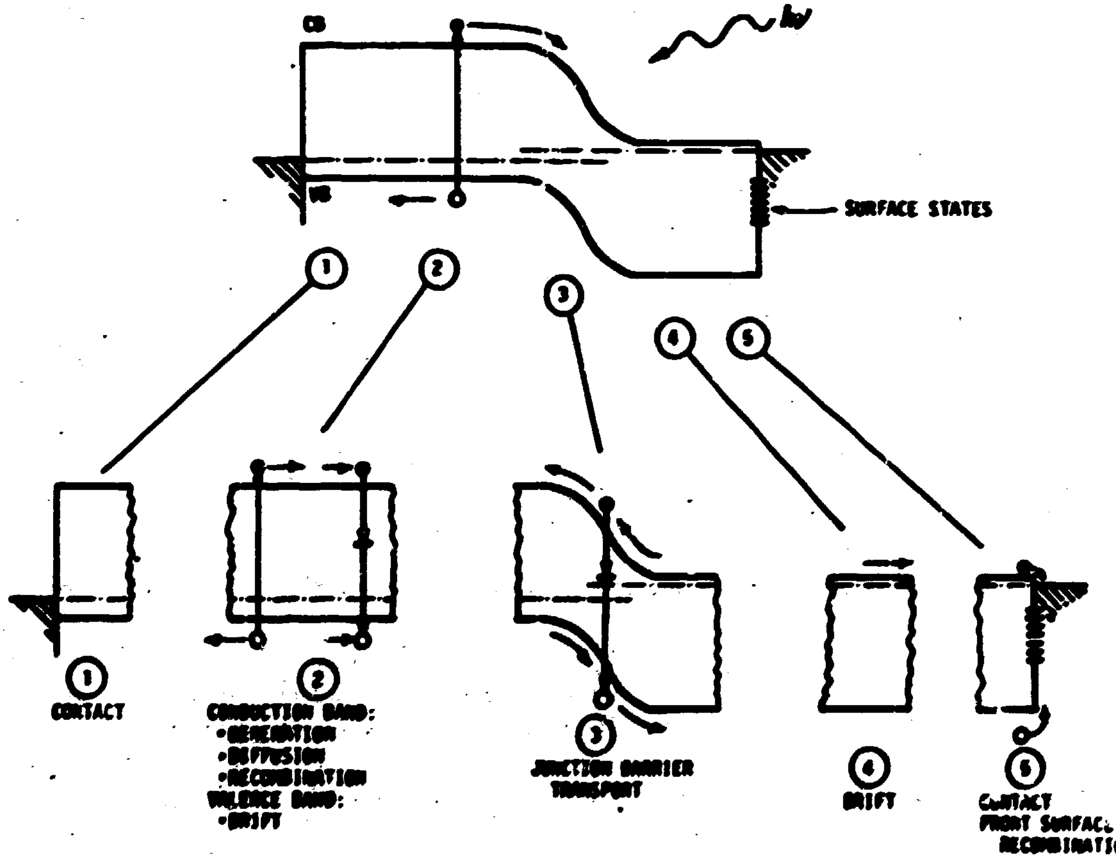

Figure 4: Band model of a pn-junction solar cell with some of the more important processes identified (after Fahrenbruch and Bube[5]).

Different cell types can be distinguished by

- how the built-in field is established (homo- or heterojunctions, or Schottky barriers);
- how the light is absorbed (direct or indirect band gap materials);
- the type of the cell design (front- or back-wall, or multijunction cells);
- the crystal state of the device (single or polycrystalline, or amorphous); and
- whether special surface coating or shaping (antireflection, light trapping) electrode arrangement (to reduce optical absorption or recombination) and connecting materials (tunnel junctions or superlattices) are used.

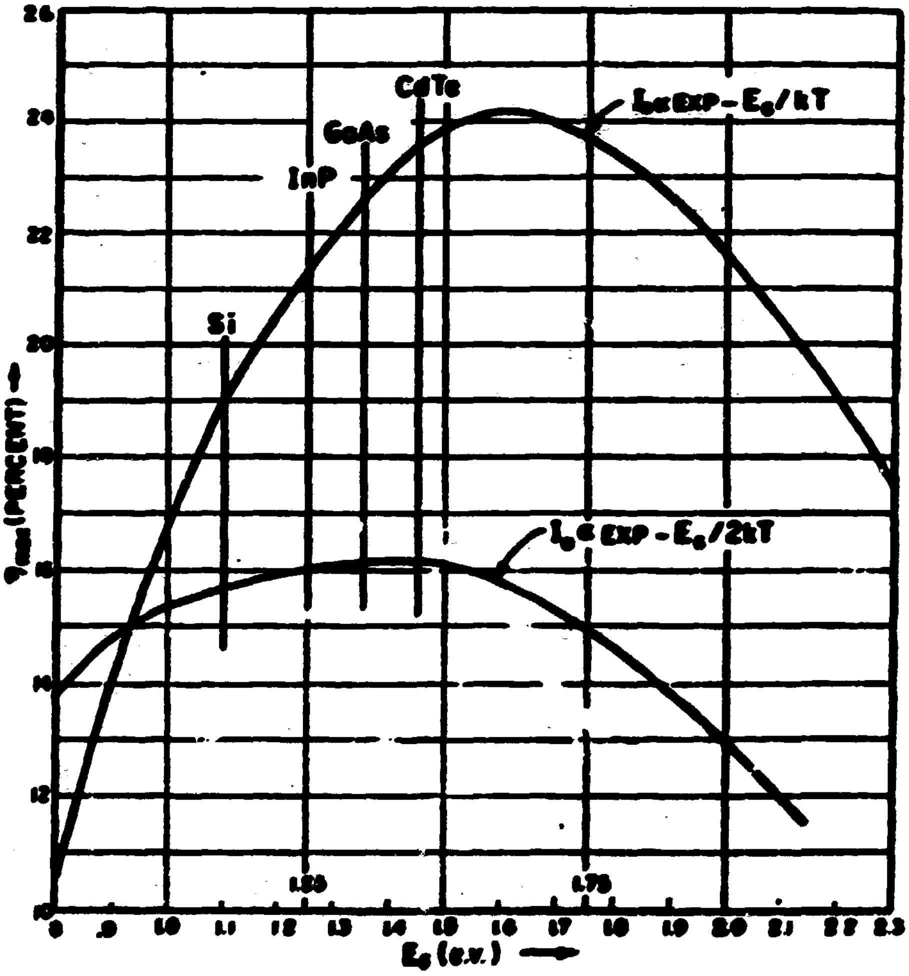

Figure 5: Theoretical maximum solar cell efficiency as function of the band gap after Loferski[9].

Presently there is no clear-cut preference between a large variety of possible devices, except for properly chosen band gap* (see Fig. 5), since there are economic trade-offs and new candidates may be found with promising futures. Examples are the CdS/CuInSe$_2$ cell, which now shows best efficiencies[12] near 12%, and the CdTe cell with efficiencies in excess of 10%, yet both cells were unknown† only a decade ago. However, the large amount of material research necessary before one can hope to optimize material treatment and cell design are in essence economic barriers for rapid expansion. Therefore the first promising candidate, single crystal Si, is still the forerunner in technology development and has still the largest market share.

3 Solar Cell Theory

The theoretical analysis of solar cells proceeds along two substantially different paths, a semiempirical description essentially based on the diode equation, and a basic analysis using the complete set of transport, continuity and Poisson equations for a two carrier model. Both approaches have advantages and disadvantages.

The diode equation approach can easily be applied and permits a relatively simple analytical description of the current voltage characteristic of the different types of solar cells. In some cases one can deduce from its quantitative behavior guidance for cell improvements. However, since the model assumes numerous empirical parameters, as shown below, an adjustment to achieve agreement between theory and experiment provides only marginal insight into the basic cell operation.

The basic analysis, on the other hand, provides such insight and gives guidance to substantial solar cell improvement. However, the approach requires numerical integration, is cumbersome and results in current voltage characteristics only after tedious iterative search for physically meaningful solutions. It is not suited for an immediate interpretation of an experimental result.

A combination of both methods may be used for achieving major advances in the development of substantially improved solar cells.

3.1 Solar Cell Diode Theory.

The current-voltage characteristics of an ideal semiconductor diode is given by the diode equation[14]

$$j = j_o\left(\exp\left(\frac{eV}{kT}\right) - 1\right). \qquad (1)$$

When light is absorbed within the semiconductor diode, at first view this characteristic *seems to be* shifted downwards along the current axis by the generated photocurrent,

---

* It should be noted that the presently *achieved* highest efficiency of Si solar cells is substantially *higher* than the 19% predicted from an obviously too conservative model by Loferski in 1956. Better recent estimates by Wolf[10] put this maximum efficiency for Si to 22% and efficiencies in excess of 28% for AM1 have been suggested more recently[11].

† *A forerunner of this cell, the* CdTe/Cu$_2$Te *cell, however was already noted by* Cusano[13] *in* 1963 *and achieved efficiencies in excess of* 7% *at that time.*

the short-circuit current j_{sc}:

$$j = j_o\left(\exp\left(\frac{eV}{kT}\right) - 1\right) - j_{sc}. \qquad (2)$$

Under certain simplifying conditions there is justification[15] for such a shift which is sometimes referred to as superposition principle, but rarely holds for actual solar cells[16]. Even for better cells there are slight deformations of the jV characteristic from the shifted jV curve (Eq. (2)) which will be discussed below in more detail. Such a typical characteristic is shown in Fig. 6.

The V-axis is crossed at the open circuit voltage V_{oc} and the j axis is crossed at the short circuit current j_{sc}, i.e., at a current that flows when both electrodes are directly connected with each other.

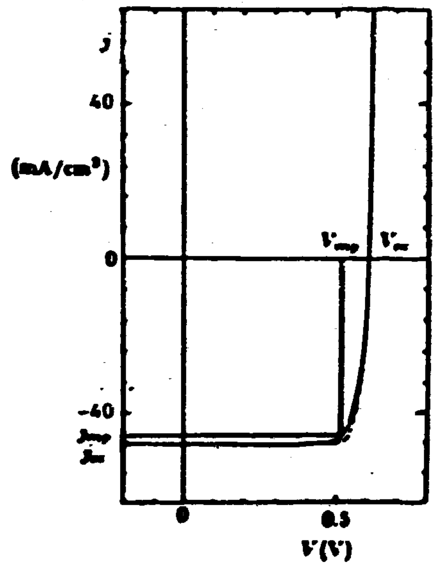

Figure 6: Current-voltage characteristic for a hypothetical homo-junction solar cell. The dashed curve represents the ideal diode characteristic shifted by $j_s = 50\text{mA/cm}^2$.

This device is able to deliver electrical power when operated in the fourth quadrant of the jV-characteristic. When exposed to sunlight, it converts a fraction of its energy into electric energy. The maximum extractable power from such a diode is given by the maximum inscribable rectangle within the fourth quadrant with coordinates of the *maximum power point* V_{mp} and j_{mp} (Fig. 6). The ratio of the $V_{mp}j_{mp}$ product to $V_{oc}j_{sc}$ is called the *fill factor*:

$$FF = \frac{V_{mp}j_{mp}}{V_{oc}j_{sc}}. \qquad (3)$$

Together with V_{oc} and j_{sc}, the fill factor is a measure of the solar cell performance. The ratio of extractable electrical power to the optical input power is called the *solar cell* *efficiency*

$$\eta = \frac{V_{mp} j_{mp}}{P_{opt}}. \tag{4}$$

Sunlight at AM1 (Fig. 7) even at clear weather days is ill-defined and, depending on ozone and water vapor content and on the turbidity changes to some degree[17]. It has an optical power density of approximately:

$$P_{opt}(AM1) \simeq 100 \mathrm{mW/cm^2}. \tag{5}$$

For practical purposes a spectrum as shown for AM1 in Fig. 7 with P=100 mW/cm² is assumed for most computations. However, only a certain fraction of the impinging photonflux can be absorbed, depending on the bandgap of the semiconductor (Fig. 8). The computed electrical power that can be extracted from the hypothetical device at the maximum power point (Fig. 6) is the product of $V_{mp} = 0.525$ V and $j_{mp} = 45.6$ mA/cm², yielding a maximum efficiency for this hypothetical solar cell of

$$\eta \simeq 24\%.$$

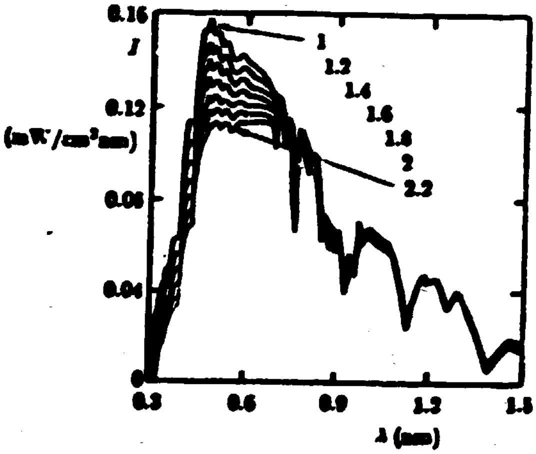

Figure 7: The changing solar spectrum with the airmass as family parameter. The air mass is defined as the relative path length through the earth's atmosphere compared to the sun at the zenith: $AM = 1/\cos(90° - \varphi)$ with φ the solar elevation above the horizon.

Since the dark saturation current j_o is usually negligible compared to j_{sc} and since for $j = 0$ one has $V = V_{oc}$, one can rewrite Eq. (2) by eliminating j_o

$$j = j_{sc}\left\{\exp\left(\frac{e[V - V_{oc}]}{kT}\right) - 1\right\}. \tag{6}$$

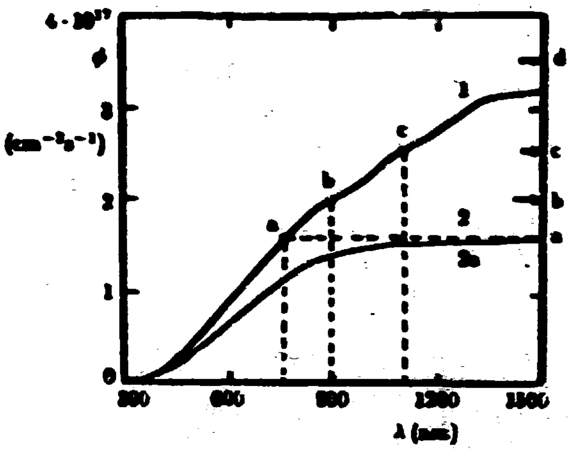

Figure 8: Photon flux for AM1, integrated from $\lambda = 0$ to the given wavelength. The photon flux at wavelengths shorter than the band edge for CdSe, GaAs, and Si are identified as a, b, and c respectively; d is the photon flux in the entire solar spectrum to $\lambda \rightarrow \infty$.

The maximum power point can be obtained from Eq. (6) by setting $d(jV)/dx = 0$, yielding an implicit equation for V_{mp}:

$$V_{mp} = V_{oc} - \frac{kT}{e} \ln\left(1 + \frac{eV_{mp}}{kT}\right), \tag{7}$$

which can be approximated* as

$$V_{mp} \simeq V_{oc} - \frac{kT}{e} \ln\left(\frac{eV_{oc}}{kT} - 2\right). \tag{8}$$

By introducing Eq. (10) into Eq. (6), one obtains:

$$j_{mp} = j_{sc} \frac{\frac{eV_{mp}}{kT}}{1 + \frac{eV_{mp}}{kT}}, \tag{9}$$

which can be approximated as

$$j_{mp} \simeq j_{sc} \frac{\frac{eV_{oc}}{kT}}{1 + \frac{eV_{oc}}{kT}}. \tag{10}$$

---

* A reasonable approximation is obtained by setting $V_{mp} \simeq V_{oc} - 3kT$.

This results in a fill factor of

$$FF \simeq \frac{eV_{oc} - kT\ln\left(\frac{eV_{oc}}{kT} - 2\right)}{eV_{oc} + kT}, \tag{11}$$

which is plotted as a function of V_{oc} in Fig. 9. It is typically about 80% and increases slightly with increasing V_{oc}.

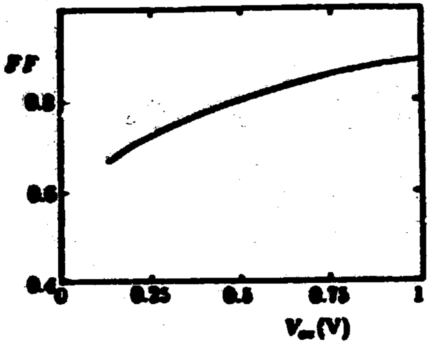

Figure 9: Fill factor for an ideal photo diode as function of V_{oc}.

In most actual devices the fill factor is substantially smaller, usually between 60 and 75% and only high efficiency devices exceeds 80%. There are several reasons for this deviation:

- a network of parasitic resistors (see Fig. 10),
- deep trap level depletion responsible for a fillfactor reduction[18,19],
- the recombination overshoot, discussed in Sec. 3.1.

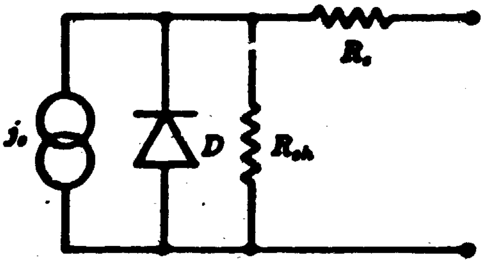

Figure 10: Simple equivalent circuit to explain some deviations from the ideal photo diode behavior.

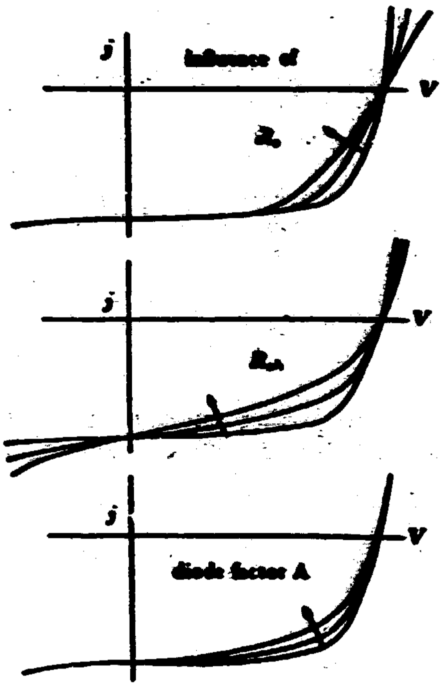

Figure 11: Influence of series resistance, shunt resistance, and diode quality factor on an otherwise ideal photo-diode characteristic.

The *parasitic network of resistors* in an actual device is composed of series resistances, which are due to insufficient conductive paths to the external circuit*, and shunt resistances, which are due to macroscopic defects bridging the diode†. Such a network is usually represented by a single series and shunt resistance (Fig. 10).

Both resistances cause a reduction in the fill factor. The series resistance R_s reduces the slope of the characteristics near V_{oc}, and the shunt resistance R_{sh} increases the slope predominantly near j_{sc}, as shown in Fig. 11.

A *reduction from the ideal shape* near the maximum power point of the characteristic is usually introduced by a diode quality factor $A > 1$. With the introduction of R_s, R_{sh}, and A into the diode equation

$$j = j_o\left\{\exp\left[\frac{e(V - jR_s)}{AkT}\right] - 1\right\} + \frac{V - jR_s}{R_{sh}} - j_o, \tag{12}$$

---

[*] Such as insufficient conductivity of the semiconductor bulk to carry the photocurrent to the top electrode (based on the three-dimensional problem resulting in extremely high current densities near the electrode grid lines), or insufficient thickness of the electrodes.

[†] These defects are more probable in polycrystalline solar cells at grain boundaries or external surfaces bridging the junction.

one has three adjustable parameters in an attempt to fit experimental data. The influence of changes in these three parameters on the jV characteristic is shown in Fig. 11.

It is obvious that such attempts can give grossly misleading indications when the reasons for the deviations from diode ideality is of more basic nature, relating to deep trap depletion or recombination overshoot.

An extensive analysis of the solution curves of the transport, continuity, and Poisson equations is required to unfold the trend in changes of curve shape and related solar cell performance parameters.

3.1 Basic Transport Theory of Solar Cells.

A more thorough analysis dealing with the complete set of transport, continuity and Poisson equations, given below, reveals a more complex behavior of the solution curves. The set of governing equations is*

$$\frac{dn}{dx} = \frac{j_n - e\mu_n nF}{\mu_n kT} \tag{13}$$

$$\frac{dp}{dx} = \frac{-j_p + e\mu_p pF}{\mu_p kT} \tag{14}$$

$$\mu_n = \frac{\mu_{n0}}{\left[1+\left(\frac{\mu_{n0}|F|}{v_n^*}\right)^{\beta}\right]^{1/\beta}} \tag{15}$$

$$\mu_p = \frac{\mu_{p0}}{\left[1+\left(\frac{\mu_{p0}|F|}{v_p^*}\right)^{\beta}\right]^{1/\beta}} \tag{16}$$

$$\frac{dj_n}{dx} = -eU \tag{17}$$

$$\frac{dj_p}{dx} = eU \tag{18}$$

$$U = U_1 = cN_{r1}\frac{np - n_i^2}{n + p + n_i^2} + g_{opt} \quad \text{for} \quad d_1 \leq x < 0 \tag{19}$$

$$U = U_2 = cN_{r2}\frac{np - n_i^2}{n + p + n_i^2} + g_{opt} \quad \text{for} \quad 0 \leq x \leq d_2 \tag{20}$$

$$\frac{dF}{dx} = \frac{e(p - N_a)}{\varepsilon\varepsilon_0} \qquad \text{for} \quad d_1 \leq x < 0 \tag{21}$$

---

* The model is simplified in many respects (same capture cross section for the two carriers when recombining, only one donor and acceptor level, no spacial distribution of N_a, N_d, N_r and g_{opt}). The model can easily be expanded for the actual computation. Here only the general behavior is of interest, hence the simplification.

$$\frac{dF}{dx} = \frac{e(N_d + p - n)}{\epsilon\epsilon_0} \qquad \text{for} \quad 0 \leq x \leq d_2 \tag{22}$$

$$\frac{d\psi}{dx} = -F \tag{23}$$

$$n_i^* = 2n_i \cosh \frac{E_i - E_r}{kT} \tag{24}$$

with the relavant parameter values for Si listed in Table 2.

Table 2: Parameters Used for the Silicon Diode.

Parameters	N_a	N_d	N_{r1}	N_{r2}	N_c	N_v
Values	10^{18}	10^{16}	10^{17}	10^{15}	$2.04 \cdot 10^{18}$	$6.54 \cdot 10^{18}$
Dimensions	cm^{-3}	cm^{-3}	cm^{-3}	cm^{-3}	cm^{-3}	cm^{-3}
Parameters	n_{10}	p_{10}	n_{20}	p_{20}	μ_{n0}	μ_{p0}
Values	2.2	10^{18}	10^{16}	220	1450	490
Dimensions	cm^{-3}	cm^{-3}	cm^{-3}	cm^{-3}	cm^2/Vs	cm^2/Vs
Parameters	E_g	$E_i - E_r$	$c_{rn} = c_{nr} = c$	$v_n^* = v_p^*$	ϵ	T
Values	1.12	0.15	10^{-9}	$5.4 \cdot 10^6$	11.8	300
Dimensions	eV	eV	cm^{3}s^{-1}	cm/s	–	°K
Parameters	d_1	d_2	$L_n(p)$	$L_p(n)$	L_{Dp}	L_{Dn}
Values	$5 \cdot 10^{-6}$	10^{-2}	$6.13 \cdot 10^{-4}$	$3.6 \cdot 10^{-3}$	$4.14 \cdot 10^{-7}$	$4.14 \cdot 10^{-6}$
Dimensions	cm	cm	cm	cm	cm	cm
Parameters	v_{Dn}	v_{Dp}	V_D	n_i^2	τ_n	τ_p
Values	$6.13 \cdot 10^4$	$3.56 \cdot 10^3$	0.467	$2.2 \cdot 10^{18}$	10^{-8}	10^{-5}
Dimensions	cm/s	cm/s	V	cm^{-6}	s	s
Parameters	$m_{n,de}$	$m_{p,de}$	$m_{n\mu}$	$m_{p\mu}$	n_1^*	n_i
Values	0.188	0.409	0.26	0.24	$4.84 \cdot 10^{11}$	$1.48 \cdot 10^9$
Dimensions	m_e	m_e	m_e	m_e	cm^{-3}	cm^{-3}

The typical set of solution curves for a rather thin device (in order to emphasize the junction properties) is given in Fig. 12.

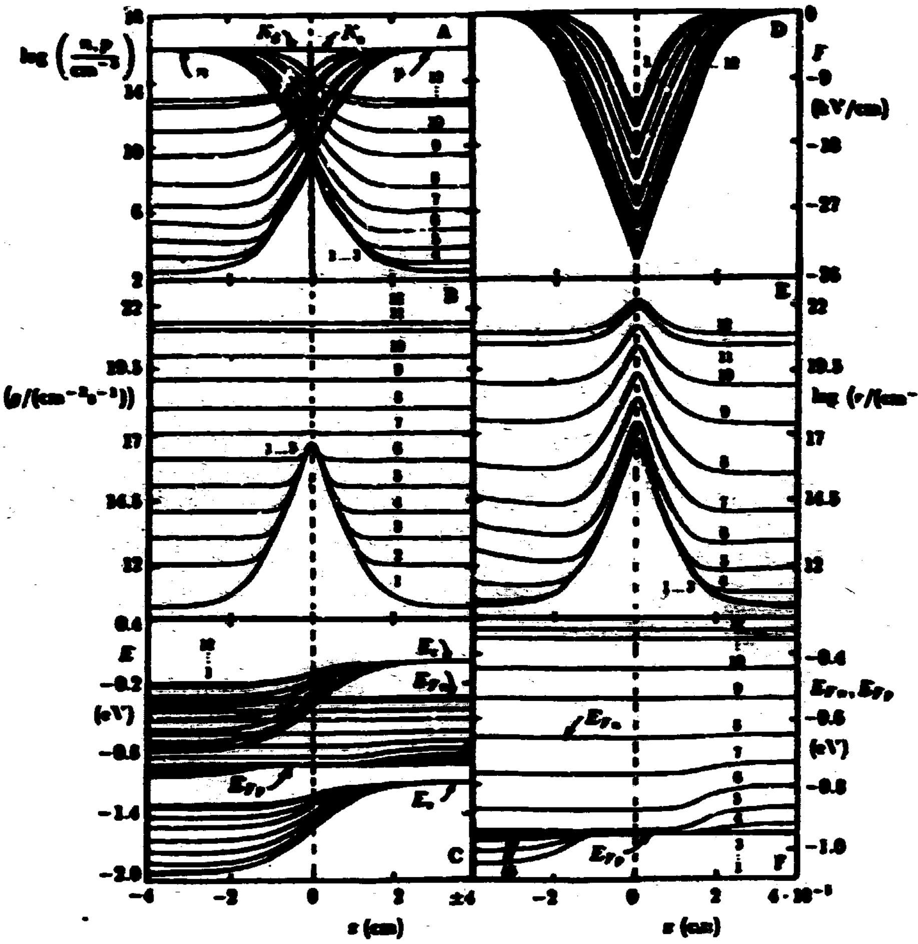

Figure 12: Solution curves for a symmetrical thin Si pn-junction device with g_{opt} as family parameter; $g_{opt} = 0, 10^{12}, 10^{13}, 10^{14}, 10^{15}, 10^{16}, 10^{17}, 10^{18}, 10^{19}, 10^{20}, 10^{21}$, and $2\cdot10^{21}$ cm^{-3}s^{-1} for curves 1–12 respectively. Shown are the distributions of the carrier densities (A), the generation rates (B), the band picture (C), the field (D), the recombination rates (E), and the quasi-Fermi levels (F) (enlarged scale from C).

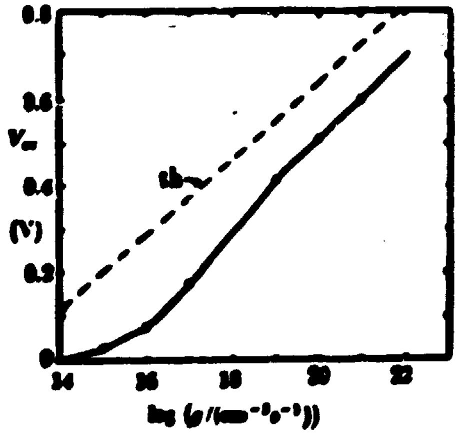

Figure 13: Open circuit voltage as a function of the optical generation rate; obtained from the computation shown in Fig. 12. The theoretical curve is obtained by using Eq. (28). computation for higher g_{opt}.

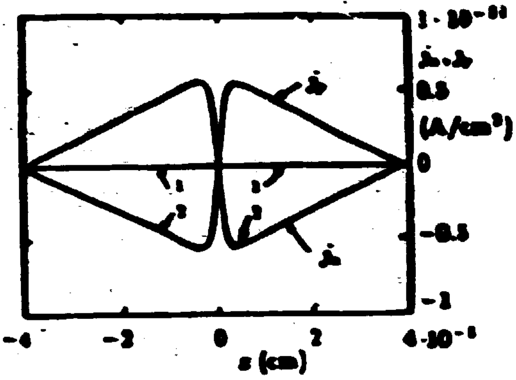

Figure 14: Typical electron and hole current distributions in a thin symmetrical Si pn-junction device with negligible surface recombination; computed as given in the text. $g_{opt} = 0$ and $1 \cdot 10^{12}$ cm^{-3}s^{-1} for curves 1 and 2 respectively. For higher optical generation rates the shape of the current distribution remains the same, the amplitude increases linearly with g_{opt}.

From this figure one can deduce the relationship between V_{oc} and the average generation rate. This is shown in Fig. 13: the open circuit voltage is substantially below the theoretical value given in Eq. (28). This is caused by the *recombination overshoot** near the center of the junction (compare subfigures B and E of Fig. 12). This recombination overshoot requires a large generation/recombination loss current to flow from the bulk regions to the junction (see Fig. 14). The height of the recombination overshoot depends on the device parameters, and its influence on V_{oc} varies accordingly as shown for variation in the density of recombination centers, doping density and optical generation rates in Fig. 15 for various device thickness or surface recombination velocities, indicated by the current at $x = \pm 4 \cdot 10^{-5}$ cm as family parameter. With appropriate changes in device parameters one can minimize such losses.

In addition, there are losses at the junction interface because of an increased density of recombination centers (donor/acceptor pairs) due to unavoidable cross-doping, and at the surfaces due to surface recombination (with the maximum recombination velocity $s \simeq v_{rms}$ expected at every metal surface).

This example reveals the importance of the recombination overshoot as a *intrinsic loss mechanism*. This causes a *reduction* of the open circuit voltage and fill-factor below the theoretical limit which was obtained from the shifted diode equations when setting $j = 0$, yielding

$$V_{oc} = \frac{kT}{e} \ln\left(\frac{j_{sc}}{j_o}\right). \qquad (25)$$

---

* *For any given optical generation the recombination rate is larger than the generation rate near the junction interface (in thermal equilibrium they are the same).*

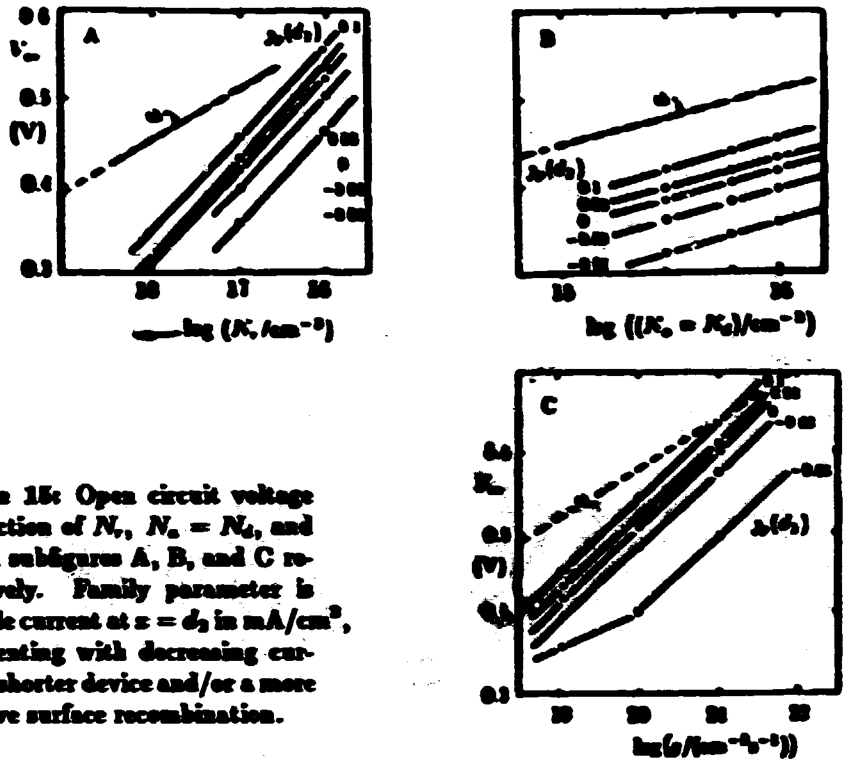

Figure 15: Open circuit voltage as function of N_r, $N_a = N_d$, and g_{opt} in subfigures A, B, and C respectively. Family parameter is the hole current at $x = d_2$ in mA/cm², representing with decreasing current a shorter device and/or a more effective surface recombination.

When (for simplicity) assuming* that most of the minority carriers are collected from the p-type region, one obtains[30] (see also Eq. (31)):

$$j_{sc} \simeq j_{sc,n} = e n_{opt} v_{Dn} \tanh\left(\frac{x_m}{L_n}\right) = e g_{opt} \tau_n v_{Dn} \tanh\left(\frac{x_m}{L_n}\right) \tag{26}$$

and

$$j_0 \simeq j_{0,n} = e n_{th} v_{Dn} \tanh\frac{x_m}{L_n} = e\frac{n_i^2}{N_a} v_{Dn} \tanh\left(\frac{x_m}{L_n}\right) \tag{27}$$

where n_{opt} and n_{th} are the optically or thermally generated minority carrier densities and x_m is the position of the maximum of $n(x)$ as shown in Fig. 19A and B. v_{Dn} is the diffusion velocity L_n/τ_n. When inserting these results into Eq. (25) one obtains

$$V_{oc} \simeq \frac{1}{e}\left(E_g - kT\ln\left(\frac{N_c N_v}{N_a g_{opt} \tau_n}\right)\right). \tag{28}$$

This is the *same result* one obtains from the spread of the quasi-Fermi levels in the region of the predominant minority carrier generation (assumed here to be the p-type region):

$$V_{oc} \simeq \frac{1}{e}\left(E_g - \left[E_c - E_{Fn}\right] - \left[E_{Fp} - E_v\right]\right)_p. \tag{29}$$

---

* The same results can be obtained in a more rigorous analysis accounting for both, the p and n-type side of the device.

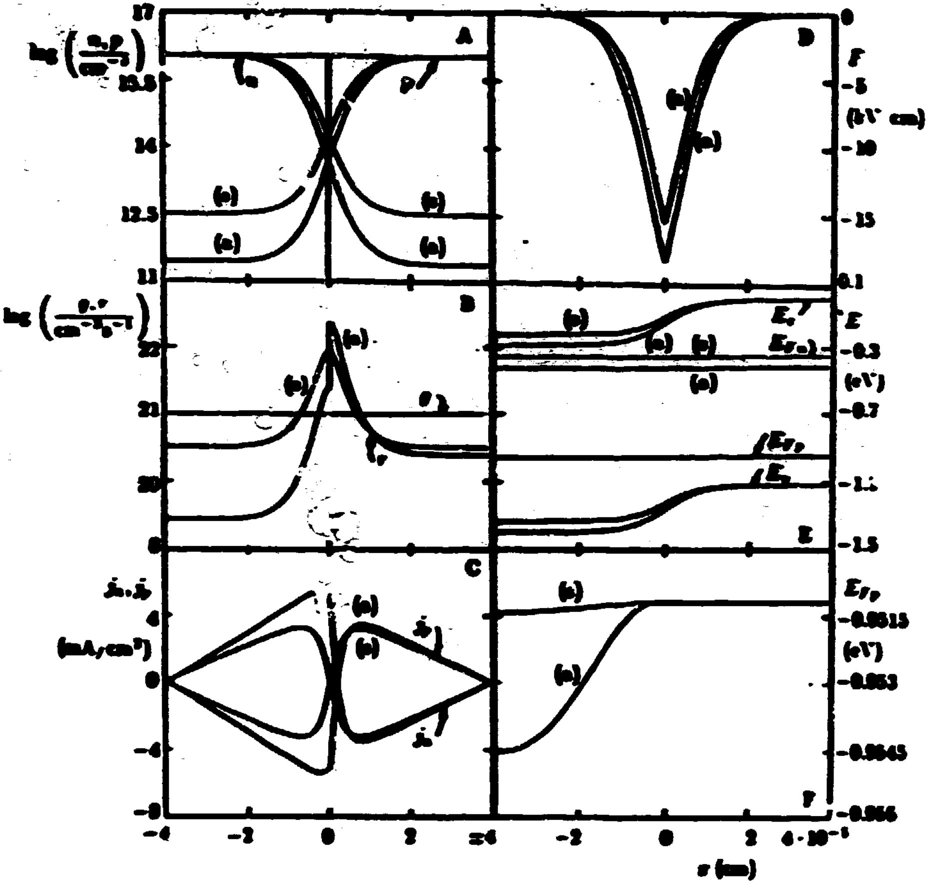

Figure 16: Solution curves of Eqs. (13) - (24) for a symmetrically doped, thin Si solar cell, and for $g_{opt} = 10^{21}$ cm^{-3}s^{-1}; curves (s) for $N_r = 10^{17}$ cm^{-3} in the entire device and curves (a) for the same density of recombination centers in the n-type region and for $N_r = 10^{18}$ cm^{-3} in the p-type region.

Another revealing example is shown in Fig. 16 where the *density of the recombination centers* is increased by a factor of 10 in the p-type region of the device only, resulting in a carrier lifetime reduced by the same factor. However, rather than reducing the minority carrier density only in the p-type region by this factor of 10, *both* minority carrier densities are reduced by a somewhat lower factor of 8.8. For comparison the solution curves for the symmetric case (same density of recombination centers of 10^{17} cm^{-3} on both sides) are also plotted in Fig. 16.

A similar decrease of the minority carrier density, here by a factor of 2.3 (rather than 5) on *both* sides of the junction results when the *optical generation rate* is reduced in only one side as shown in Fig. 17.

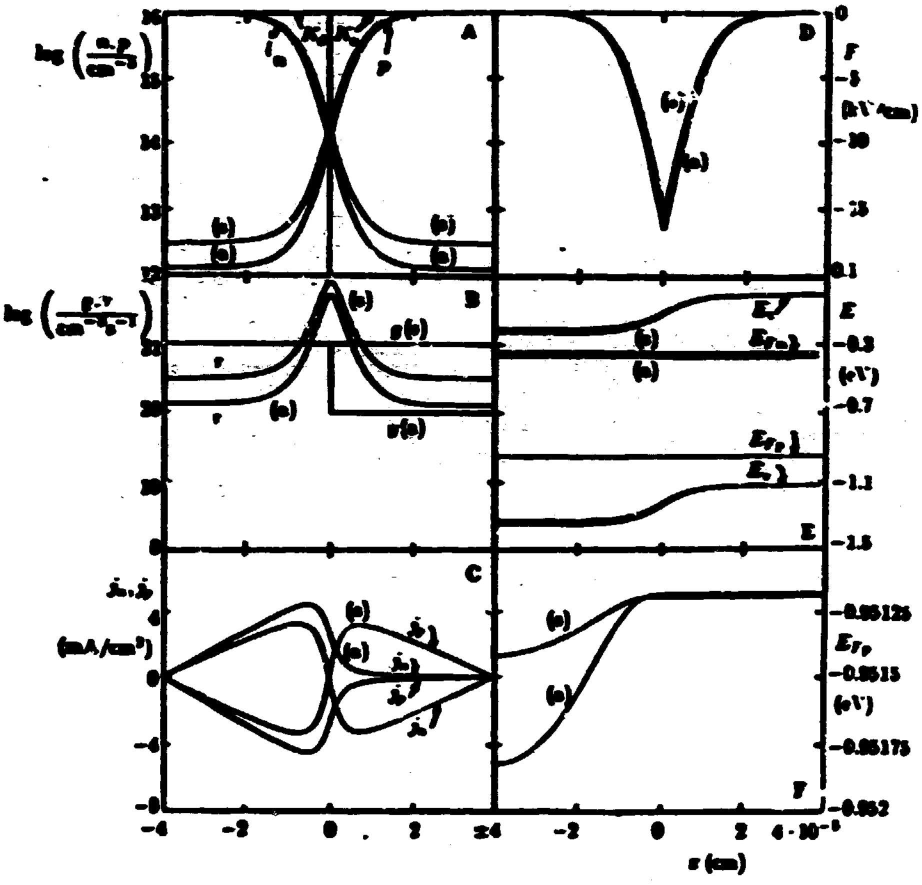

Figure 17: Solution curves as in Fig. 16 (curves (s) are repeated), however curves (a) are obtained or a reduced generation rate from 10^{21} to 10^{20} cm^{-3}s^{-1} in the p-type region.

These examples indicate that *both sides of the junction communicate well with each other* in respect to the minority carrier density, and that non-linear recombination is significant. The reason for the perfect communication is the *continuity of each current* (j_n and j_p). This communication *persists* for a characteristic length, the *diffusion length*. In Figs. 16 and 17 the device width is much smaller than the diffusion length of both minority carriers, hence we observe *perfect* communication.

The resulting current voltage characteristic obtained from the computed solution curves shown in Fig. 18 are substantially different than calculated for the ideal case: the open circuit voltage and the fill-factor are reduced, the saturation current is not*. The

---

* j_{sc} is given in this thin device with neutral surfaces by $eg_{opt}(d_1 + d_2)$ for curves 1 and 2 and by $e(g_{opt,1}d_1 + gopt,2d_2)$ for curve 3 in Fig. 18.

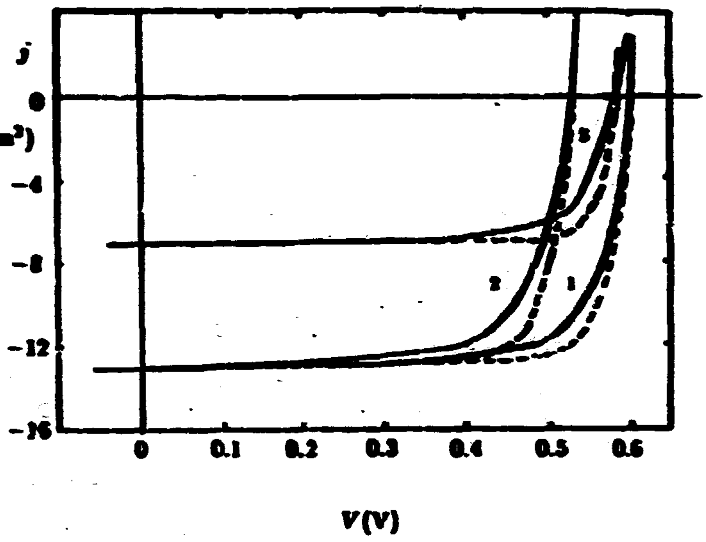

Figure 18: Current-voltage characteristics for the symmetric Si solar cell (curves 1), for the cell with a jump in recombination center densities (curve 2) and with a jump in generation rates (curve 3) as given in Figs. 16 and 17. The dashed curves are the ideal diode characteristics computed for the same values of j_{sc} and V_{oc}.

reduction in the fill-factor can be expressed in a change of the diode quality factor from 1 to a value substantially larger* than 1. In light of this discussion the diode quality factor appears with different significance. The deviations from the ideal diode characteristics occur as a result of the recombination overshoot in the junction. This effect is amplified hereby choosing a very thin device.

The results given as examples here have significant impact in the design of improved devices. For instance, the effect of the recombination overshoot can be minimized by an appropriate choice of the device parameters. The effect of communication of minority carriers through a junction, however, indicates the need for rethinking of the design of both electrodes: since every electrode acts like a perfect recombination surface and a junction does not appear to provide a perfect separation from the active region, such separation has to be provided by a thicker layer of the semiconductor or by a two-dimensional grid or dot-structure of both electrode contacts, thereby reducing the effective recombination surface area. We will return later to this description in more detail.

Since a comprehensive analysis of the transport properties (except for a few examples) is still missing, we will now resort to a more general, semiempirical description in the next section, to categorize the different loss mechanisms.

---

* The quality factor is A=1.52, 1.88 and 2.4 for curves 1–3 respectively (see figure caption).

- optical losses (reflection, incomplete absorption and shading effects),
- intrinsic losses (recombination-related),
- surface related losses, and
- geometry-related losses (usually described by a network of parasitic resistors).

Optical reflection losses are minimized by surface etching providing a pyramidical surface which gives a velvet effect and by antireflection coating, which together can reduce reflection to below 5% in the photoelectric active part of the solar spectrum of better solar cells. Incomplete absorption (for indirect bandgap material) can be minimized by making the cell thick enough, making the back-contact reflecting and by light-trapping (i.e., by shaping the surfaces so that most of the light impinges below the Brewster angle). In better cells typically >90% of the photoelectric active photon spectrum ($h\nu > E_g$) is absorbed within the electrically active part of the cell.

3.2.2 Minority Carrier Collection via Diffusion. Intrinsic losses can more easily be understood when separate in relation to the short circuit current and to the open circuit voltage. Short circuit current losses are characterized by the collection efficiency, which gives the fraction of the generated minority carriers which are collected at the respective electrodes. This collection competes with the recombination within the cell and at the surfaces. The characteristic cell parameter describing the collection efficiency is the minority carrier lifetime τ_n or τ_p in the p- and n-type region respectively, and derived from it the diffusion length

$$L_n = \sqrt{\frac{\mu_n kT}{e}\tau_n} \quad \text{or} \quad L_p = \sqrt{\frac{\mu_p kT}{e}\tau_p}. \tag{30}$$

Without field assistance the collection efficiency can be obtained from solving diffusion and continuity equation* resulting in[30]

$$\eta_{c,n} = \frac{L_n}{d_p}\tanh\frac{x_{m,n}}{L_n} \quad \text{and} \quad \eta_{c,p} = \frac{L_p}{d_n}\tanh\frac{x_{m,p}}{L_p} \tag{31}$$

with $x_{m,n}$ or $x_{m,p}$ the position of the maximum of the minority carrier density in the n and p-type region respectively which occurs when outdiffusion of these carriers to the surface (loss) competes with the diffusion into the junction (collection); d_p and d_n are the thicknesses of the p and n-type regions respectively. When the surface recombination

---

* The reason that fields (Poisson equation) can be neglected in the current generating regions of most solar cells relates to the fact that in these devices the diffusion length (or cell width) are long compared to the Debye length (or junction width). Hence, in most of the active material the space charge has vanished and the drift current is negligible for minority carriers. This permits solving current and continuity equation for minority carriers *explicitely* as shown in most textbooks. We have chosen a simple representation, using x_m, which is much more transparent for further explanation and which can easily be bracketed by $0 < x_m < d_m$ (or d_p) and is often approximated by $x_m \simeq d_n/2 \simeq d_p/2$.

current is negligible, then $x_{m,n} \simeq d_n$ and $x_{m,p} \simeq d_p$. The dependence of η_c on surface and volume recombinations is shown in Fig. 19.

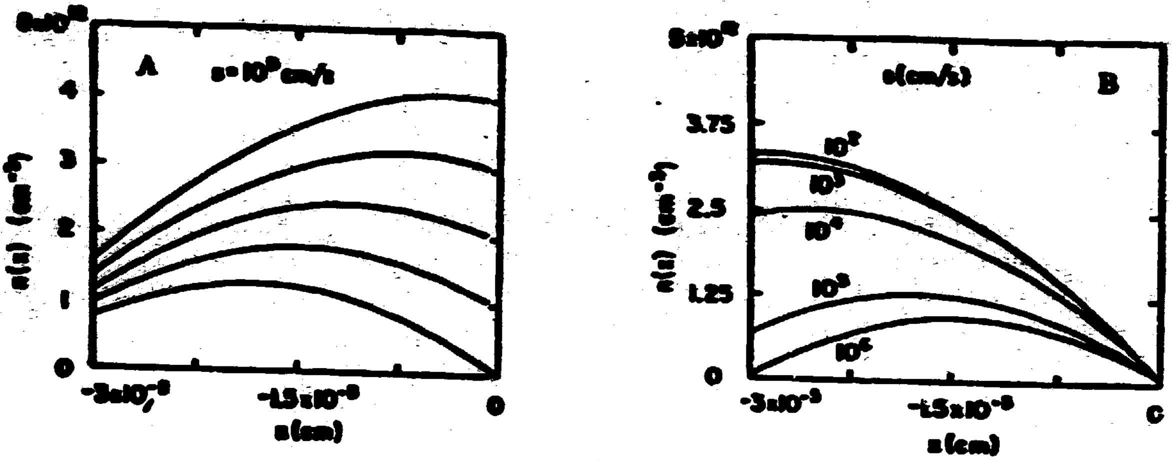

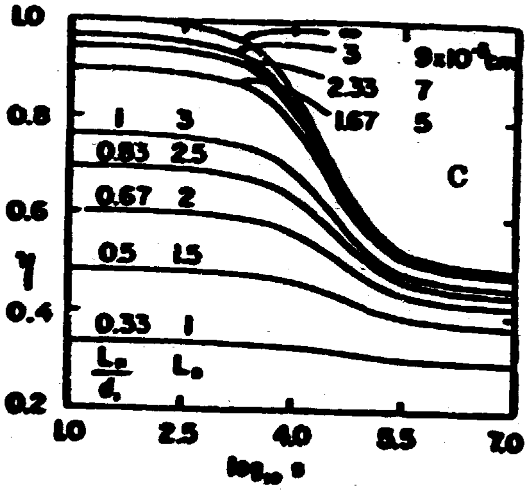

Figure 19: Minority carrier distribution A) with a surface recombination velocity $s = 10^5$ cm/s at the left outer surface and for different reverse currents at $x = 0$ as family parameter, B) for saturation current at $x = 0$ and with the surface recombination velocity as family parameter, and C) collection efficiency as function of the surface recombination velocity with the diffusion length as family parameter (device thickness $3 \cdot 10^{-5}$ cm).

3.2.3 Driftfield-Enhanced Carrier Collection. An increase of the collection efficiency by introducing a drift field in the base (neglecting a field near the back electrode to reduce back surface recombination) is of advantage for solar cells with a low $\mu\tau$ product as one can see from the relation between Schubweg L_e and diffusion length. For the required $L_e > L_n > 2d_p$ one needs homogeneous fields in the region of predominant minority carrier generation of

$$F_{drift} > d_p/(\mu_n \tau_n). \tag{32}$$

This condition is fulfilled for the i-region of α-Si solar cells and probably for the compensated part of the CuInSe$_2$ layer in CdS/CuInSe$_2$ solar cells with a shifted junction.

A theoretical analysis of the set of solution curves of the set of Eqs. (13) – (24) for α-Si is most instructive and is given below for two cases of an α-Si solar cell with a slightly and a heavily compensated i-layer.

3.2.4 Amorphous Silicon as Example for i-layer Collection. The i-layer can be considered as an interfacing layer of substantially reduced doping density between a higher doped n and p region. We are assuming here that this i-layer is n-type with a highly simplified device configuration* Fig. 20.

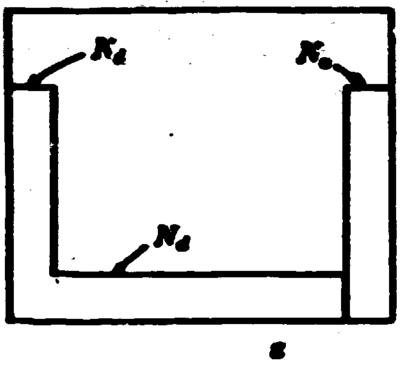

Figure 20: Schematics of a doping profile in an nip-junction as assumed for the following discussion.

The principal set of parameters is given in Table 3 for α-Si. In the following analysis we will use this principal set while varying one specific parameter in order to demonstrate its influence on the solution curves.

For boundary conditions we assume neutral outer surfaces. They are the easiest to use for the actual computation and are reasonably justified when the main carrier collection is considered from the internal i-type region, which is separated by two barriers from the two electrodes. Such neutral surfaces are characterized by $j_e = 0$ and permit $j_n(d_1) = j_p(d_1) = j_n(d_2) = j_p(d_2) = 0$ in open circuit conditions. Field and majority carrier density at the surface are chosen so that they approach asymptotically the singular points at both surfaces (i.e., $\frac{dn}{dx} = \frac{dF}{dx} \equiv 0$ in the n-type region, and $\frac{dp}{dx} = \frac{dF}{dx} \equiv 0$ in the p-type region). The yet unknown minority carrier density at the start of the computation

---

* Again chosen here to amplify the involved principles.

Table 8: Parameters Used for the a-Si Solar Cell

Parameters	N_d	N_{di}	N_a	N_{r1}	N_{ri}	N_{r2}
Values	10^{17}	10^{15}	10^{17}	10^{17}	10^{17}	10^{17}
Dimensions	cm^{-3}	cm^{-3}	cm^{-3}	cm^{-3}	cm^{-3}	cm^{-3}
Parameters	p_{10}	n_{10}	p_{i0}	n_{i0}	p_{20}	n_{20}
Values	$6 \cdot 10^{-8}$	10^{17}	$6 \cdot 10^{-6}$	10^{15}	$6 \cdot 10^{-8}$	10^{17}
Dimensions	cm^{-3}	cm^{-3}	cm^{-3}.	cm^{-3}	cm^{-3}	cm^{-3}
Parameters	N_c	N_v	T	n_i^2	n_i	n_i^*
Values	$2.5 \cdot 10^{19}$	$1.8 \cdot 10^{19}$	300	$6.2 \cdot 10^{9}$	$7.9 \cdot 10^{4}$	$1.6 \cdot 10^{5}$
Dimensions	cm^{-3}	cm^{-3}	°K	cm^{-6}	cm^{-3}	cm^{-3}
Parameters	E_g	$E_i - E_v$	$c_{cr} = c_{rv} = c$	$\tau_n = \tau_p$	g_{opt}	$g_{opt}\tau_0$
Values	1.7	0	10^{-9}	10^{-8}	$2 \cdot 10^{21}$	$2 \cdot 10^{13}$
Dimensions	eV	eV	cm^3s^{-1}	s	$cm^{-3}s^{-1}$	cm^{-3}
Parameters	d_1	d_i	d_2	ϵ	v_n^*	v_p^*
Values	500	$5.5 \cdot 10^{-5}$	500	11.7	$2.7 \cdot 10^{6}$	$3 \cdot 10^{6}$
Dimensions	cm	cm	cm	—	cm/s	cm/s
Parameters	μ_{n0}	μ_{p0}	$m_{n,ds}$	$m_{p,ds}$	$m_{n\mu}$	$m_{p\mu}$
Values	1	0.1	1	0.8	1	0.8
Dimensions	cm^2/Vs	cm^2/Vs	m_0	m_0	m_0	m_0
Parameters	$L_n(p)$	$L_n(i)$	$L_p(n)$	L_{Dp}	L_{Di}	L_{Dn}
Values	1,600	1,600	510	130	1,300	130
Dimensions	Å	Å	Å	Å	Å	Å

is iteratively adjusted* so that the current densities fulfill the appropriate condition at both outer surfaces.

For solution curves of Eqs. (13) — (24), we will discuss the sets of $n(x)$, $p(x)$, and F(x), the potentials $E_c(x)$, $E_v(x)$, $E_{Fn}(x)$ and $E_{Fp}(x)$, the currents $j_n(x)$ and $j_p(x)$, and the generation and recombination rate distributions $g(x)$ and $r(x)$. Specific variation of these distributions are instructive for understanding the specific operating modes of this solar cell.

In Fig. 21 a family of solution curves is plotted with the donor density in the bulk (i-layer) as family parameter. At higher doping densities the bulk region is thick enough to provide a substantial region at which $n \simeq N_d$, and consequently $\varrho = 0$; here $F(x)$ has

---

* The iteration actually involves all three free variables, $n(d_2)$, $p(d_2)$, and $F(d_2)$, with ψ artificially fixed at $\psi(d_2) = 0$ (when starting the computation at d_2 and proceeding into direction of lower x values).

decreased to very low values: both junction regions are separated from each other by a substantial center region within the i-region of vanishing field (Fig. 21, curve set 1).

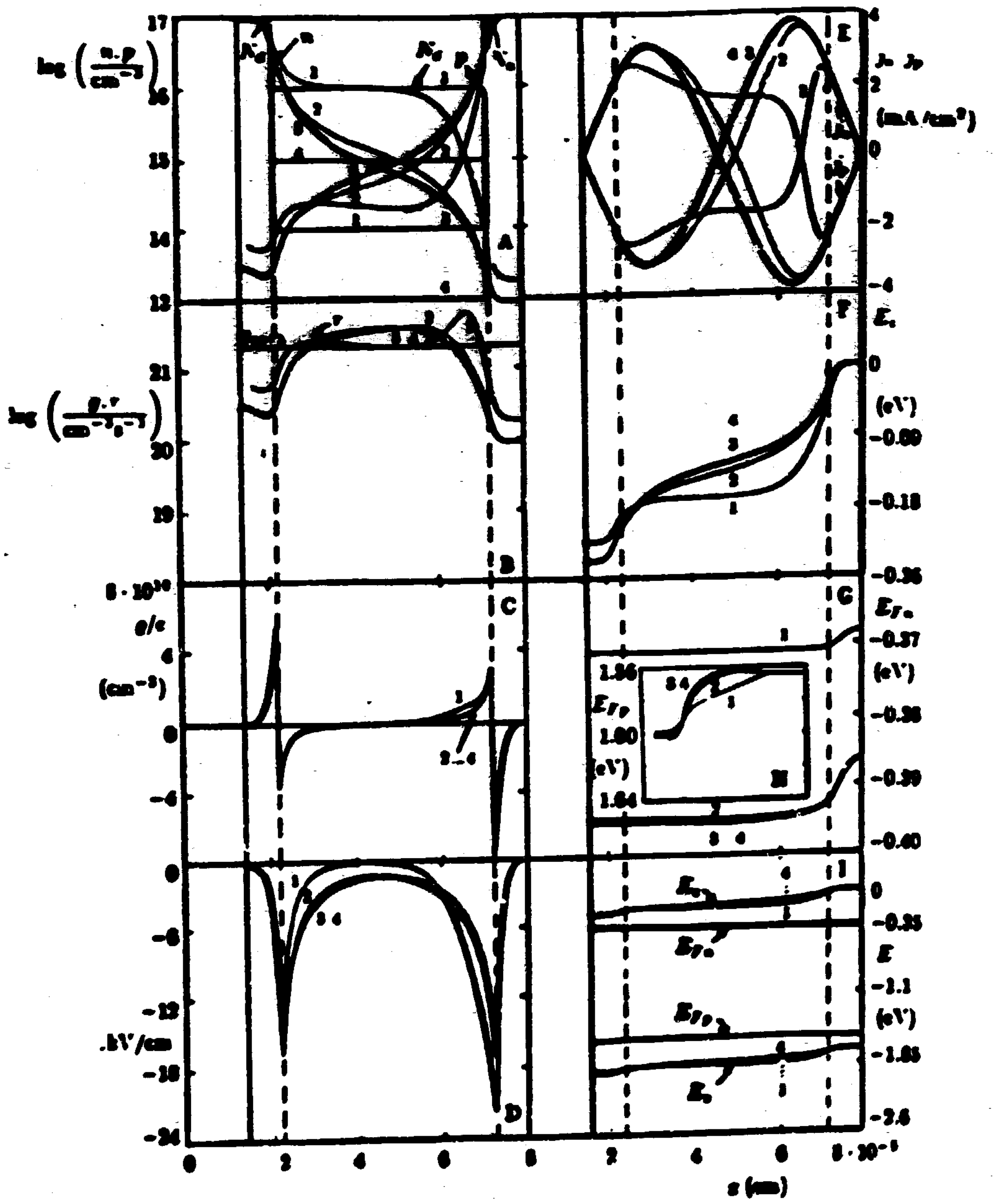

Figure 21: Solution curves computed for open circuit conditions for an a-Si cell (0.65 μm thick), with $g_{opt} = 2\cdot10^{21}$ cm^{-3}s^{-1} and parameters listed in Table 3. Family parameter is the donor density in the center region: $N_d = 10^{16}$, 10^{15}, 10^{14}, and 10^{13} for curves 1–4 respectively.

The cross-over of n and p is close to the np-junction, and causes a major recombination overshoot there.

With reduced donor density (curves 2–4) the space charge does not vanish in an extended region. It is given in the n-type bulk by $n(x)$ or $p(x)$, essentially (except for the very center of curve set 2) independent of the doping. This causes many solution curves ($n(x)$, $p(x)$, $r(x)$, $F(x)$, $j_n(x)$, and $j_p(x)$) to become nearly symmetrical*.

The field in the bulk is no longer reduced to zero but shows a wide minimum (here at about 2 kV/cm) independent of bulk doping for $N_d < 10^{15}\text{cm}^{-3}$. This minimum field depends on the doping of the adjacent n^+ and p^+ regions and on the width of the i-region.

The broad (even though smaller) recombination overshoot (subfigure B) for a higher compensated bulk causes a larger accumulation of recombination currents (subfigure E), and thus a larger reduction in the spread of quasi-Fermi levels, hence a slight penalty in V_{oc} for higher compensation.

Fig. 22 shows a set of solution curves for the highly compensated case. There is little difference in the qualitative behavior from the set at much smaller degree of compensation, except that at low reverse current the field increases rapidly into a range where satisfactory drift field assistance can be rendered. When estimating the Schubweg for holes one recognizes that at an average field of 5 kV/cm this Schubweg is only 10% of the thickness of the i-layer with only minute collection efficiency, while for electrons it has reached the thickness of the i-layer, causing already a collection efficiency in excess of 80%. Hence a somewhat unusual situation occurs in so far as a major contribution to the photo current stems from electrons created in a (slightly) n-type region (the i-region).

The maximum field at the junction changes little while most of the voltage drop occurs in the i-layer with a corresponding large change in the bulk field. As a result of the carrier distribution a slight asymmetry occurs with more of the voltage drop occuring in the i-layer near the np-junction, while a somewhat smaller drop occurs near the nn-junction (subfigure H).

The resulting jV-characteristics (Fig. 23) show a less pronounced sloping branch in the highly compensated case where, at relatively small reverse currents, the drift field is already large enough to create a Schubweg in excess of the i-layer width for the carrier with higher mobility (here for the electrons). Again, if such pronounced sloping branch occurs, it may be caused by lesser compensation (curve 2) or by a lower carrier $\mu\tau$ product, reducing the Schubweb below the i-layer width.

The solution curves for the lowly compensated case are shown in Fig. 24. A substantial difference to the highly compensated case is best seen by comparison of the field distributions (subfigure E). In the lowly compensated case the field rapidly decreases from the np-junction into the i-layer and only near zero bias or in reverse bias becomes high enough near the nn-junction to cause substantial drift-field assistance. Consequently, the jV-characteristic (curve 2 in Fig. 23) shows a major sloping branch.

---

* A small asymmetry remains because of the differences in μ_n and μ_p, and in m_n and m_p.

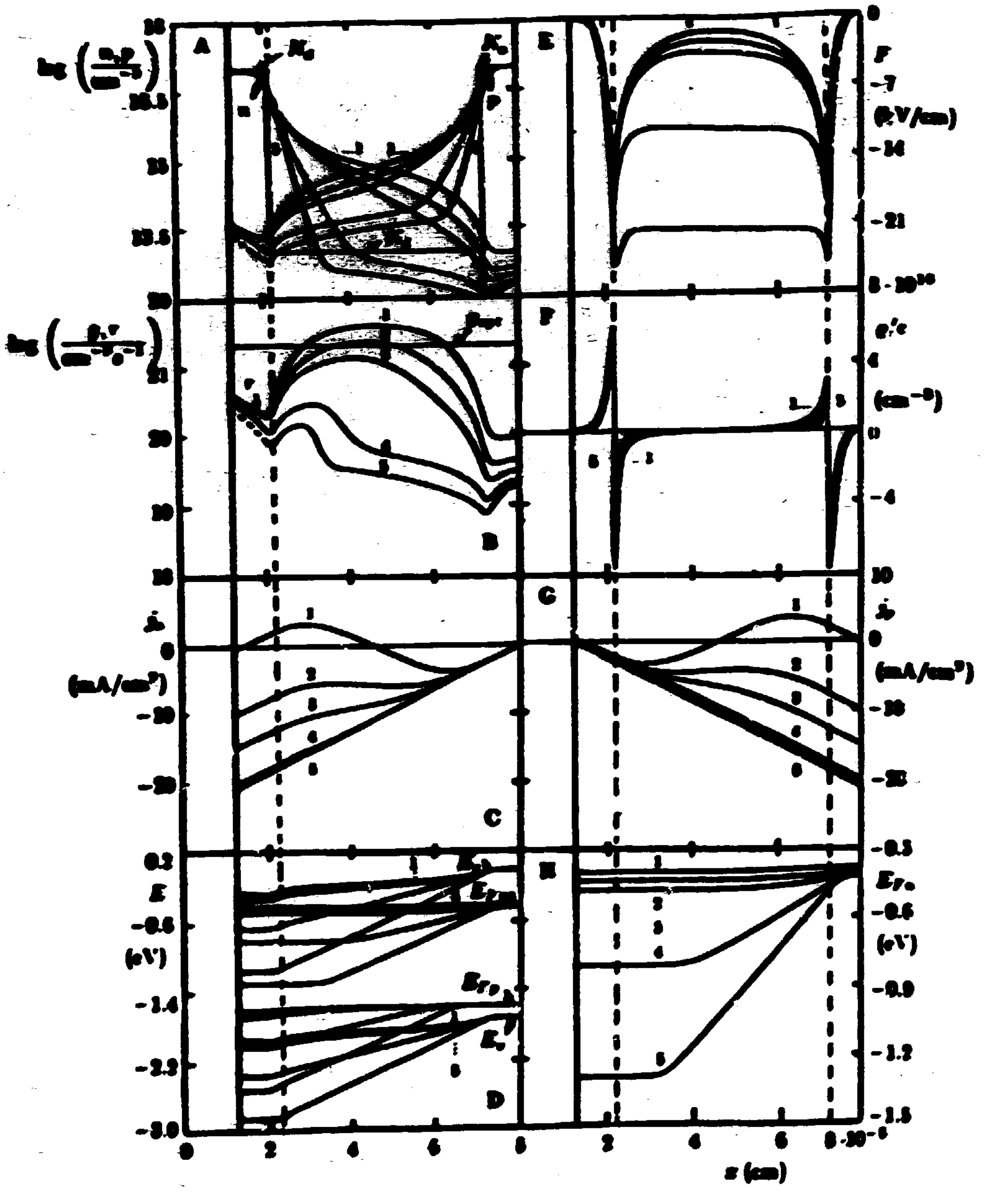

Figure 22: Solution curves for the a-Si solar cell as in Fig. 21 for the highest degree of compensation (curve 4) and with total current as family parameter; $j = 0, -10, -15, -20$ and -21mA/cm^2 for curves 1–5 respectively.

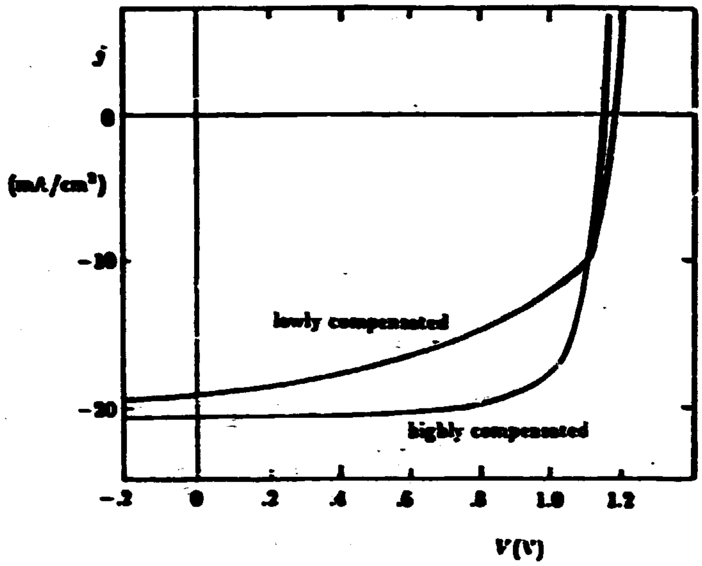

Figure 23: Current-voltage chracteristics obtained from the solution curves for high compensation shown in Fig. 22 and for a similar set corresponding to low compensation (Fig. 24) for curves 1 and 2 respectively.

In addition, the decrease of n below N_d in the i-layer near the np-junction provides an extended region of constant space charge (subfigure F) and permits the use of the Schottky approximation (linear field distribution) here, which can be employed to estimate the minimum necessary bias to reach current saturation.

Intrinsic losses in relation to *open circuit voltage* are more difficult to analyze. Previous attempts have resorted to the diode equation, assuming an already highly simplified model. Only recently[21] was a sufficiently accurate numerical analysis of the complete set of transport, continuity, and Poisson equation throughout the entire cell performed to permit some categorizing such losses. We have given some key elements of the analysis in the previous section. They can best be followed when plotting the band model with computed quasi-Fermi levels as shown in the previous figures when neglecting surface recombination (all examples assumed $j_n = j_p = 0$ at both surfaces). The recombination overshoot identified there causes the flow of generation/recombination currents, hence losses of V_{oc}: the computed V_{oc} is less than the one calculated from the simple model given in Eq. (28).

Such recombination overshoot is caused by the fact that the minority carrier distribution in the junction is controlled by the majority carrier, i.e., by the built-in field created from the space charge which is produced by the majority carrier. In thermodynamic equilibrium, drift and diffusion currents of each carrier are equal to each other (and have opposite signs) at each point of the device; here generation is equal to recombination at each point. In steady state (with light) and open circuit condition, this is no longer fulfilled. The density of minority carriers is substantially *increased* (with little change of majority carriers), thereby *decreasing* the gradient of the minority

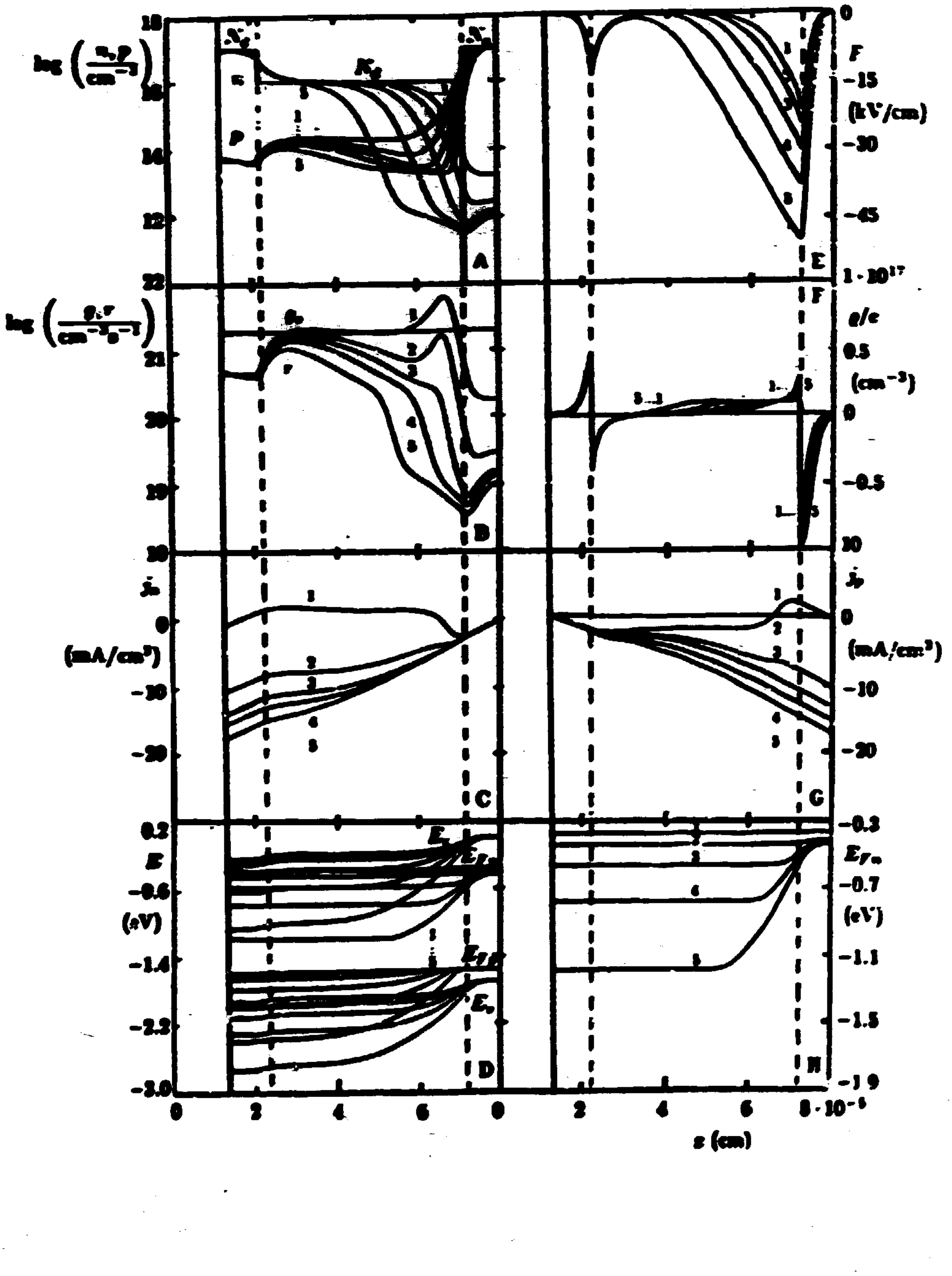

Figure 24: Solution curves for an a-Si in Fig. 22 however, for low compensation (N_{dl} = 10^{16} cm^{-3}) with the total current as family parameter for j = 0, −10, −13, −15, and −18 mA/cm^2 for curves 1–5 respectively.

carriers, i.e., decreasing the diffusion current of the minority carriers which no longer can compensate the drift. The resulting net minority carrier current is now compensated by a net majority carrier current, the generation/recombination current, causing a loss in V_{oc}.

This is the minimum unavoidable loss, the magnitude of which changes with the density of recombination centers, doping density and other cell parameters and were indicated in Fig. (18) for a simple pn-junction.

In addition, there are losses near the junction interface because of an increased density of recombination centers (donor/acceptor pairs) due to unavoidable cross-doping, and at the surfaces due to surface recombination (with a recombination velocity $s \simeq v_{rms}$ expected at every metal surface). An analysis of the influence of the surface recombination is most interesting.

3.2.5 Asymmetric Thick Si-Solar Cell as Example for Surface Recombination Losses. We now extend the analysis to an asymmetrically doped Si-solar cell with a thin, heavily doped n-type front layer and a very thick ($d_2 > L_n$) p-type base which is not protected from surface recombination at the back electrode. The set of solution curves is plotted in Fig. 25 for open circuit conditions. This figure contains a broken scale at $2.5 \cdot 10^{-5}$ cm (see arrow on top for emphasis) in order to show the behavior in the bulk, which contains several interesting features.

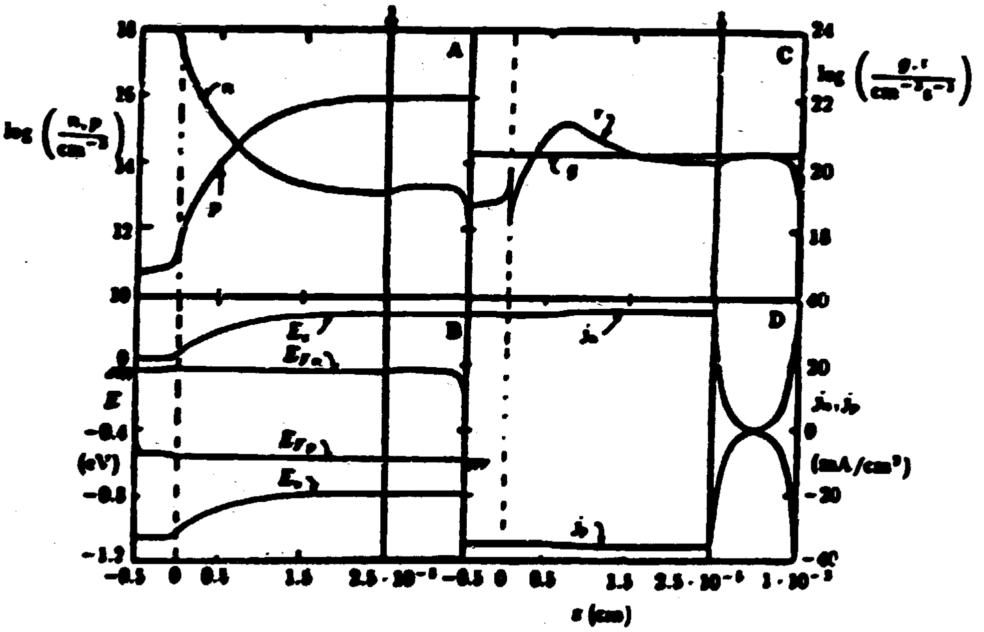

Figure 25: Solution curves of a long asymmetric Si pn-device with complete surface recombination at both electrodes for $g_{opt} = 2\cdot10^{20}$ cm^{-3}s^{-1}, $N_{r1} = 10^{17}$ cm^{-3}, $N_{r2} = 10^{16}$ cm^{-3}, and $c = 10^{-9}$ cm^{-3}s^{-1}.

The minority carrier density is non-monotonic, indicating electron diffusion towards the region of the recombination overshoot near the junction (subfigure C) and electron out-diffusion for recombination at the outer electrode (indicated by the negative slope of $n(x)$ near the right outer surface in subfigure A). In the bulk the electron density has increased close to its steady state value ($g_{opt}\tau_{n0} = n_{10}$), consequently making the recombination rate nearly equal to the generation rate and causing there a vanishing generation/recombination current (subfigures C and D).

Closer to the right outer surface the recombination current changes sign (subfigure D) where the electron density decreases towards the thermodynamic equilibrium value. The near-bulk recombination rate decreases below g_{opt}, creating a net generation rate to approach $U = g_{opt}$, and consequently the slope of the recombination currents rapidly increases to $dj_n/dx = -dj_p/dx = eg_{opt}$.

Because of the large width of the p-type bulk near the right electrode, a large current (near saturation current for the assumed optical generation rate*) for each carrier is accumulated:

$$-j_p(d_2) = j_n(d_2) \simeq eg_{opt}L_n \simeq 40\ \mathrm{mA/cm^2}. \tag{33}$$

This current is dissipated as recombination current at the electrode surface with

$$j_n(d_2) = e\{n(d_1) - n_{20}^{th}\}s \simeq en(d_1)v_n^*, \tag{34}$$

requiring a density of minority carriers of $n(d_1) \simeq 4 \cdot 10^{10}\ \mathrm{cm^{-3}}$, which is substantially larger than the thermal equilibrium density of $n_{20}^{th} \simeq 200\ \mathrm{cm^{-3}}$. Therefore, one observes a decrease of the minority quasi-Fermi level near this surface, however, with a remaining substantial jump

$$E_{F_n}(d_2) - E_F = kT \ln \frac{n(d_1)}{n_{20}^{th}} \simeq 0.5\mathrm{eV}. \tag{35}$$

The majority quasi-Fermi level shows no significant jump† at $x = d_2$ due to the negligible difference in *majority* carriers of $\Delta p \simeq 4 \cdot 10^{10}\ \mathrm{cm^{-3}}$ compared with the thermal equilibrium value of $p_{20}^{th} = 10^{16}\ \mathrm{cm^{-3}}$, which is necessary to maintain the same recombination current of $j_p(d_2) = -j_n(d_2)$.

At the left electrode the situation is somewhat different. Only a very thin layer of n-type material is available. Here the minority carrier density continues to decrease immediately after passing through the junction. This decrease towards the thermal equilibrium value occurs as rapidly as out-diffusion towards the left electrode will permit. This is controlled by the minority carrier current now provided from the near-junction region, a current which was accumulated in the bulk of the p-type material (i.e., approximately 35 mA/cm^2 because of additional recombination in the recombination overshoot region of the junction). Again a jump of the minority carrier density at the electrode surface occurs which can be calculated with a relation corresponding to Eq. (34), however here for holes. The jump is of the same order of magnitude as the

---

* For simplicity we have here assumed homogeneous optical generation. In actual practice the generation rate decreases towards the back electrode, making this recombination current considerably smaller for devices with a thickness larger than the diffusion length.

† From $E_F - E_{F_p} = kT \ln[(p_{20} + \Delta p)/p_{20}]$, one obtains for this jump of the *majority* quasi-Fermi level approximately 10^{-6}eV.

corresponding jump at the right electrode. A concurrent jump of the minority carrier quasi-Fermi level of ~ 0.5 eV therefore occurs also at the left electrode.

The combining effect of minority carrier leakage to the left electrode and excess recombination because of the recombination overshoot in the junction reduces the split of the quasi-Fermi level from* 0.654 eV to the computed split of 0.533 eV.

3.2.6 Fillfactor Losses. Losses in the *fillfactor* are more difficult to analyze. For this, the current voltage characteristic needs to be computed near the maximum power point by introducing the net current as a parameter in Eqs. (13) and (14) ($j_n + j_p = j$) and computing the resulting voltage drop across the device.

Often a low fillfactor is caused by intrinsic cell problems due to deep trap release. This can be identified experimentally by a hysteresis when the jV-characteristic is traversed in forward and reverse direction[22]. The recombination overshoot discussed before also causes a reduction in fillfactor.

As indicated earlier, fillfactor losses can also be caused by series resistance limitation, mostly due to insufficient gridding (upper surface electrical contact), or to shunt resistances, mostly occuring in polycrystalling cells with pinholes. However, the observed fillfactors for better solar cells (Si and GaAs) of typically 80–85% are close to the theoretical limit of 84.7% for Si and of 88% for GaAs derived from the ideal diode equation (Eq. (6)) for the expected values of j_{sc} and V_{oc}. Losses through *parasitic resistances* can be neglected in better solar cells.

4 Solar Cells and Modules

We will now discuss specific solar cells in more detail.

4.1 Single Crystal Si Solar Cells.

Silicon is an indirect band-gap material requiring a relatively thick (typically 0.2mm) cell to absorb most of the active height in the solar spectum (after using light trapping by appropriately structuring the surfaces). The geometry and band model of a typical npp^+-Si solar cell† is shown in Fig. 26.

Sufficient doping of the base is necessary to permit a large open circuit voltage (the majority quasi-Fermi level for holes is then shifted close to the valence band-edge). In addition, a large lifetime of minority carriers is necessary to move the quasi-Fermi level for electrons close to the conduction band. However, Auger recombination[23] limits the doping density to ~ 10^{17} cm^{-3}, and therefore limits[24] V_{oc} to approximately 0.68 V. By increasing the minority carrier diffusion length to values well in excess of the cell thickness and reducing recombination at the back contact by using a back surface field

---

* This split must be calculined at the lower doped region.

† More efficient solar cells are produced by making the region of major generation of minority carriers p-type since for most materials the mobility of electrons is larger than the mobility of holes, causing a larger diffusion length, which is responsible for carrier collection.

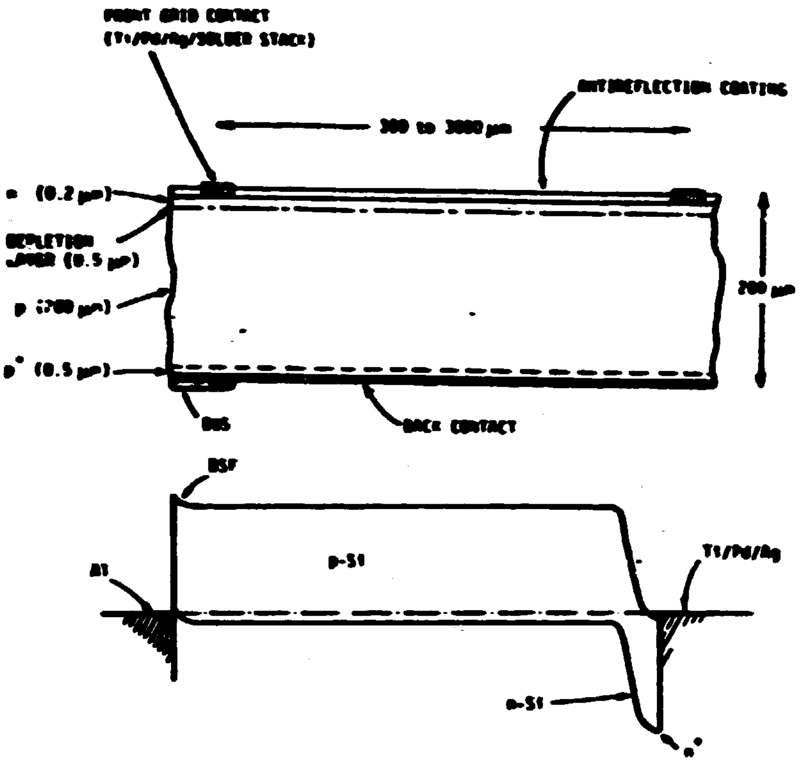

Figure 26: A: Cross-section; B: Band model of a npp^+ Si solar cell after Fahrenbruch and Bube[11].

(using an Al back contact with Al-diffusion into a thin layer during a 15 minute heat treatment at 500–800°C) one obtains also high current collection efficiencies and achieves cell efficiencies of typically 14%[25].

By reducing the thickness of the front n-layer and the density of recombination centers there and in the pn junction, the blue/violet response is raised and the efficiency improved beyond 15%[26]. Further substantial improvements of the current was achieved by etching the front surface to reduce reflectivity and create light trapping (velvet effect[27]) with efficiencies in excess of 17%.

After almost a decade with little further progress, Green and coworkers[28] have pushed the efficiency of the single crystal Si-cell well above 20% by further reducing the recombination at the front surface (by introducing a thermally grown SiO_2 layer (Fig. 27A)), by separating the front electrode through a thin SiO_2 layer (Fig. 27B), or by reducing the contact surface through such a layer (Fig. 27C), thereby increasing the open circuit voltage to 694 mV (AM0, 25°C). When surface etching is also applied to reduce reflection and cause light trapping (Fig. 28), Green[28] achieved 20.9% efficiency at AM1 with indication that still higher efficiencies can be expected realistically with this type of device design.

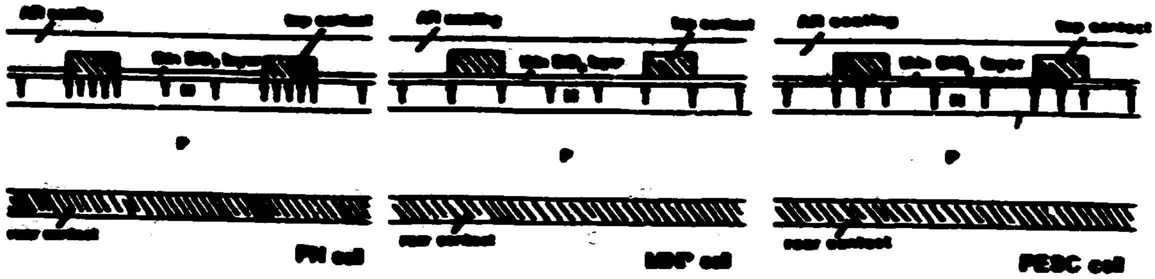

Figure 27: The use of a thin SiO$_2$ layer to reduce upper surface recombination (A) and recombination at the front electrode (B and C) after Green et al.[28]

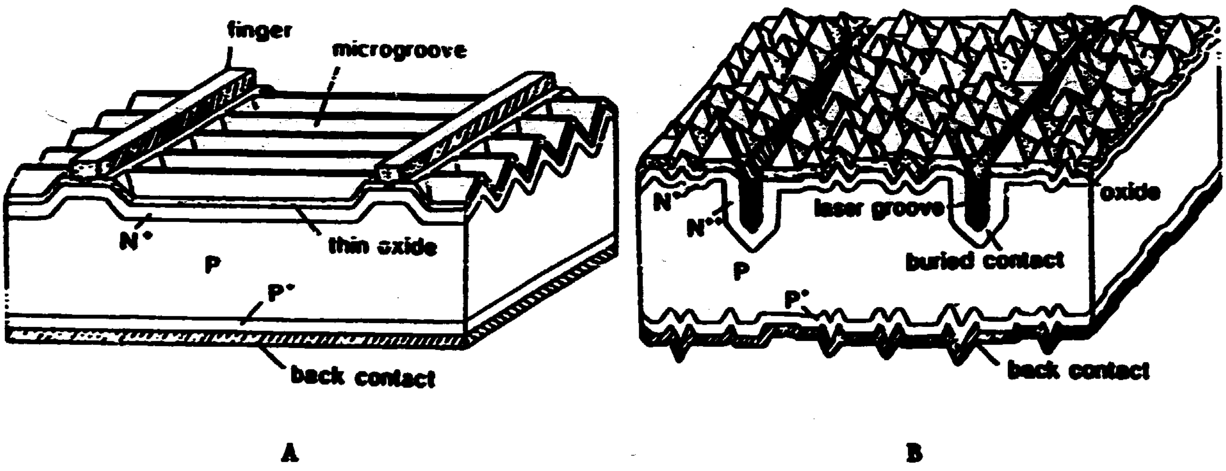

Figure 28: High efficiency Si solar cells with parivated and structured surface to reduce surface recombination and achieve light trapping. Deep, vertical contacts (B) reduce shading effects.

Very recently a research group at the Department of Material Science at Stanford University under Swanson[29] has further developed the idea of an intedigitated back contact[30] and has been successful to further increase the conversion efficiency of Si-solar cells by a significant step to 23% after redesigning the cell geometry radically. In conventional cells a fraction of approximately 5% of light is lost because of grid shading from the top electrode. Another, not yet specified fraction is lost because of recombination at the extended back contact. Both losses can be eliminated or substantially reduced by alternatingly providing carrier collection via small n$^+$ and p$^+$-type "dots" at the back-side of the device[31] with alternating metal contacts, as shown schematically in Fig. 29*. The actual geometry of the back-contact can be obtained from Fig. 30 (the cell is turned around; light impinges from below).

---

* With concentration these cells have achieved 25% conversion efficiency at 150 suns[32] and recently 27% at 900 suns[7].

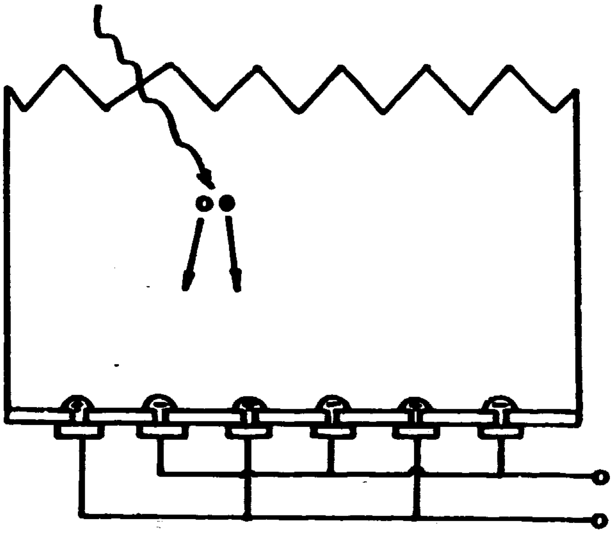

Figure 29: Schematic of the electrode arrangement in the Stanford high-efficiency Si-solar cell.

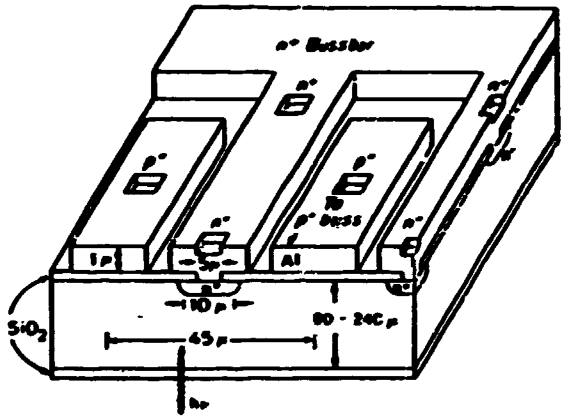

Figure 30: Geometry of the back point contacts of high-efficiency Si solar cells after Swanson.[31]

The *theoretical limit* for the attainable efficiency in Si solar cells depends on a variety of factors, such as

- the spectral distribution of sunlight which varies with the solar elevation and the composition of the earth atmosphere[33];
- the losses of excess energy due to light with $h\nu > E_g$;
- light not absorbed to produce free electron/hole pairs for $h\nu < E_g$;
- the ratio of the achievable spread of the quasi-Fermi levels (V_{oc}) to the bandgap;
- the fill-factor;

- the collection efficiency;
- the losses due to reflection and shading; and
- other (geometry related) losses due to cell defects.

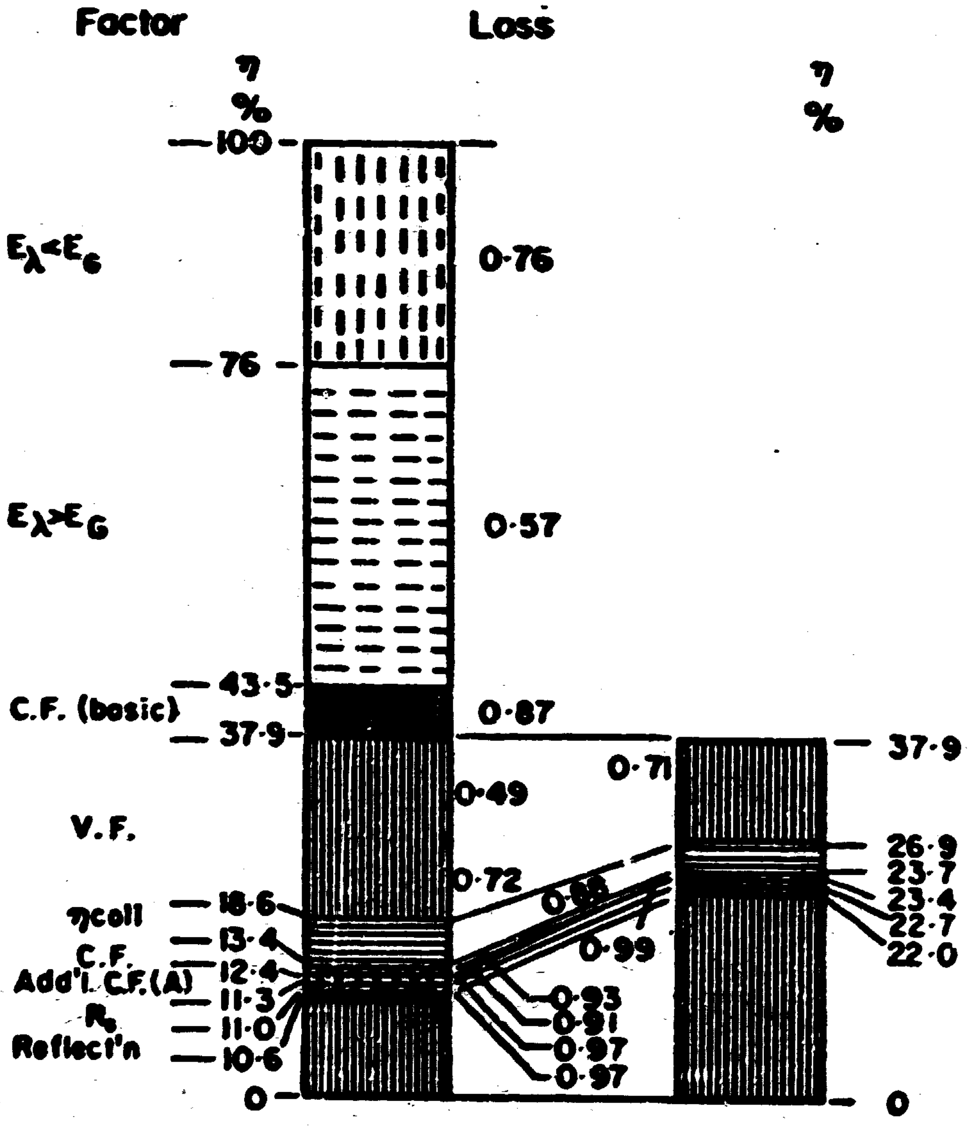

Figure 31: Bar chart of the various energy losses in the best 1971-Si solar cells and the potential for improved Si solar cells after Wolf[63].

These losses were evaluated in a number of papers*, e.g., by Wolf[36] in a detailed accounting for each of the major loss factors and arriving at a bar chart for the actual and for a best projected device (Fig. 31).

The example of the present best Si-solar cell (23% efficiency)[29] exceeding the "improved Si solar cell" estimate of Wolf indicates the need for careful updating of the loss analysis. This includes a new evaluation of the solar spectrum influencing the two upper bar segments and a reevaluation of the fillfactor. The product of the three factors seems to be a few percent low for AM1 illumination (updates to 42%). The voltage factor $(E_{F_n} - E_{F_p})/E_g$ appears to be realistic in the light of our present knowledge about the recombination overshoot. The collection efficiency and the fillfactor modifiers, however, should be upgraded, both to 95%. Series resistance losses are negligible, reflection and shading losses may be a bit optimistic and probably should remain at 5%. This would result in a maximum efficiency of 27% at AM1. It is, however, not impossible by further parameter optimization to increase the voltage factor. Here further research efforts are encouraged.

At higher illumination intensities (with a concentration factor X) the voltage factor increases, as the open circuit voltage rises with $(kT/e)\ln X$, i.e., by 179 mV at a concentration factor of 1000. However, now series resistance limitation becomes significant, reducing the fillfactor; hence best conversion efficiencies have not yet exceeded 27% at $X = 900$ in Si solar cells[29].

How realistic the above given estimates are can only be judged after extensive additional material science studies including more work on Auger recombination and on donor-acceptor pair recombination to design Si with a high minority carrier lifetime yet with high acceptor doping. Such high doping will diminish the effectiveness of the back surface field, and therefore may require additional steps in device design†.

4.1.1 Si-Material*. Presently there are two trends discernable: to develop and produce low cost raw Si material which is useful for cells with modest efficiency (in the 10–16% range), or to develop ultra-high efficiency devices irrespective of the present cost of the raw material, however assuming that a reasonable modification of the material production process could yield the necessary material for such high efficiency devices without adding significantly to the cost.

At this time *semiconductor-grade* Si is used to produce Si-solar cells. This Si is made by the Siemens process in a quantity of a few thousand metric tons/year‡ at a price in excess of $70/kg. Several alternative processes have been studied, capable in

---

* A more general estimate of maximal conversion efficiencies were obtained by Shockley and Queisser[34] using thermodynamic reasoning.

† It is, however, remarkable that present best Si-solar cells have approached theoretical limit efficiency rather closely. On a different note it should be pointed out that the best currently achieved solar cell efficiencies are not far away from power utility efficiencies using conventional fuels.

‡ At an estimated use of 5 metric tons/MW, a substantial fraction of this production would be needed for solar cells in 1986 with a projected production rate of 50MW/y world wide.

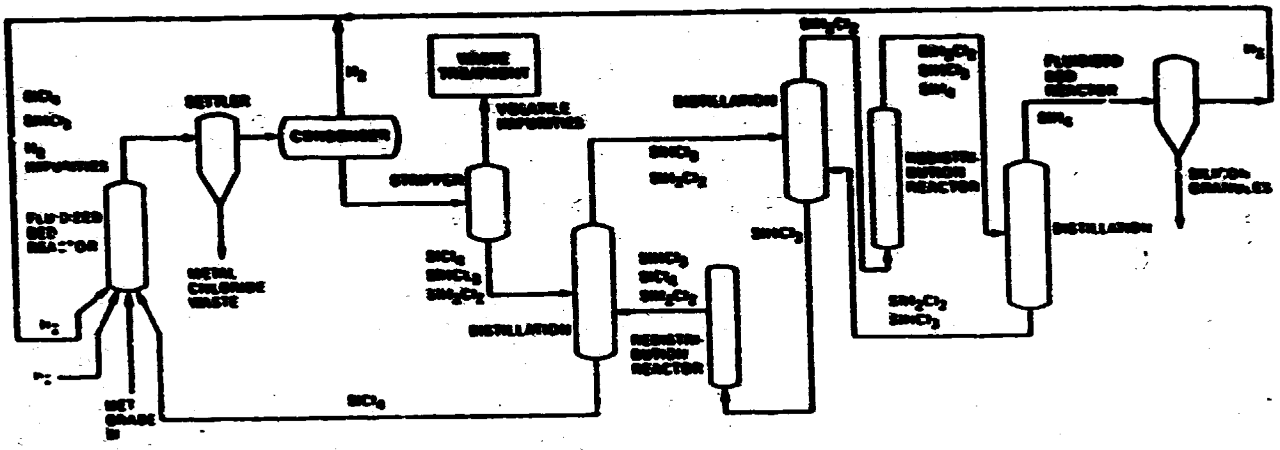

Figure 32: Union Carbide silane process flow diagram.

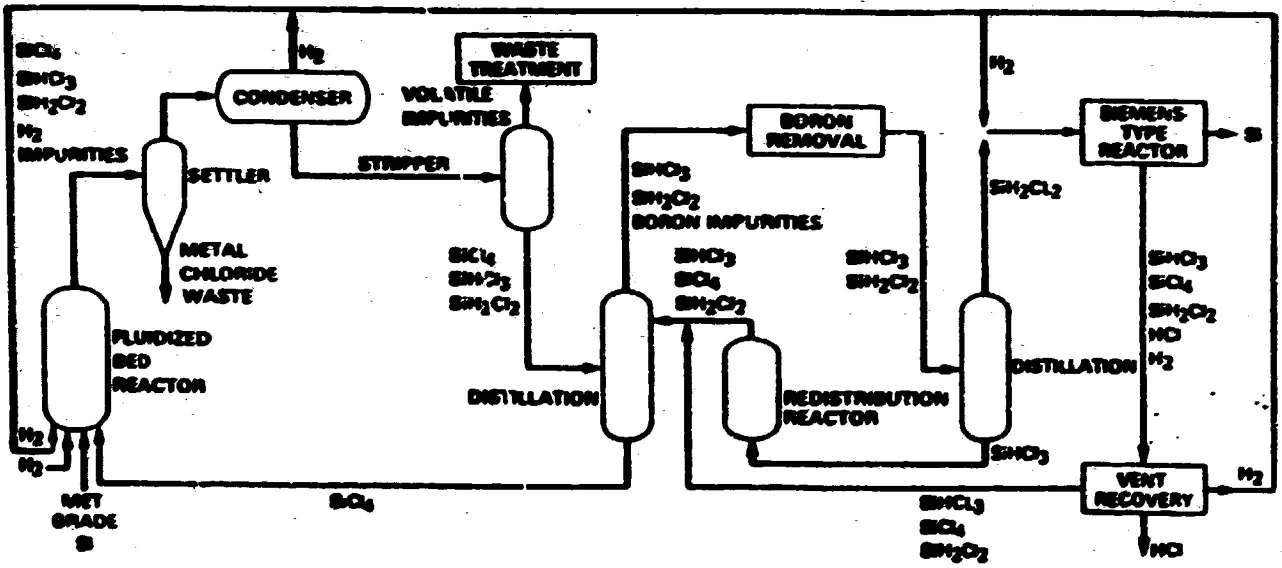

Figure 33: Hemlock semiconductor dichlorosilane process flow diagram.

producing solar grade Si (a material with slightly higher impurity concentration, but capable to yield modest efficiency solar cells) at a cost of less than \$20/kg.

One of the processes is based on Silane rectification and is already developed through pilot (100 mt/y) and production plant (1,200 mt/y) by the Union Carbide Corp. Another 1,200 mt/y plant is in construction and a 3,000 mt/y plant is in design. The flow diagram of the Silane process is shown in Fig. 32; it is capable of producing solar cell grade silicon at a cost below 20 \$/kg.

Another process is being developed by the Hemlock Semiconductor Corporation in the USA and based on the dichlorosilane process shown in a flow diagram in Fig. 33. The feasibility of this process has also been demonstrated in a process development unit. The process, however, is estimated to be slightly more expensive (35 $/kg) than the silane process and subject to some autoignition hazard, which can be minimized by proper factory design (avoiding the storage of dichlorosilane).

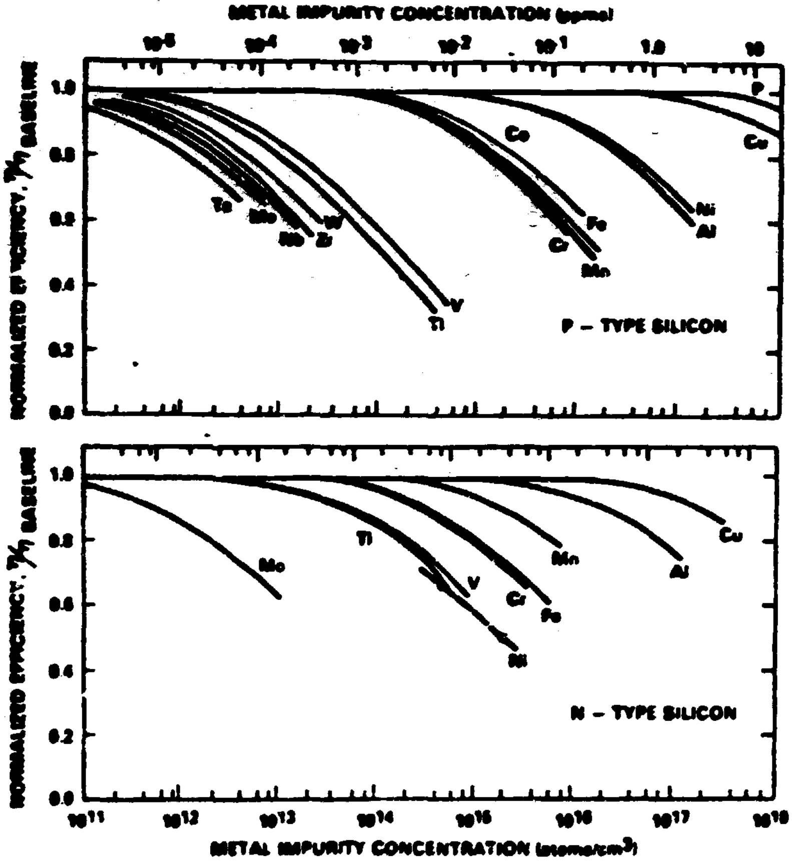

Figure 34: Sensitivity of the relative cell efficiency in respect to concentration of typical impurities in n- and p-type materials used in cell production.

The rationale behind the development of solar grade silicon is the insensitivity of medium efficiency solar cells ("baseline" cell) in respect to some typical impurities. Fig. 34 indicates that certain impurities, e.g., Cu and Al in n-type and P and Cu in p-type material, can be tolerated in excess of 1 ppm without major cell degradation. Other elements have to be avoided much more carefully (e.g., transition metals).

It is expected that solar grade Si will become available in the near future and, because of the lower production cost, price elasticity can be expected in due course.

4.1.2 Si Crystal/Sheet Growth*. Substantial reduction in production cost can be achieved by improving the single crystal growth process.

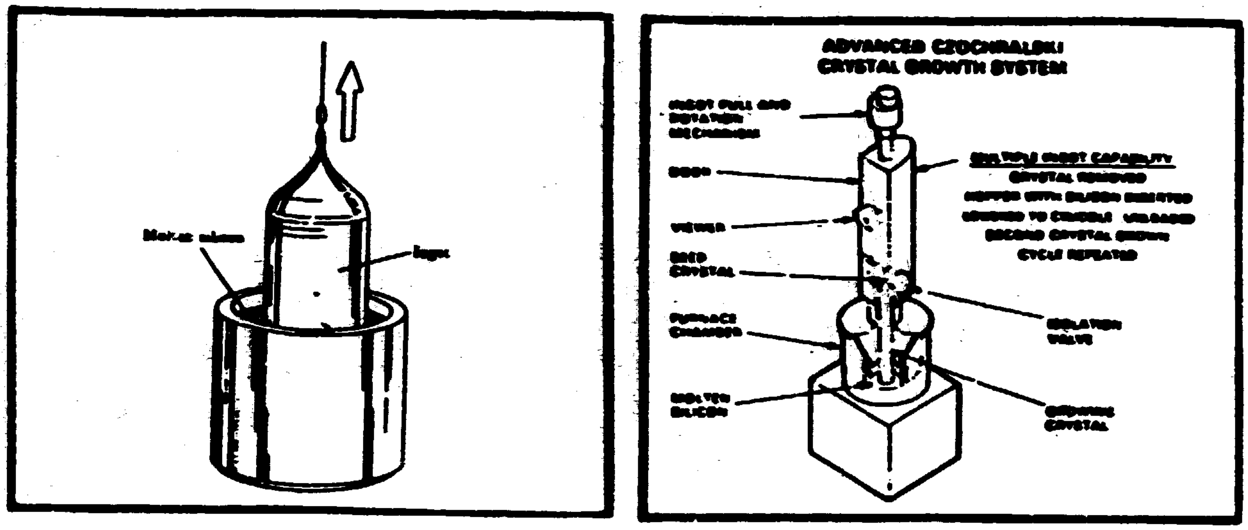

Figure 35: Czochralski growth technique and advanced Czochralski-grown Si by the Hamco Division of Kayex Corp.

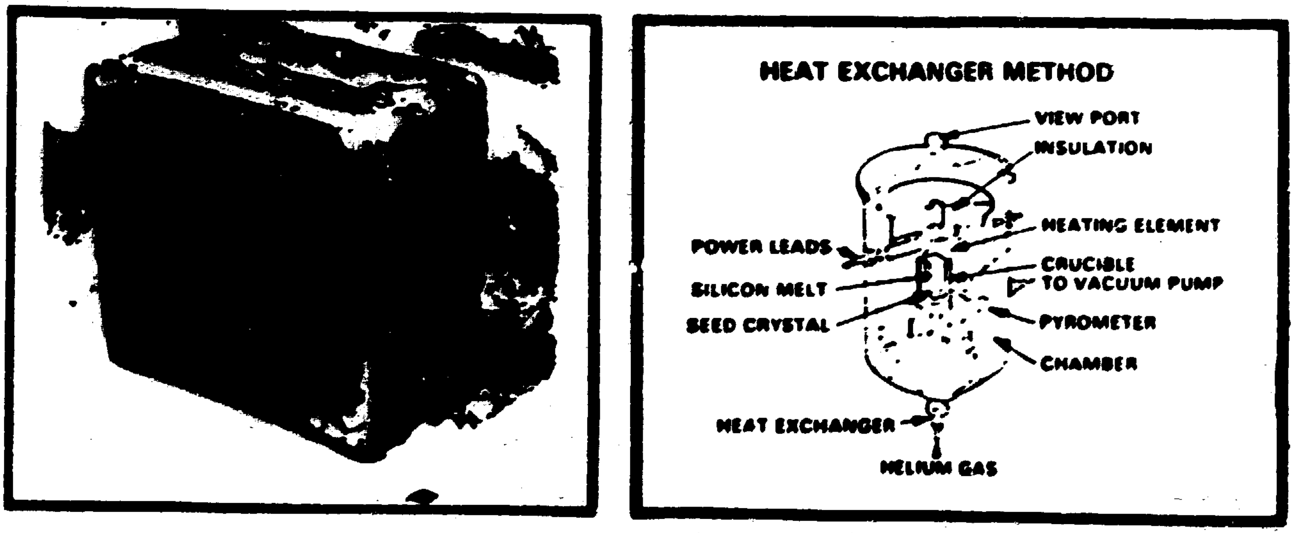

Figure 36: Ingot-casting-by-a-heat-exchanger method, developed by Crystal Systems, Inc.

---

* Examples listed here contain only material available in the open literature.

Figure 37: Semicrystalline high efficiency Si solar cell 10 x 10 cm^2. (Solarex).

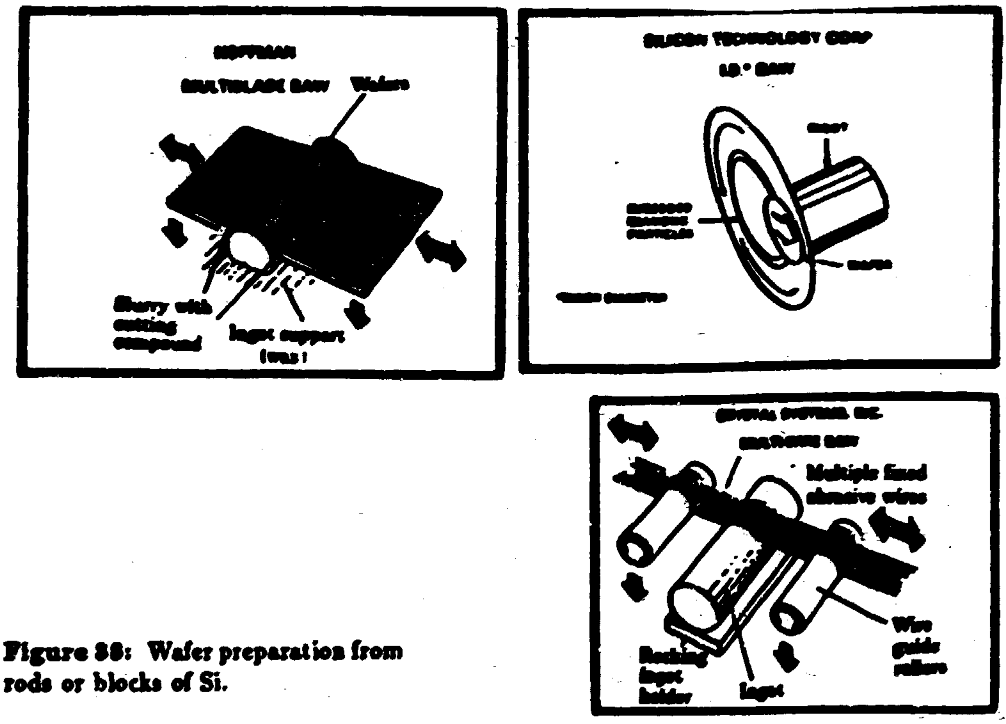

Figure 38: Wafer preparation from rods or blocks of Si.

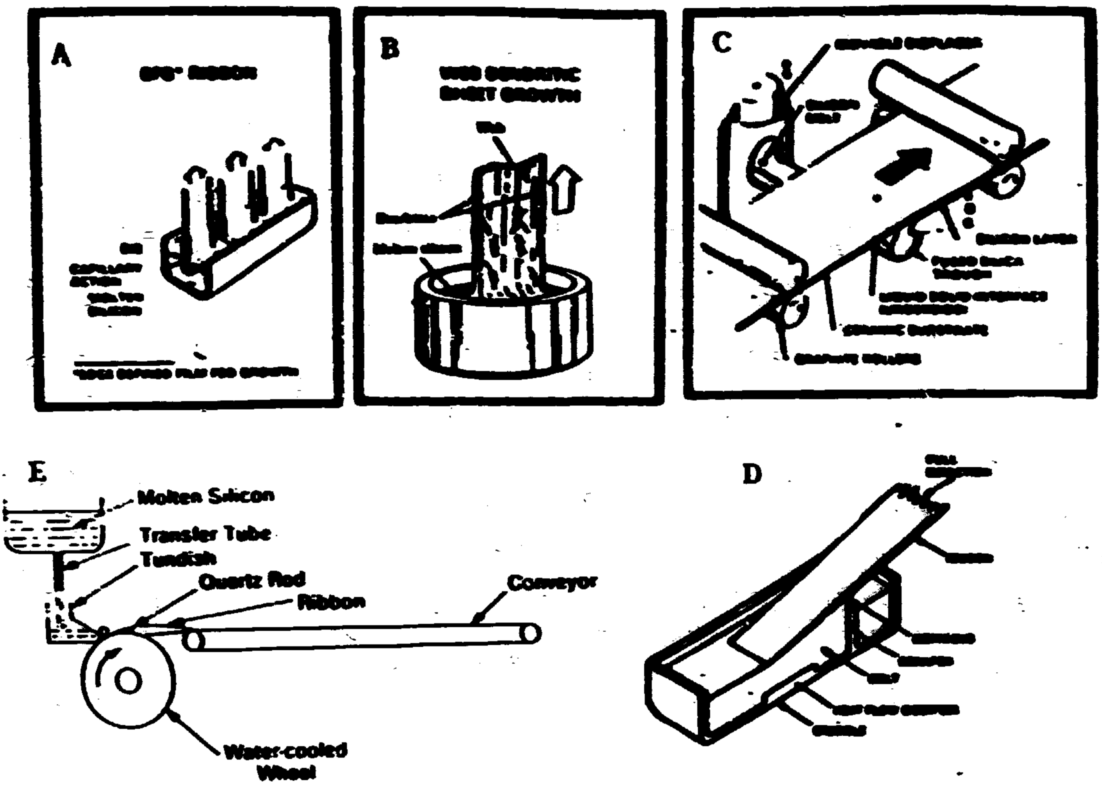

Figure 39: Different sheet growth techniques.

Figure 40: Nonagon growth machine and segment of a grown nonagon.

For instance, in an advanced *Czochralski growth system* of the Hamco Division of the Kayex Corporation, in an automated growth from a 150 kg ingot/cruicible with 2.2 kg/hr throughput, 15 cm rods can be produced yielding 15% efficient solar cells (Fig. 35).

A further cost reduction can be achieved by using *polycrystalline Si* for solar cells, which show moderate efficiencies in the 8–15% range (typical 10% for large quantities) when the grain size exceeds a few mm diameter (Fig. 37) and grain boundaries are appropriately passivated (usually by a H_2 treatment).[36] Examples are the ingot casting by Semix, Inc. and the ingot-casting-by-a-heat-exchanger method of Crystal Systems, Inc. (Fig. 36). Both methods are capable of producing up to 15% efficient solar cells. The Semix process presently produces 20 x 20 x 15 cm^3 semicrystalline blocks with 83% ingot yield at 2.3 kg/hr. The Crystal Systems process produces slightly larger blocks of 34 x 34 x 17 cm^3 which are > 95% single crystal at 1.9 kg/hr with > 95% yield.

Process variability, non-uniformity of grains, and non-uniformity of impurities still influence adversely the yield of cells with acceptable efficiencies from polycrystalline material.

All of these rods or blocks need to be sawed into thin wafers. Several methods, as shown in Fig. 38, are presently being developed. Best present achievements are a slicing of 17 wafers from a 15 cm rod and 20 wafers from a 10 x 10 cm^2 cast block per cm length at a rate of 0.4 and 1.2 wafer/min respectively at 95% yield. The finished wafer area per kilogram of ingot is 0.7 and 1.0 m^2/kg respectively. Surface damage due to the sawing requires substantial etching to remove these damaged layers. The resulting material losses are additional cost factors which present a substantial handicap to the above listed methods.

Major advances can be achieved by direct growth of *Si-sheets*. Several methods to produce such sheets are being developed; some results are available in the open literature and are listed below.

The *edge-defined film-fed ribbon* growth developed by the Mobil Solar Energy Corp. has achieved a respectable 40 cm^2/min growth of 10 cm wide ribbon, simultaneous multiribbon growth of 3 ribbons @ 10 cm width or 5 ribbons @ 5 cm width with 0.15 mm ribbon thickness and 80% yield of cells with >12% efficiency (Fig. 39A). More recently a nonagon growth technique was developed in which a hollow, polygonal shaped tube of 150 mm diameter is grown with nine flat sides, each one 50 mm wide and 0.3 mm thick and later cut into rectangular blanks (Fig. 40). These nonagons can be grown to an impressive light (Fig. 41).

The *dendritic* web growth developed by the Westinghouse Corp. can produce 13 cm^2/min for short ribbon lengths, which yield somewhat higher efficiencies (best achieved[37]: 16.9%) (Figs. 39B and 42). The history of the recent web development is given in Table 4. The status of the technology in industrial Si sheet development can be seen from Table 5.

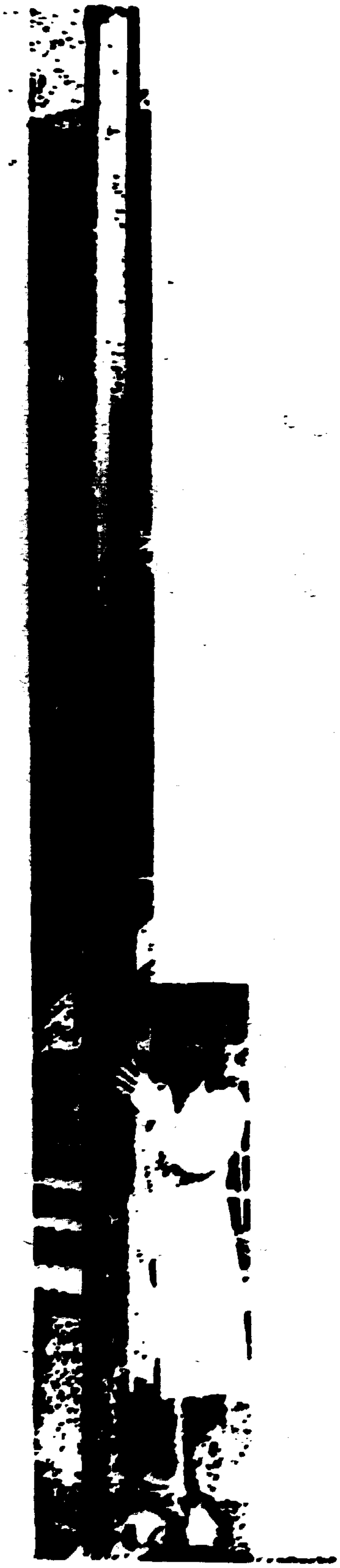

Figure 41: Si-nonagon continuously grown by Mobil Solar.[38]

Figure 42: Dendritic web silicon ribbon progress from 1968 to 1978 in Westinghouse Electric Co. pilot plant.

Table 4: Dendritic Web Development.

Development	1977	1978	1979	1980	1981	1982	1983	1984	Mar 1985
Area Growth Rate, cm^2/min									
1) Transient (Lengths Of Several Centimeters)	2.3	8	23	27			42		
2) Quasi-Steady-State (Lengths Of 30 To 100 cm)					7	13			
3) Steady-State (Meters Of Length, Hours Of Growth)					4	8			
Maximum Undeformed Width, Centimeters	2.4	3.5	4.0	4.4		5.5	5.8		6.7
W_{150}-Undeformed Width At 150 μm Thickness (An Inverse Measure Of Buckling Stress)		2.0	2.7	3.2		4.9			
Maximum Area Throughput For Single Furnace in 5-Day Week (cm^2/week)								9,000	27,000
Maximum Demonstrated Solar Cell Efficiency, AM1	13	14	15	15.5			15.9	16.2	16.9

Table 5: Si Sheet Development.

SHEET TECHNOLOGY	DIMENSIONS (cm)		THROUGHPUT* (m²/hr)		MATERIAL UTILIZATION m²/kg		SOLAR CELL EFFICIENCY %AM1 ENCAPSULATED	SOLAR CELL EFFICIENCY %AM1 BARE CELL	ADD-ON PRICE $/Wp (1980 $)
	TR GOAL	CURRENT STATUS	TR GOAL	CURRENT STATUS	TR GOAL	CURRENT STATUS	TR GOAL	ESTIMATED* STATUS	TR ALLOCATION
SHAPED SHEET									
EFG**	4 @ 10 WIDE x 0.020 THICK	3 @ 10 WIDE x 0.020 THICK	0.95	0.80	2.15	2.15	12	14	0.285
WEB	—	—	0.10	0.05	<3.2	<3.2	15	16.5	0.282

*HIGHER EFFICIENCY INDIVIDUAL CELLS HAVE BEEN FABRICATED
**NONAGON RIBBON CONFIGURATION FUNDED BY MOBIL SOLAR HAS HIGHER VALUES

Table 6: State-of-the-art Si-sheet Technology.

SHEET TECHNOLOGY	DIMENSIONS (cm)		THROUGHPUT (kg/hr) or (m²/hr)		MATERIAL UTILIZATION m²/kg		SOLAR CELL EFFICIENCY %AM1 ENCAPSULATED	SOLAR CELL EFFICIENCY %AM1 BARE CELL	ADD-ON PRICE $/Wp (1980 $)
INGOT	TR GOAL	STATUS	TR GOAL	STATUS	TR GOAL	STATUS	TR GOAL	ESTIMATED* STATUS	TR ALLOCATION
Adv. CZ	15 DIA	15 DIA	2.5†	2.2†	n.a.	n.a.	15	13.5	0.112
HEM	30x30x15	30x30x17	1.8†	1.8†	n.a.	n.a.	15	11.5	0.104
Semix Casting Process	30x30x10	20x20x15	2.3****	2.3****	n.a.	n.a.	15	11.0	0.245***
Adv. Wafering**	15 DIA & 10x10 SQ	15 DIA & 10x10 SQ	0.53 0.80	0.42 0.75	0.73 1	0.65 1	n.a. n.a.	n.a. n.a.	0.081 0.062
SHAPED SHEET									
LASS	1 @ 15			3.6		3.8	12		
SOC	2 @ 12.5 x 0.010	1 @ 10 x 0.010	2.1	0.3	4.3	4.3	11	9.5	0.100

*HIGHER EFFICIENCY INDIVIDUAL CELLS HAVE BEEN FABRICATED
**DATA GIVEN FOR ID WAFERING. OTHER WAFERING APPROACHES WILL ALTER THE FIGURES
***ADDED VALUE FOR CASTING AND WAFERING
****CRYSTALLIZATION RATE kg/hr

There are other methods to produce directly Si-sheets however, in a somewhat earlier developmental stage. For instance a Si-on-ceramic pick-up from a liquid surface developed by Honeywell produces sheets of <0.1mm thickness and cell efficiencies of 10.5% (Fig. 39C) with a growth rate of 60 cm²/min.

Another method is being developed by the Energy Materials Corp., in which a crystal sheet is picked up from the meniscus of a Si melt (Fig. 39D). This method has achieved a much larger throughput of 450 cm²/min, but at a larger ribbon thickness of 0.64 mm (pull speed 85 cm/min) and ribbon width of 15 cm. Best achieved cell efficiency is 12.9%. Still another method[38] (Wakefield patent) uses liquid silicon poured over a spinning wheel (Fig. 39E) and achieves 0.25 mm thick and 5 cm wide sheets at a rate of 15 m/min Best cells made from such a sheet have 9% conversion efficiency.

Other methods are vigorously being developed and judged promising by the involved industry. It can be expected that with further research and development an improved production reliability (acceptable yield) can be achieved and increased efficiencies in the 17(+)% range can be obtained in a cost efficient production environment. The state-of-the-art in Si-sheet technology is summarized[11] in Table 6.

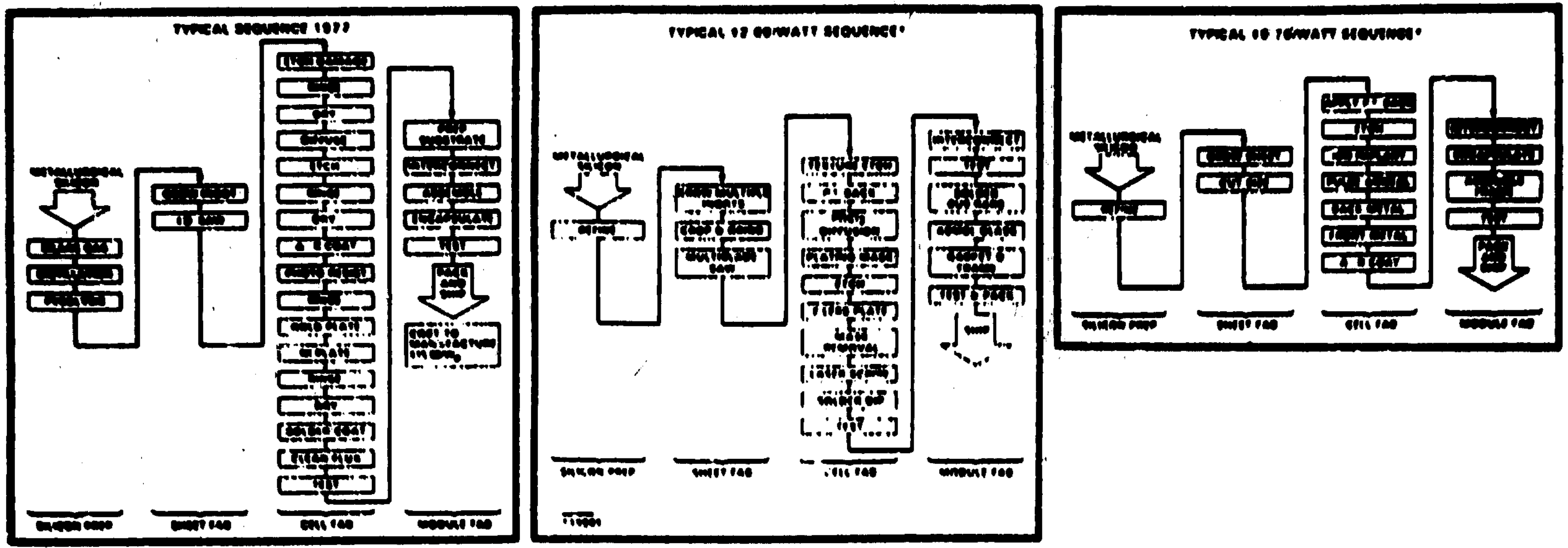

Figure 48: Solar cell and module production process sequences.

4.1.3 Cell and Panel Production. Cell and panel production contains a large number of steps which add costs and reduce overall yields. Streamlining of this production (reduction in steps) and automation are being developed. A typical example is given in Fig. 43 for the conventional and for more advanced production sequences containing some cost estimates in 1980 dollars.

Recent advances are related to the goal of improving the metallization and the overall process yield. They also include further improvement in liquid-dopant processing and in thermal pulse diffusion to produce simultaneously the np- and pp$^+$-junctions. Laser annealing of ion implanted dopants and microwave powered plasma systems are used, the latter to passivate (SiO_2) and to produce antireflective coating (SiN). New means to produce the top electrode, including laser pyrolysis of metallo-organic liquid films[40] (Fig. 44) at the cell surface and printing with newly developed inks (e.g., Mo-Sn) are being developed (narrowest presently obtained linewidth is 3 μm). New interconnecting automatic equipment using ultrasound is employed. A double chamber vacuum lamination is used. Further development of automation in cell production (Fig. 45) is in progress.

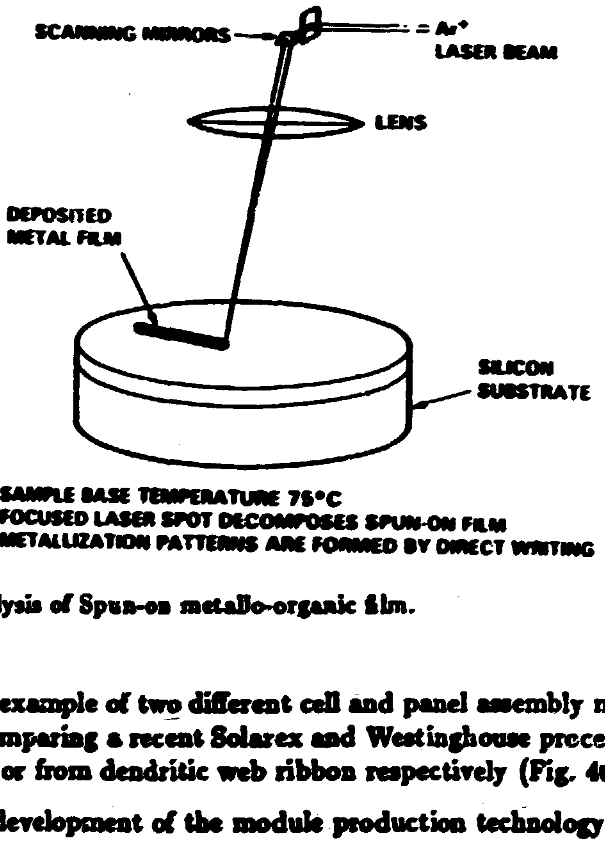

Figure 44: Laser pyrolysis of Spun-on metallo-organic film.

An illustrating example of two different cell and panel assembly methods is given in the flow diagram comparing a recent Solarex and Westinghouse process starting from polycrystalline wafers or from dendritic web ribbon respectively (Fig. 46).

The economic development of the module production technology during the last 12 years is impressive and can be obtained from Fig. 47 for the example of Czocralski grown Si.

Fig. 48 shows some typical *encapulation designs* as they are presently used. Fig. 50 gives some sample panels as they evolved from the early 1970 to the present design with

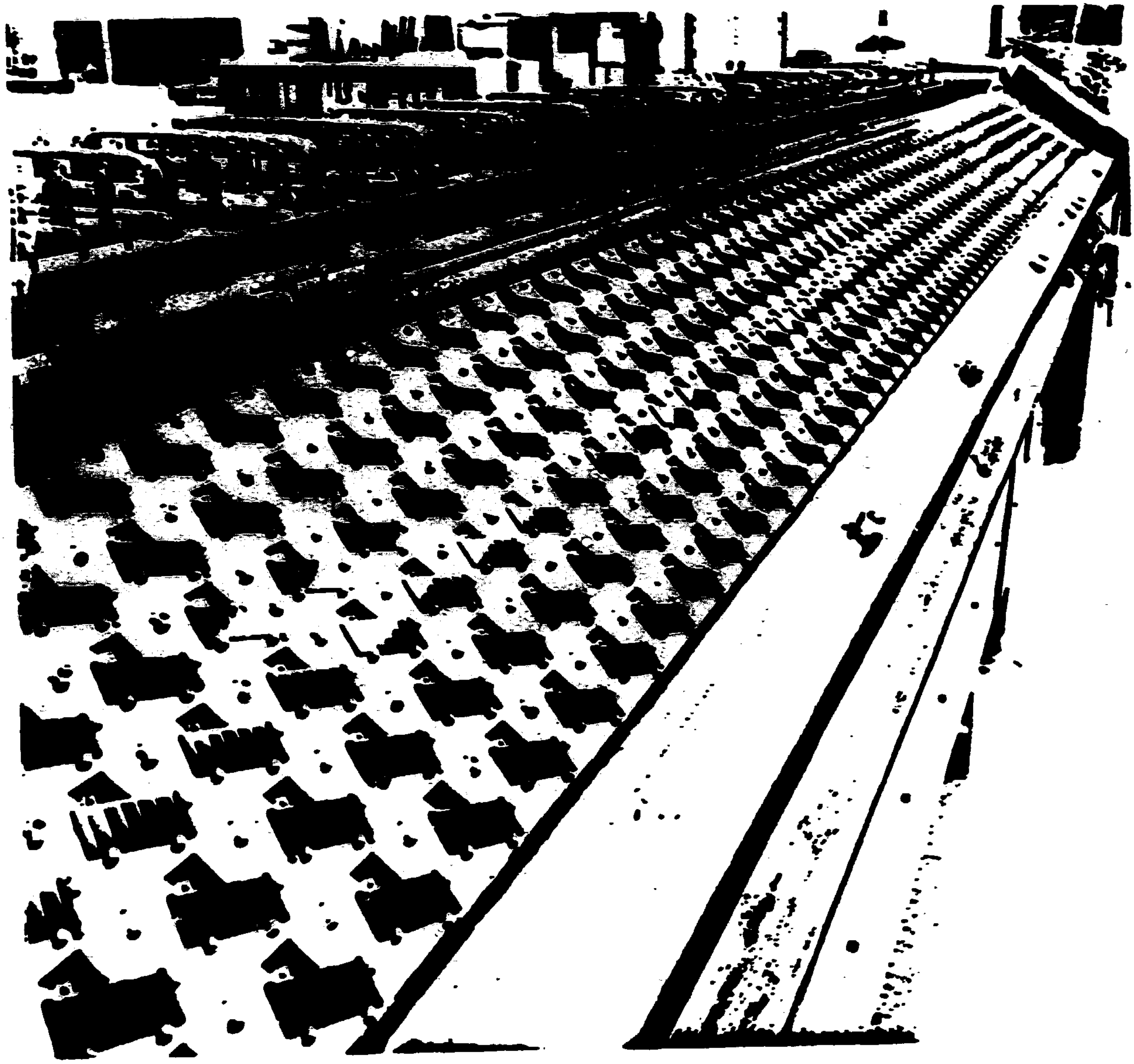

Figure 45: Automation of wafer treatment by TRW.

high packing density and improved edge to edge efficiency (presently up to 12.6%). Overall further development is in progress and a "Strawman" process analysis predicts feasibility of a 2$/W low cost cell and module fabrication, and, when fully automated, a possible 0.75$/W cost (in 1986 dollars).

The updated goals established in 1983 of high efficiency 15% Si modules at a cost of 90$/$m^2$ with 30 years deployed panel life seem to be realistic, although not without additional effort in research and development, but not requiring a technology breakthrough.

The trend in the development of commercially available Si-solar cell panels is shown in Fig. 49 which clearly show the major advances achieved during the last decade,

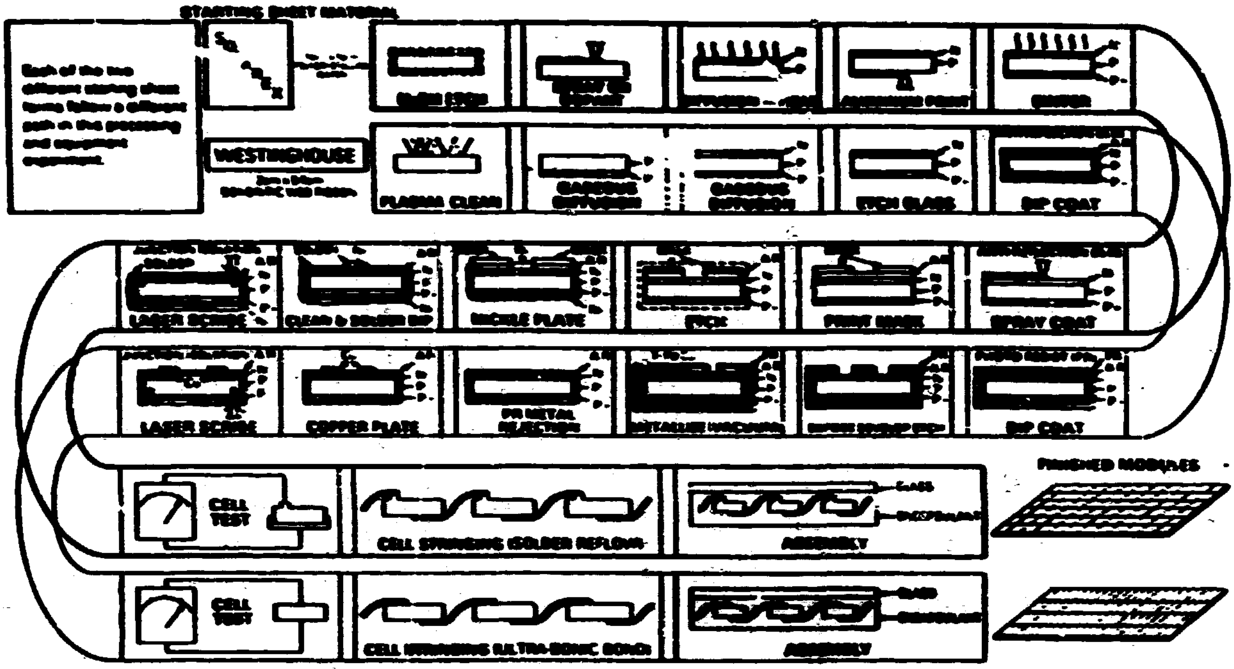

Figure 46: Module experimental process system development unit.

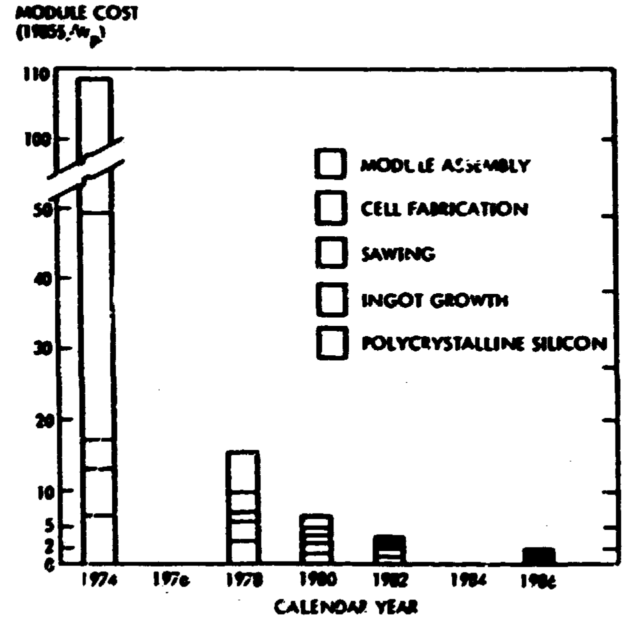

Figure 3. State-of-the-Art Projections For Czochralski Module Technology, 1974–1985

Figure 47: State-of-the-Art projections for Czochralski module technology, 1974–1985.

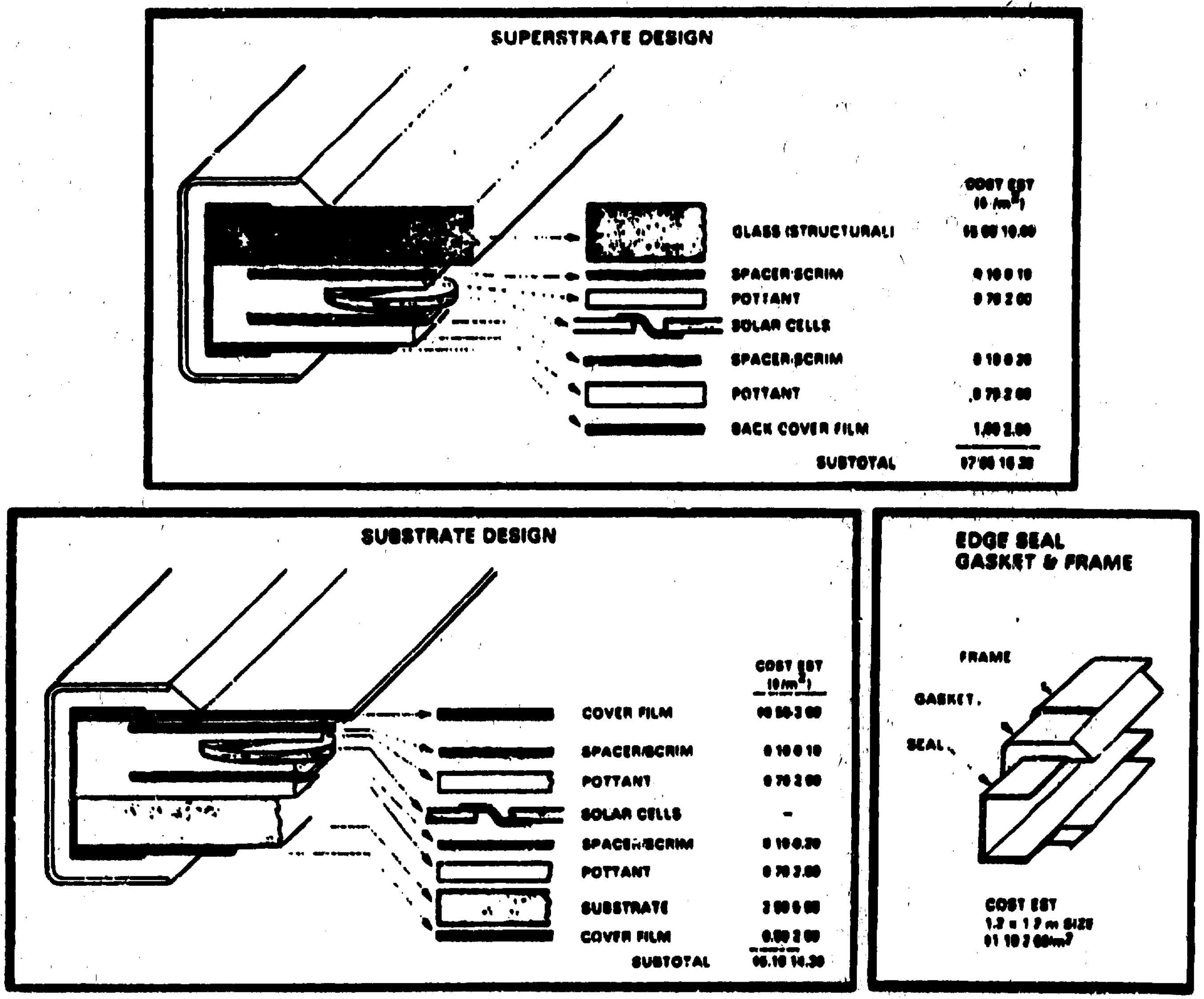

Figure 48: Typical encapsulation design for Si-solar cell modules.

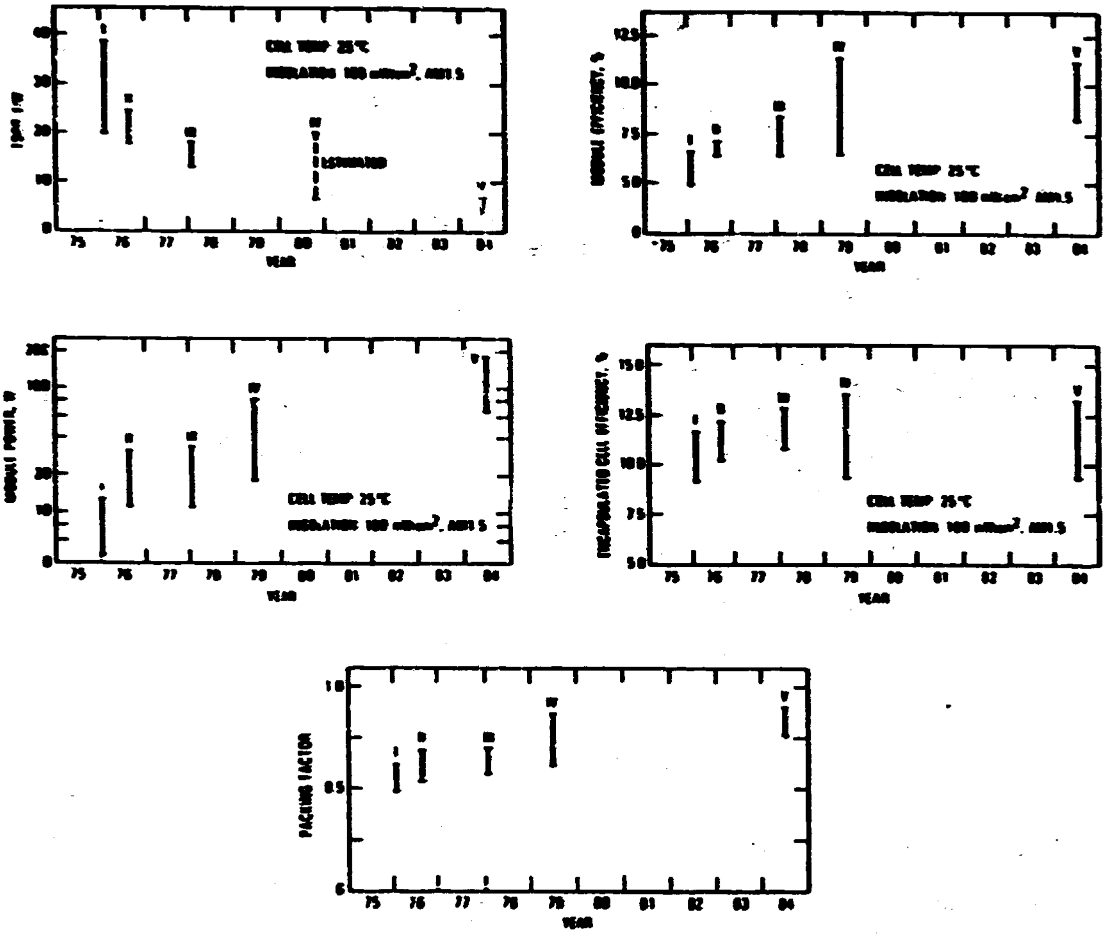

Figure 49: Development trend of commercial Si solar cell panels during the last decade.

most significantly in sales price from an average of 30$/W in 1975 to 5$/W in 1985 (all in 1980 dollar), module efficiency (edge to edge) from 6% to 10% average, and packing factor from 55% to 85%. Significant further progress is expected when high efficiency cells will be used for production units, boosting the persent average 11% encapsulated cell efficiency potentially well above 15%. A variety of solar cell modules as they became commercially available during the last 10 years is shown in Fig. 49.

In summary, there is no doubt that the present achievements in thick sheet Si-solar panel technology will see major improvements during the next few years in terms of panel efficiencies and further significant reduction in panel cost. An idea about a

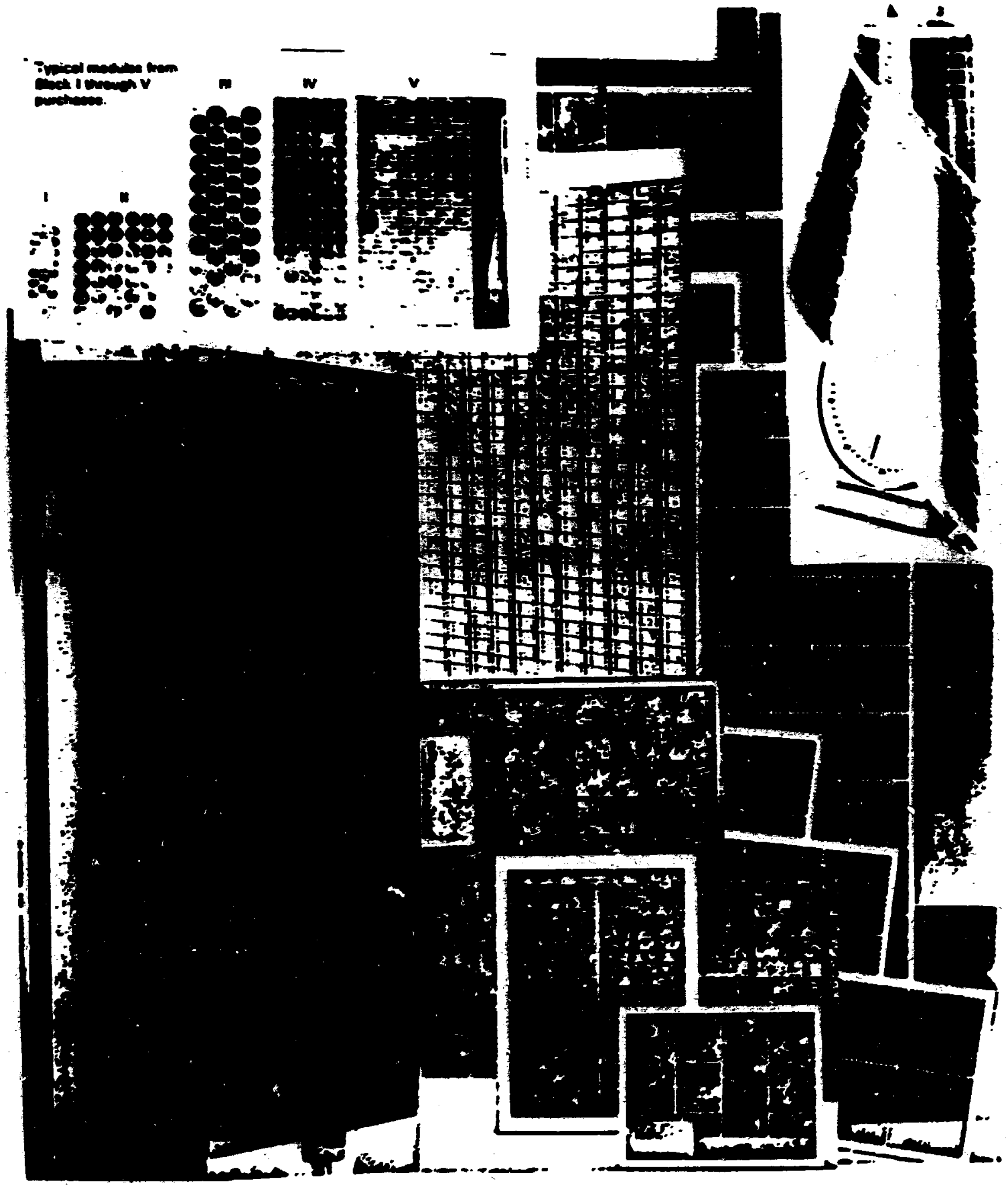

Figure 50: A: Early Si-modules — upper left insert (mid 70)[11]; B: Recent Si-modules (α-Si: ARCO, Sovonics and Sanjo; ribbon: Mobil-Tyco; Poly: Solarex; and Czochralski: ARCO.)

possible price development for large scale procurement (1 megawatt) may be obtained from Table 7[41].

Table 7:

	1984	1986	1990
Modules	6.00	4.00	1.50
Balance of system:			
Power conditioning	0.50	0.30	0.20
Racks/mounts	1.00	0.50	0.40
Wiring	0.20	0.10	0.10
Installation	1.00	0.50	0.40
Engineering/profit	1.30	0.70	0.50
Installed system	10.00	6.10	3.10

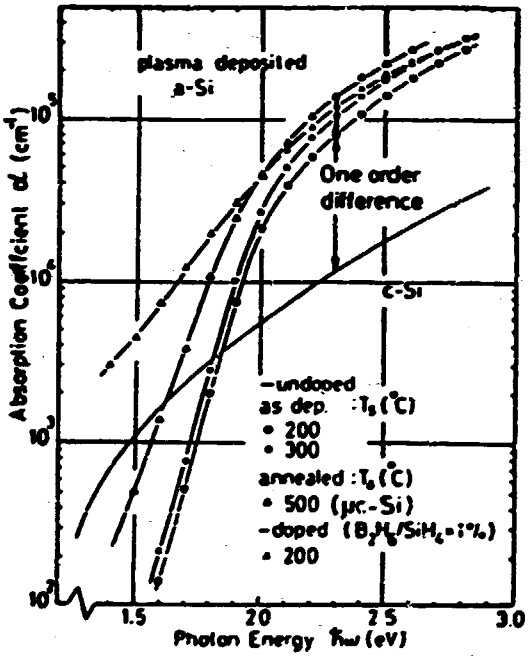

Figure 51: Optical absorption coefficient of α Si in comparison with microcrystalline and single crystal Si after Hamakawa[42].

4.2 The Amorphous Si-Cell.

A substantial improvement of the cost efficiency of solar cells is expected by using amorphous, hydrogenated, or fluorinated Si as the active cell-material[43,44]. It has a much steeper optical absorption edge (behaving like a direct band-gap material) at an energy (~ 1.7 eV) which is better matched to the optical spectrum of sunlight, as shown in Fig. 51.

The amorphous silicon layer can be easily deposited on a large variety of materials acting as the base electrode. Such materials can be thin layers of stainless steel or polyimide films, coated or clad with thin metal layers (total substrate thickness 15 – 40 μm) and may be used to fabricate (flexible) very light weight monolytic photovoltaic modules with the best currently achieved power-to-weight ratio of 2.4 kg/kW.[45]

The deposition is done in a gas discharge and permits via changes in the gas composition a rather simple change in doping and chemical composition of the deposited layer. It requires typical deposition temperatures of 200–300°C, i.e., temperatures which are low enough for the use of inexpensive substrates. The band gap can be changed between ~ 1 and 2.8 eV by changing the host material from Si to SiC, SiGe or SiSn, using mixtures of Silane and Methane, GeH_4 or $Sn(CH_3)_4$, or similar fluorinated compounds with possibilities to produce stacked cells, super lattices* or window layers with relative ease.

Only ten years ago the use of amorphous Si of efficient (>6%) solar cells was shown by Carlson and Wronski[47]. Consequently, the development of such cells with higher efficiencies proceeded rapidly (Fig. 52).

The amorphous silicon can be made n- and p-type by doping, similarly to cystalline Si. However, the α-Si solar cell is distinguished by several principal features from the crystalline Si cell:

- it is about 1000 times thinner since its absorption coefficient is substantially higher,
- its main region of generating minority carriers contains a substantial electric field ($\sim 10^4$ V/cm) to assist collection,
- its band gap lies closer to the optimum value (i.e., near 1.5 eV) for solar energy conversion,
- however, the carrier mobility is $\lesssim 1\ \mathrm{cm}^2/\mathrm{Vs}$, i.e., only ~1/1000 of the carrier mobility in crystalline Si, and
- there is cell degradation which requires careful development of commercially viable solar cell panels.

---

* Alternating thin layers (typically 10-50Å) of different composition. As an example of such alternating deposition, higher and lower band gap α-Si was deposited as the top layer of an α-Si solar cell,[46] thereby increasing the effective band gap to 2 eV and its conductivity, causing an increase in V_{oc} by 50–70 mV.

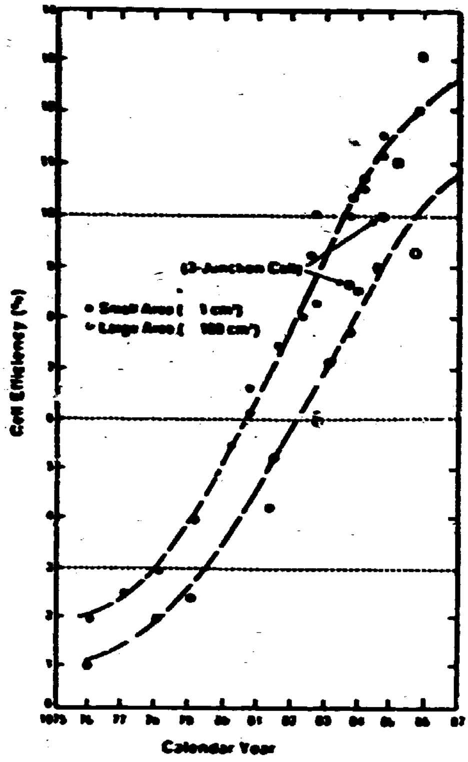

Figure 52: Development of the α-Si solar cell during the last 12 years.

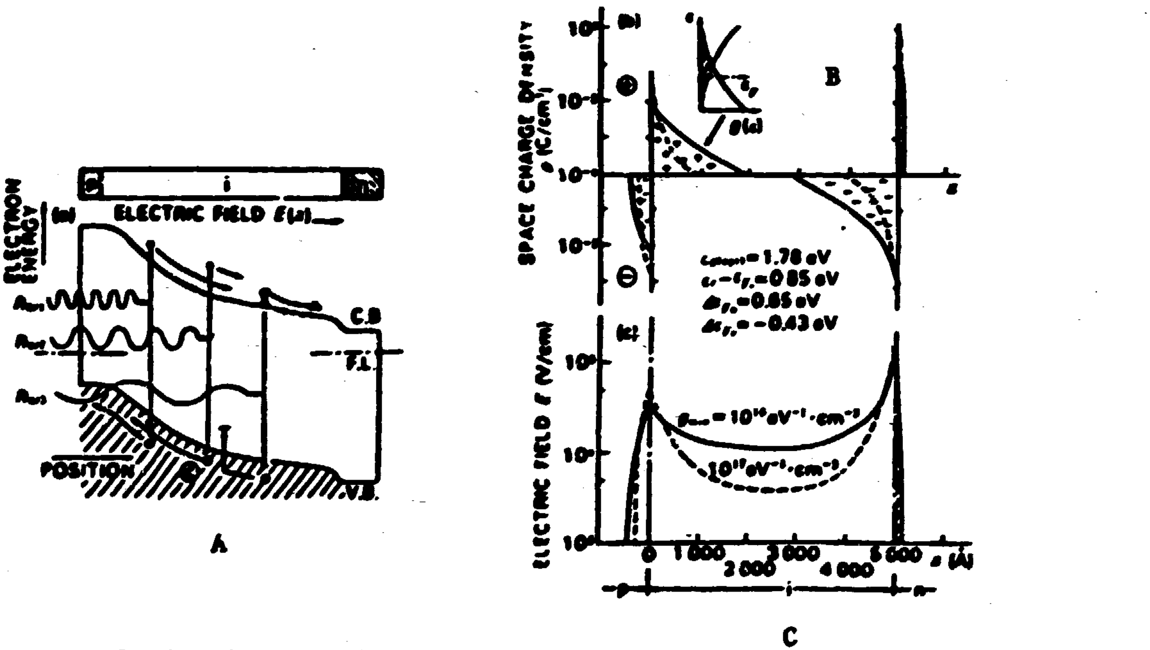

Figure 53: Band model of a highly efficient thin-film pin amorphous Si solar cell (A) with space charge (B) and field distribution (C).

4.2.1 α-Si Solar Cell Operation, Losses and Degradation. The higher efficient α-Si cells are pin-cells which have an extended i-region interfacing the pn-junction. Most of the light is absorbed within the i-region (Fig. 53). The conversion efficiency of such cells exceeded 10% in 1982 (Catalano et al.[48]) and presently lies in the 11–12% range for a pin-α SiC/α Si heterojunction cell of 1 cm^2 area[49] (the α-SiC also acts as window).[50] More recently ECD achieved 13% efficiency at a triple layer cell (see below).

The low carrier mobility ($\mu_n < 1cm^2/Vs$, $\mu_p < 10^{-2}cm^2/Vs$) requires drift-field assistance to collect most of the minority carriers which are generated in the device of a thickness of 0.5 μm, since typical lifetimes are $< 10^{-7}$s for electrons and $< 10^{-5}$s for holes, indicating a diffusion length of substantially less than the width of the i-part of the cell ($5 \cdot 10^{-5}$cm). With $F \simeq 10^4$ V/cm in a higher compensated i-region one estimates a Schubweg for electrons,

$$L_s = \mu_n F \tau_n, \tag{36}$$

which exceeds 10^{-4} cm for $\tau_n > 10^{-8}$ s, and therefore provides a means for such carrier collection (see Sec. 3.2.3).

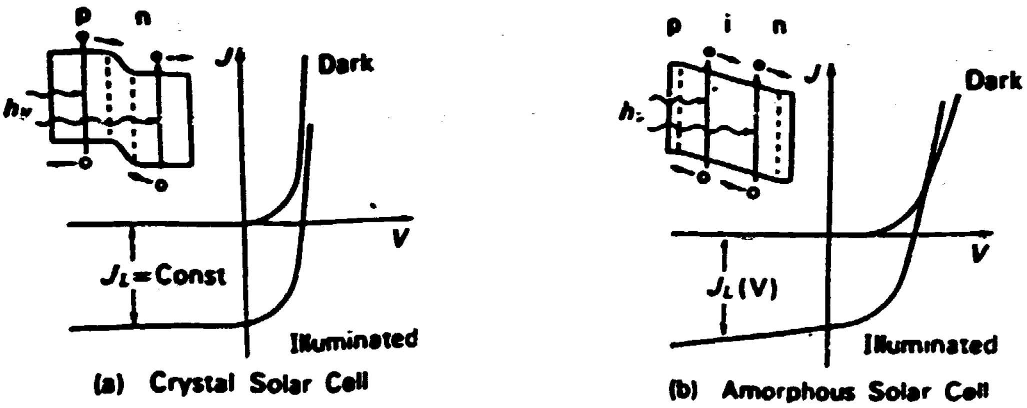

Figure 54: Current-voltage characteristics for a crystalline (A) and amorphous (B) Si solar cell.

The penalty for such drift-field is a sloping current-voltage characteristic with reduced fill factor (Fig. 54). The observed highest values of $V_{oc} \simeq 0.81$ V, $j_{sc} =$ 19 mA/cm^2, and $FF \simeq 0.7$ are respectable in the light of this discussion. Typical material and deposition parameters of α-Si:H cells are listed in Fig. 55 (after Sabiski[51]). For major further improvements in cell-efficiency a redesign of the cell is indicated, as indicated below.

Presently two effects seem to counteract each other: increased compensation in the i-layer produces a higher field resulting in an enhanced collection efficiency, but probably reduces the minority carrier lifetime due to enhanced recombination by donor acceptor pairs (compensation effect). An increase in minority carrier lifetime, however,

Deposition Gas	100% SiH_4 to 10% SiH_4 in H_2
Deposition Temp. (°C)	200 - 350
Pressure	5 - 250 m torr for 100% SiH_4 to 3 torr for diluted SiH_4
Flow Rate (SCCM)	30 - 200
Power Density (W/cm²)	0.02 - 2.0
Deposition Rate (Å s^{-1})	2.0 - 4.0
Hydrogen Content (At. %)	8 - 15
Optical Bandgap (eV)	1.65 - 1.80
Minimum Gap State Density $(eV)^{-1}$ cm^{-3}	~ 10^{16} (FE) ~ 10^{16} (CV) ~ 10^{16} (DLTS)
ESR (Spins/cm³) undoped	< 10^{16}
Dark Conductivity (Ω^{-1} cm^{-1})	10^{-9} - 10^{-10}
Activation Energy (eV)	~ 0.7
Photoconductivity (Ω^{-1} cm^{-1})	10^{-4} - 10^{-5}
Drift Mobility (cm²/V sec)	$\mu_e \sim 1$: $\mu_H \sim 10^{-3}$ room temp.
Hole Diffusion Length (μm) at 100 mW/cm²	0.5 - 1.3 surface photovoltage
($\mu\tau$) (cm^2 V^{-1})	~ 10^{-7} for L ~ 0.5 μm
Absorption Coefficient (cm^{-1})	1.5 × 10^5 at 2.5 eV 7.0 × 10^4 at 2.25 eV 1 × 10^3 at 1.80 eV
Dark Conductivity (max) n-Layer (Ω^{-1} cm^{-1})	0.01 - 0.1 (amorphous) 1 - 20 (microcrystalline)
Activation Energy n-Layer (eV)	~ 0.2 (amorphous)
Dark Conductivity (max.) p-Layer (Ω^{-1} cm^{-1})	0.001 - 0.01 (amorphous) 1 - 20 (microcrystalline)
Activation Energy p-Layer (eV)	~ 0.5

Figure 55: Typical material and deposition parameters.

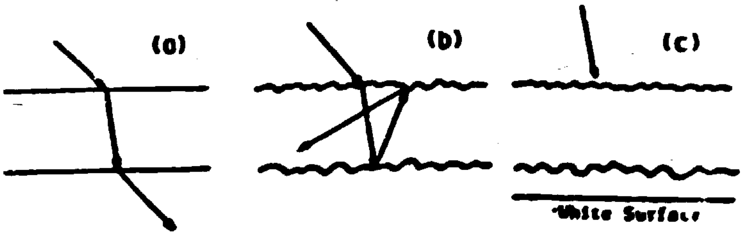

Figure 56: Light trapping by using rough surfaces and back surface reflection to increase the collection efficiency of a-Si cells.

Presently two effects seem to counteract each other: increased compensation in the i-layer produces a higher field resulting in an enhanced collection efficiency, but probably reduces the minority carrier lifetime due to enhanced recombination by donor acceptor pairs (compensation effect). An increase in minority carrier lifetime, however, by reduced compensation causes an increased recombination at the back surface due to communication through the ip-junction (see Sec. 3.2).

One could therefore, expect an increase in efficiency when the back electrode is covered by an isolating film, except for a dot matrix providing sufficient contact area. A redesign to avoid series resistance limitation and field losses in the i-layer between the dot contacts is required to achieve improved efficiencies.

Stacked cells are also collecting more efficiently[52] low energy photons (< 1.8 eV) for which the optical absorption depth is larger than the active cell thickness. Light trapping is another way to increase the collection efficiency of long wave length light[53] (as indicated in Fig. 56).

The *cell degradation* is a factor of major concern. As shown by Stabler and Wronski[54], the decrease in cell efficiency in time is a function of treatment and doping and can be reduced substantially. Its sensitivity to oxygen (possibly nitrogen)[55] to enhance and boron to decrease degradation[56,57] was already indicated in 1982 (see Fig. 57).

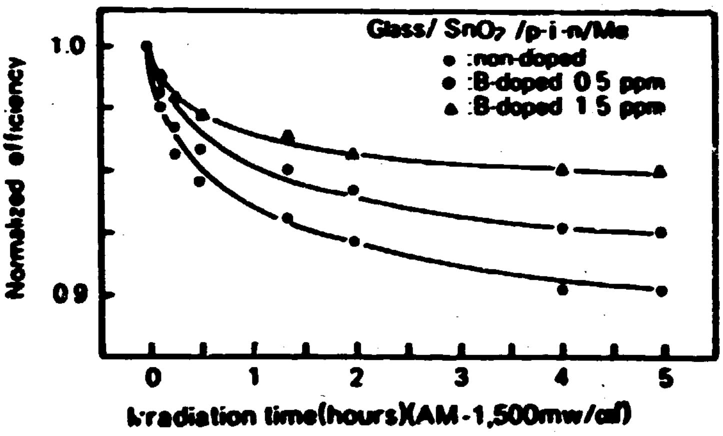

Figure 57: *Accelerated efficiency degradation of a pin-α-Si solar cell with optical irradiation of AM1 spectrum, but 500 mW/cm², normalized.*

The degradation is probably based on several mechanisms, the most important of which may be described as photochemical reactions. These reactions are thermally activated, need light to become active, and anneal out in the dark (accelerated at elevated temperatures). Hence, continuous illumination at elevated temperatures and light intensities produces accelerated degradation* and permits a compressed timescale research of the degradation mechanisms. The application of an appropriate time expansion factor permits some estimate of projected field life.

Present microscopic models of the degradation process include dangling bond rearrangement after recharging their electronic states under light (Adler[58]). These photochemical reactions consequently convert donors and acceptors† into recombination centers, thereby reducing carrier (and minority carrier) lifetimes, hence decreasing photoconductivity, and, when extensive enough, the collection efficiency. This causes first a reduction in the fillfactor, since near V_{oc} the i-layer field is not strong enough to produce a sufficient Schubweg. With increased reverse bias, again, even with somewhat reduced minority carrier life, most of the photogenerated excess carriers can be extracted; hence the saturation current is only slightly reduced.

With an intentionally reduced spreading of the quasi-Fermi levels, a less severe redistribution of carriers occurs; therefore photochemical reactions are reduced and degradation is less severe. This seems to be one of the reasons that present commercial cells (used as power source for calculators, watches, etc.) have satisfactory life when exposed intermittantly and only rarely to intense sunlight.

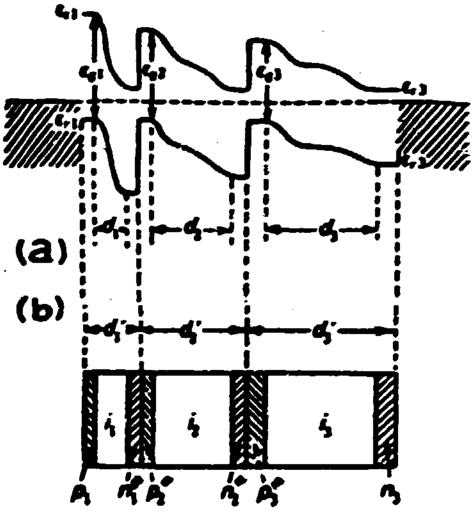

Figure 58: Stacked a-Si solar cell with varying band gap (largest towards the light) achieved by alloying Si with C or Ge; n^+p^+ tunneling interconnects the stacked cells.

---

* But not necessarily larger degradation since the annealing is also enhanced at elevated temperatures.

† One therefore also observes a reduction in the dark conductivity.

Another promising way to reduce the spread of quasi-Fermi levels in each individual cell is the use of stacked cells (Dalal[60]) (Fig. 58). Indeed, excellent improvements of life expectancies have been reported in such multi-gap cells[60,61]. A large body of research papers appear in the recent proceedings of the IEEE Photovoltaic Specialist Conference[62–71], which indicates in addition to a sensitivity to doping, temperature and light level also a sensitivity to material i-layer thickness, as can be expected from the change in defect structure during these photochemical reactions, hence inducing changes in the space charge density, causing in turn changes in the built-in-fields and therefore in the cell performance for insufficiently compensated wider cells (see Sec. 3.2.4, Fig. 24).

The recent progress in the development of stacked, multi-gap cells has sparked renewed optimism for the α-Si solar cell with feasibilities to reach efficiencies in excess of 15% and life expectancies in excess of 10 years in field deployment[72].

Government sponsored fundamental research activities for further development of the α-Si solar cell and the involved research teams in the USA are listed in Table 8. Specific industrial involvement in this field with government support is listed in Table 9 (prepared by Sabisky et al. recently[73]).

Table 8: Amorphous Si Research Effort Sponsored
by the US Government.

Fundamental Research Activities and Research Teams

Light-Induced Effects

Xerox Palo Alto Research Center
Optical and electronic properties of a-Si alloy material

University of Oregon
DLTS measurements

Massachusetts Institute of Technology
Theory of light-induced defects

Solar Energy Research Institute
Stability studies of a-Si:H material and devices

Alloy Materials

Harvard University
Fluorinated a-Si,Ge:H alloys

North Carolina State University
a-Si,Ge:H using dual magnetron sources, local bonding theory

Solar Energy Research Institute
a-Si, Ge:H prepared by glow discharge

Alternate Deposition Methods

Chronar
Photo-CVD a-Si:H using Hg sensitized disilane

University of Delaware
Photo-CVD a-Si:H and a-Si,Ge:H (New Ideas) using Hg sensitized disilane

Harvard University
APCVD of SnO$_2$(F), a-Si:H, and diffusion barriers

Massachusetts Institute of Technology (New Ideas)
Laser-induced CVD of silane using CO$_2$ laser

Device Modeling, Testing, Reliability

Solar Energy Research Institute
Measurement standardization, Extended outdoor testing, Resource assessment

Jet Propulsion Laboratory
Reliability studies

University of Florida
a-Si:H device modeling

Plasma and Material Characterization

Naval Research Laboratory
ESR and NMR studies

National Bureau of Standards
Characterization of glow discharge plasmas

North Carolina A&T
Thermal and optical effects in a-Si:H

Rockwell International Science Center
EPS of a-Si:H materials and devices

University of Utah (University Program)
ESR, NMR, and spectroscopic investigations

Material Deposition Rate

Brookhaven National Laboratory
Material studies, disilane glow discharge

Vactronic
Glow discharge material using disilane

Table 9: Amorphous Si Partnerships With
US Government Support.

Government-Industry Partnerships
Multiyear, Multidisciplinary Subcontracts

Chronar

- Single junction p-i-n cells
- RF glow discharge,
  two electrodes
- Three chambers
- Glass substrate

3M

- Single junction p-i-n cells
- RF glow discharge,
  two electrodes
- Three chambers
- Flexible polymer substrate

Solarex

- Single junction p-i-n cells
- DC glow discharge,
  three electrodes
- Three chambers
- Glass substrate

Spire

- Multi-junction cells,
  a-Si alloy cells
- RF glow discharge,
  three electrodes
- Six chambers
- Glass substrate

4.2.2 Production of α-Si Cells, Economical Aspects.

The production of the α-Si cell as a thin-film cell is rather insensitive to the substrate structure and can be fully automated. A typical cell cross-section of such cell is shown schematically in Fig. 59.

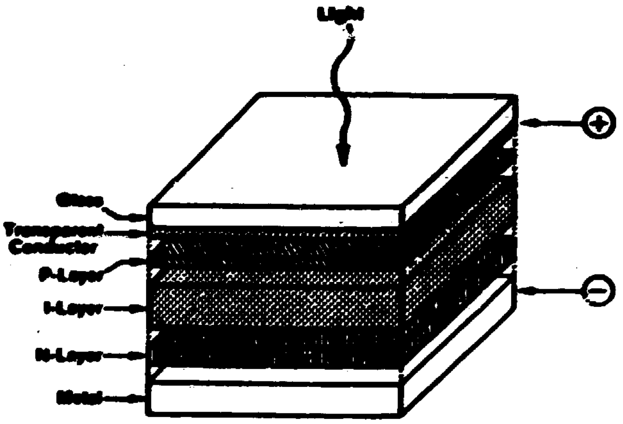

Figure 59: Cross-section through a typical α-Si solar cell.

A schematic of a production line is shown in Fig. 60, and for a partial view of an actual line in Fig. 61. Using a variety of substrates, from stainless steel to polymide films[51] to hybridization on already formed units such as roof shingles (Fig. 62), has the potential to reduce the balance of system cost to highly attractive levels.

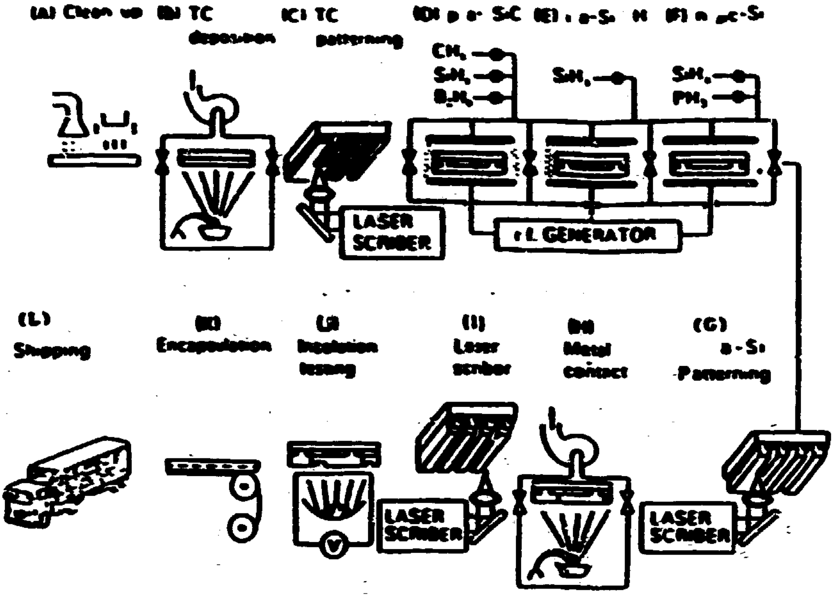

Figure 60: Schematic of a production line for automatic production of α-Si solar cells.

Figure 61: Actual production line segments of a roll to roll fabrication at Sovonics.

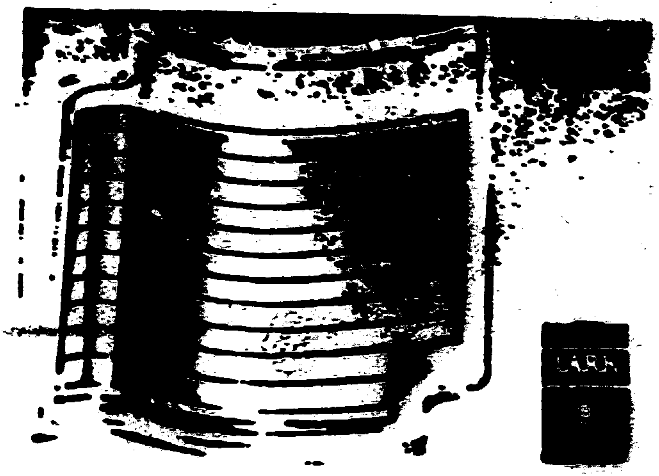

Figure 62: Solar shingle with α-Si cells.

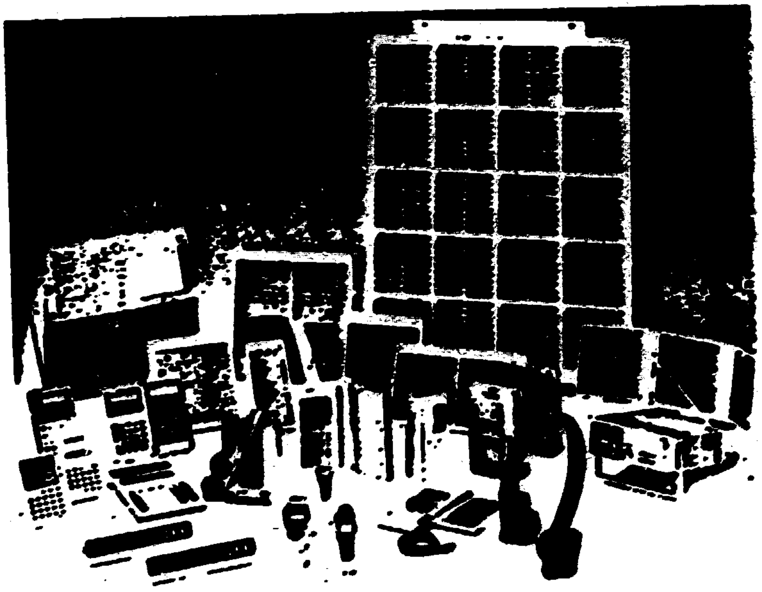

Figure 63: Variety of consumer applications using amorphous Si solar cells (Sanyo Electric Co. Ltd.).

Present operation of production lines in several companies has entered a learning curve which promises a high probability for full-scale commercialization after freezing of an attractive long-life-expectancy cell design with a reasonable efficiency (~10%).

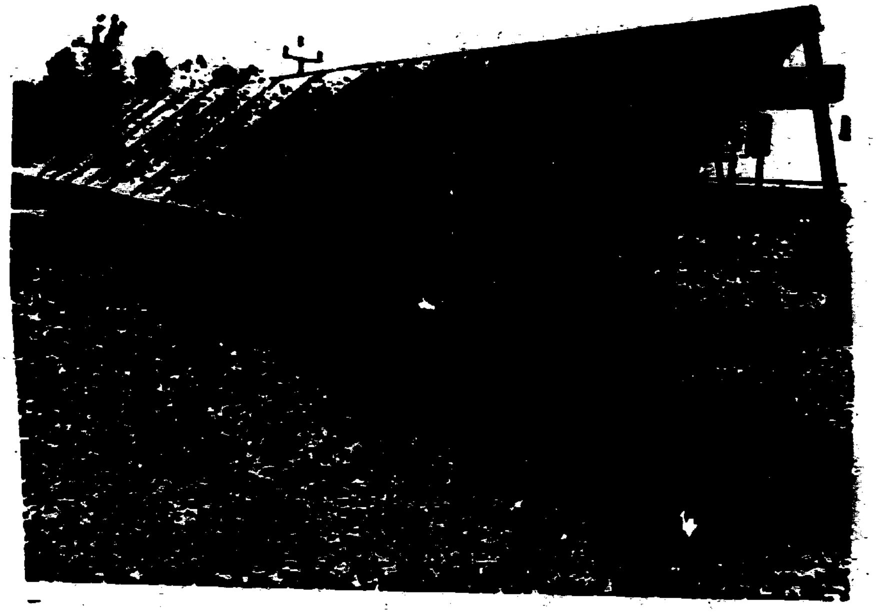

Figure 64: Amorphous Si panels for commercial applications. (Sovonics)

It is therefore expected that the α-Si cell production line will swiftly expand from the present consumer application market (Fig. 63) to the larger scale solar market (Fig. 64) which is presently dominated by the crystalline Si solar panels.

It is also expected that the production cost of these solar cells can be reduced to below 0.5 $/W (1985 dollars).

4.3 Other Promising Solar Cells.

Some of the inherent limitation in the present generation of crystalline and amorphous Si cells justifies vigorous further development of alternative materials. These limitations relate to

- a too-low band gap in Si, limiting its maximum efficiency,
- the indirect gap optical absorption, requiring a rather thick crystal sheet of Si,
- the low mobility of both carriers in α-Si, and
- photochemical reactions at room temperature in α-Si.

Other materials, such as GaAs and CdTe, have advantages in respect to the above listed limitations, suggesting the potential of higher efficiencies and extended life expectancy for homojunction solar cells made from these semiconductors. However, both compounds contain elements of very limited supply (Ga and Te).

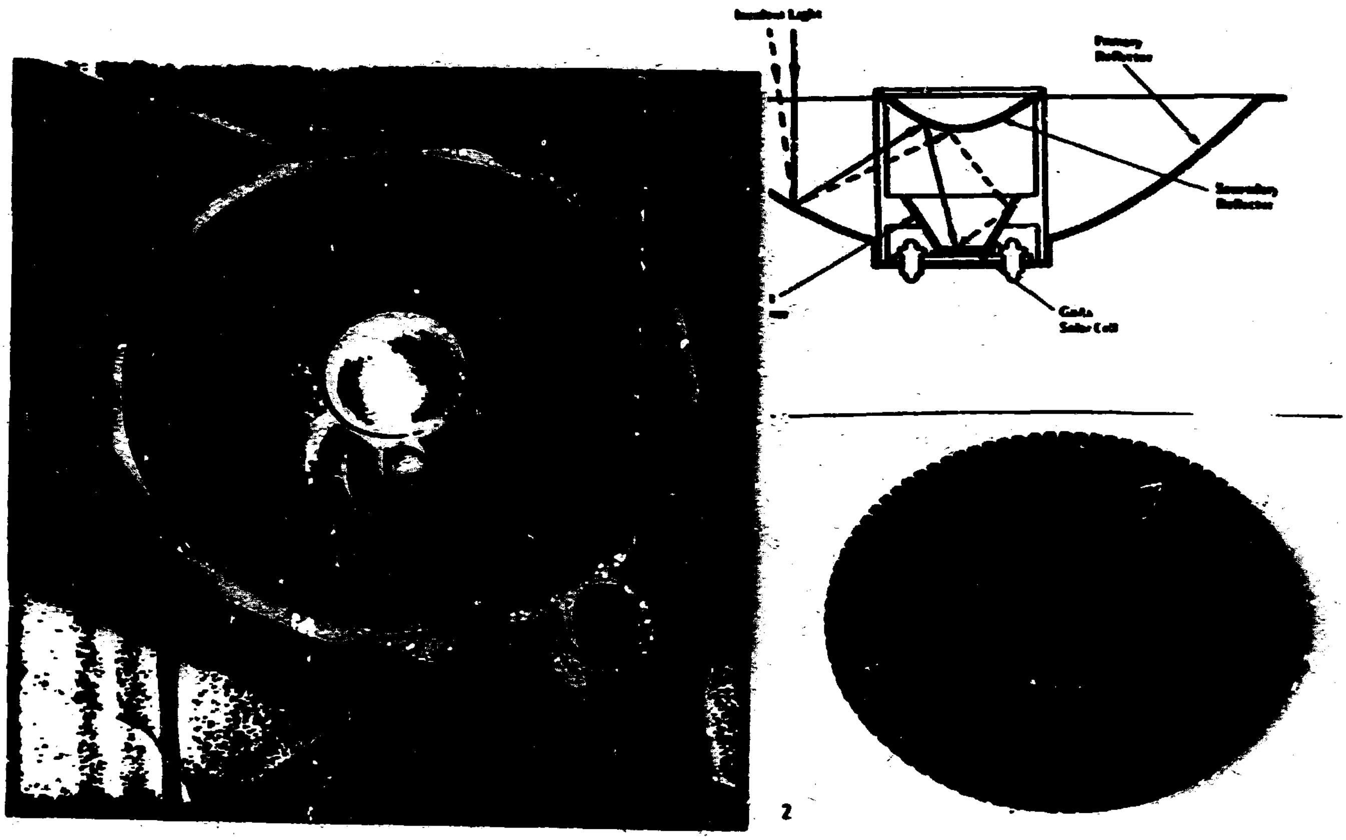

Figure 65: Varian 1000× concentration module with GaAs cell.

The present development of GaAs is justified since it can be operated at higher temperatures and high light intensities making the cell attractive as a receiver in concentrators with concentration ratios up to 1000 (Varian) — see Fig. 65. Presently best GaAs cells achieve a conversion efficiency of 23.7% at 209 suns[74] and of 26% at 753 suns[75]. A cost comparison[76] shows that such GaAs cells with an efficiency of 25% can cost between \$3.50 and \$10 per cm^2 to support an array cost of 1.30\$/W, while for the same array cost the price of Si concentrator cells of 20% efficiency must be reduced by a factor of 12 below the above-projected cost for GaAs. The present state of the art permits an installed array field subsystem cost near 7\$/W with approximately 17% of the subsystem cost allocated for the solar cell[76].

The highest presently achieved efficiency for a single Mg-doped AlGaAs/GaAs cell is reported by Hamaker et al.[77] at 26% in a concentator deployment.

The development of thin-film GaAs is another possibility if surface and grain boundary passivation can be achieved. A high recombination velocity at these surfaces is a major drawback of the GaAs. This is circumnavigated by using an $Al_xGa_{1-x}As$ window on top of highly efficient single crystal cells. A very interesting approach is the double heterostructure of two AlGaAs/GaAs cells on top of each other,[78] which achieved 23% efficiency at AM1 with $j_{sc} = 25.3$ mA/cm^2, $V_{oc} = 1.05$ V and a fillfactor of 87%.

Presently thin-film polycrystalline cells have a disappointingly low efficiency while thin film single crystal cells still require a GaAs substrate (epitaxy), yielding 20% efficient cells or, being thinned by etching, require a thickness of ~ 70 μm with efficiencies in the 16% range.

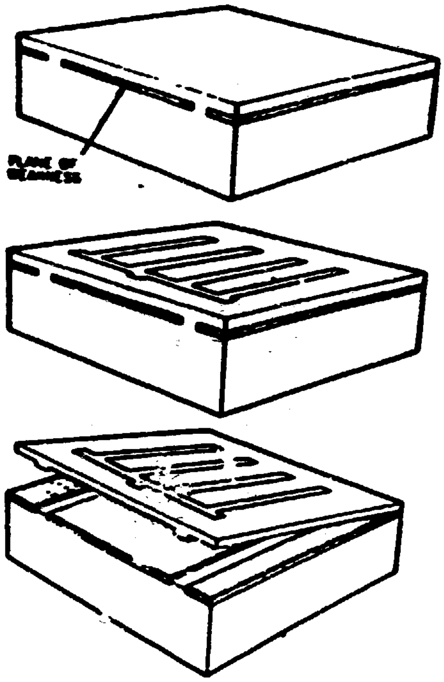

Figure 66: Schematic diagram of the CLEFT process illustrating the separation of the thin top cell from its reusable substrate after Fan et al.[79].

A potentially interesting approach is a process known as CLEFT (cleavage for lateral epitaxial film transfer). Here lateral growth on a properly oriented, mostly masked GaAs substrate can be used to form GaAs single crystal sheets which can easily be cleaved from the substrate (Fig. 66) after it is bonded to glass, and cells of 17% efficiency with only 5 μm thickness have been produced[79].

Recently studies begun of a $GaAs_{0.75}P_{0.25}$ solar cell, which could become an interesting partner in a stacked multijunction cell. The achieved[80] 15% efficiency is encouraging.

As a direct band-gap material with a high electron mobility, GaAs and some other III IV compound materials have sufficient potential to warrant further research and development (see the numerous papers in the Proceedings of the 18th IEEE Photovoltaic Specialist Conference).

The *CdTe solar cell* is another, potentially highly efficient cell which, as single crystal cell, has already shown in excess of 13% efficiency. The Kodak group has reported 10.9% efficiency for a polycrystalline thin-film CdS/CdTe device at AM2 while, for a slightly thicker, sintered CdS/CdTe heterojunction cell, the Matsushita group[81] reports an active area efficiency of 12.8%. (See also ref. 84). Problems with a rapid development of this cell relate to the difficulties to make a highly p-type material and to produce good ohmic contacts on the p-CdTe.

Another II VI solar cell is the $Hg_{1-x}Cd_xTe$ cell which has recently shown a promising 9% efficiency[83].

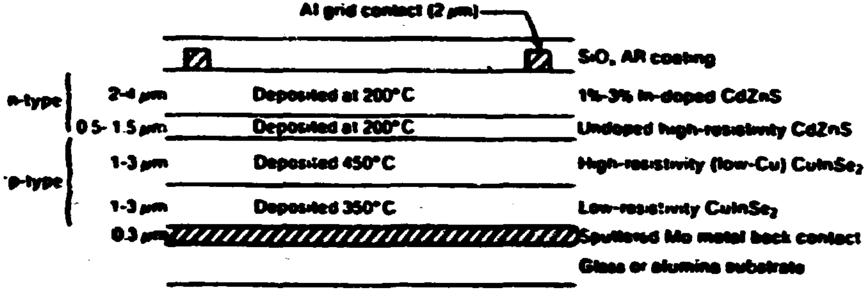

Figure 67: CdS/CuInSe$_2$ solar cell structure developed by Boeing.

Other possibilities include heterojunction cells, such as CdS/CuInSe$_2$. Such a cell was developed by Michelson et al. at Boeing Aerospace Co. and yielded 11% conversion efficiency. It is deposited by evaporation of the components in a multi-layer thin-film structure (Fig. 67).

This structure has the potential of obtaining cell efficiencies in excess of 15% and excellent long-term stability[83].

Other materials which have been studied to some extent in respect to their photovoltaic capabilities and have shown conversion efficiencies in excess of 1% include Zn_3P_2, Cu_2O, CdSiAs, CdSe several copper-ternaries and a number of heterojunctions, including CdS/Cu_2S and CdS/InP.

A list of US government sponsored research projects in the field of polycrystalline thin film solar cells given in Table 10 indicating a wide variety of activities[84].

By far the most attention received the CdS/Cu_2S heterojunction in the recent past. This for good reasons: the topotaxial growth of the Cu_2S into the surface layer of CdS provides the most intimate contact and guarantees a compatible crystallite structure. The field limitation in illuminated CdS due to field-quenching[85] prevents tunneling even for relative high density of impurities in CdS. The almost liquid Cu sublattice in Cu_2S permits annealing even in cold winter nights of defects in Cu_2S created by ion diffusion during illumination. Ample availability of raw materials and the ease of fabrication indicate feasibility for very low cost production. The possibility for passivation indicate feasibility to permit inexpensive encapsulation. Initial hesitation to restart further intensive research and development was overcome when cell degradation

Table 10:
Polycrystalline thin film research sponsored by the US government (after Zweibel et al.[84]).

Structure (substrate)	Deposition Method*	Best Reported Efficiency	Group	Comments
$Cd_{1-x}Zn_xS/CuInSe_2/Mo/(alumina)$	Open-boat evaporation	11.9% (12.5% active area)	Boeing	25°C, Xenon, 1 cm²
$CdS/CuInSe_2/Mo/(alumina)$	Open-boat evaporation	10.3%	SERI	SERI Standard
$CdS/CuInSe_2/Mo/(glass)$	Effusion cell evaporation	11.3%**	IEC	28°C, 87.5 mW/cm² ELH
$CdS/CuInSe_2/Mo/(glass)$	Reactive magnetron sputtering	4.1%**	Telic/ U. Illinois	28°C, 87.5 mW/cm² ELH
$ZnO/CdS/CuInSe_2/Mo/(glass)$	Electrodeposition (Cu,In)/H_2Se	(new)	ISET	
$CdS/CuInSe_2/W/(graphite)$	Solution (Cu,In)/selenization	(new)	Poly Solar	
$ITO/CuInSe_2/W$	Electrodeposition	(new)	Weizmann	
$CdS/CuGa_xIn_{1-x}Se_2/(glass)$	Open-boat evaporation	7.2%	Boeing	SERI Standard
$CdS/CuGaSe_2/(alumina)$	Open-boat evaporation	2.7%	SERI	25°C, ELH
$(glass)/SnO_2/CdS$ or $CdO/Cd_{1-x}Zn_xTe$	Close-spaced sublimation	8.2% **(CdTe)	SMU	SERI Standard
$(glass)/SnO_2/CdS$ or $CdO/Cd_{1-x}Zn_xTe$	Chemical vapor deposition (CVD)	(new)	SMU	
ITO or $CdS/Cd_{1-x}Zn_xTe/(W/graphite)$	CVD	8.2% (x = 0, CdTe)	SMU	25°C, ELH
$CdS/CdTe/(graphite)$	Hot wall vacuum evaporation	4.7%	Stanford	25°C, ELH
$ITO/CdS/Cd_{1-x}Hg_xTe/(glass)$	Effusion cell evaporation	6.4%**	IEC	28°C, 87.5 mW/cm² ELH
$(glass)/ITO/CdS/CdTe$	Effusion cell evaporation	(new)	IEC	

* For absorber only
** Active area. The others are total area

Note: All efficiencies are "reported" unless indicated as having been measured at SERI

could be controlled by avoiding copper phase segregation from the Cu_2S. This was achieved using a graphite interlayer, and by avoiding needle-like protrusions of Cu_2S (hence excessive fields) by a modification of the etching process of CdS before Cu_2S formation[86].

The reason for the most recent discontinuation of the CdS/Cu_2S cell development (SES, Inc. in 1982) was the relatively high interface recombination which seems to prevent conversion efficiencies much in excess of 10%.

It is, however, not impossible by a redesign of this cell to reduce the interface recombination and consequently arrive at a potentially very attractive thin-film solar cell.

Finally, the trend to develop higher efficient cells has sparked several research efforts to *stack cells of different band gaps* on top of each other with the goal to approach 30% conversion efficiencies. Even though the net benefit from the added cell is expected to be of the order of only 10% or less, savings in the deployment structure could make the effort cost-effective. Careful matching of currents and of certain intrinsic cell parameters, such as the lattice constant (Fig. 68) and the electron affinity limit a *two terminal device* in material selection. *Four terminal devices* are more flexible in design and may be more promising to surpass single cell efficiencies, however, have other problems in array interconnection.

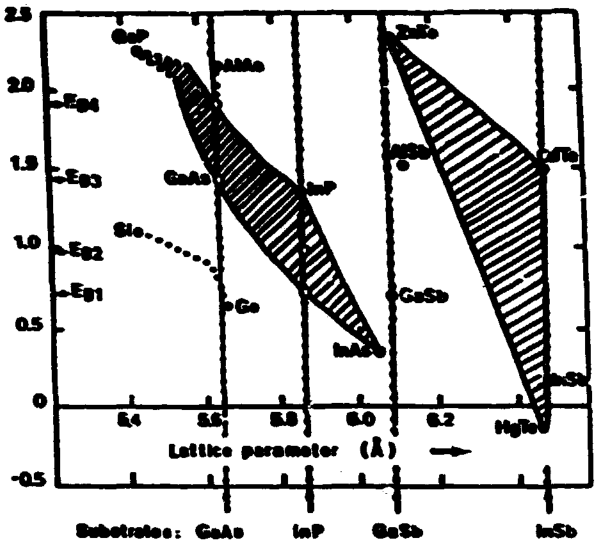

Figure 68: Band gap vs. lattice constant for numerous III V and II VI compounds indicating reasonable match for four groups of materials. Solid solutions of one of the components offers an intermediate band gap. Desirable band gap combinations are shown as $Eg_1 \ldots Eg_4$.

Stacking of AlGaAs/GaAs on top of Si has resulted in 22% conversion efficiency. The progress is slow as the combination of two cells poses many technology problems due to interrelation of treatments[87]. The most promising multijunction solar cell combinations are listed in Table 11.

Table 11:

Most Promising Multi-Junction Thin Film PV Technologies

To Cell (bandgap in eV)	Bottom Cell (bandgap in eV)	Lab. Record	Near-Term using Current Avail. Tech.	Practical Potential	Companies and Labs Pursuing	Comments
Amorphous Silicon (1.75)	$CuInSe_2$ (1.0)	13.1%	16.5%	20-25%	Arco Solar	Probably largest research effort
CdTe (1.5)	$CuInSe_2$ (1.0)	12.8%	16%	20-25%	Matsushita SERI Program IEC	Alloys of CdTe with higher bandgap being pursued
GaAs CLEFT[1] (1.4)	$CuInSe_2$ (1.0)	N.A.	23.4%	25-30%	Boeing	Greatest potential of current technologies
Amorphous Silicon (1.75)	Amorphous Silicon-Ge (approx. 1.5)	13%	16%	18-20%	ECD Other	Triple-junction all-cells also being studied

1. In the experimental CLEFT process, GaAs cells are produced on a single crystal then cleaved off.
Sources: Information on this table was obtained primarily from Ken Zweibel and Edward Sibiski at SERI.

4.4 Commercial Markets of Solar Panels.

As the first introduced commercially available solar panels, the Si panels have become the panels with by far the largest share of present deployment. In the following section we will list a number of examples for such deployment.

A target scale for a break-even cost of different photovoltaic modules is given in Fig. 69 indicating different interim markets and final, very large scale applications. An instructive and typical entry scenario is shown in Fig. 70 for a sizable interim market for solar panels replacing diesel driven generators. It indicates a cross-over in the 5 to 11 $/Watt range dependent on installation and fuel cost and shows an attractive market potential for present-day technology.

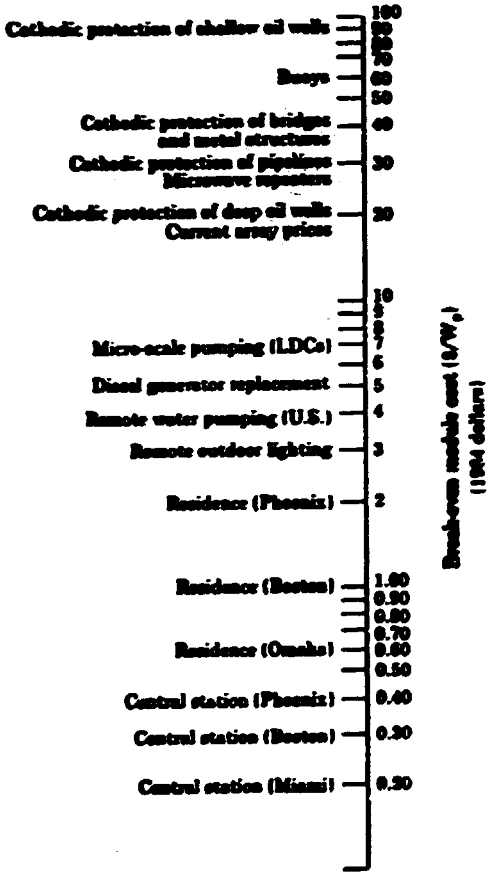

Figure 69: Break-even costs for various photovoltaic applications[41].

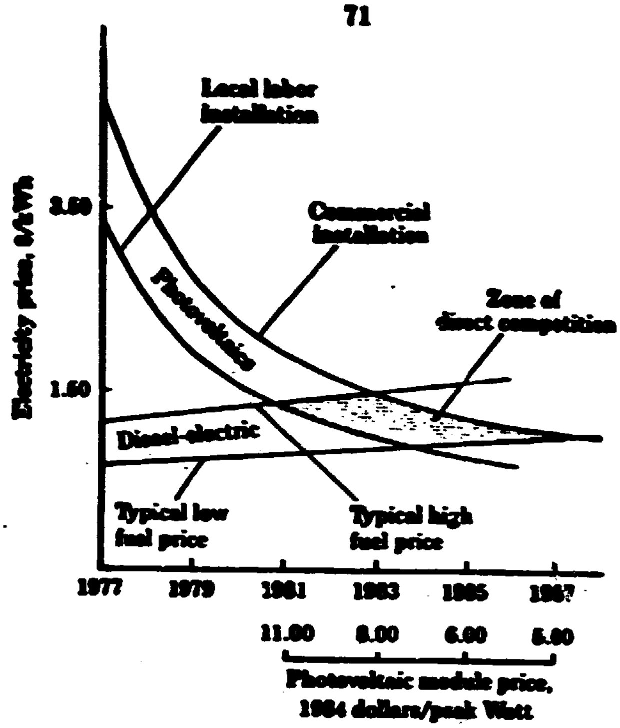

Figure 70: Energy price comparison[41] between 1 kW photovoltaic continuous power system and diesel driven generators reflecting fuel prices of ¢60/gal and $1.50/gal (lower and upper curve).

The market developed rapidly from only a few kW deployed in 1974 to shipments of more than 25MW in 1984 with the following distributions:

Remote Deployment	8MW
Consumer Products	7MW
Utility Grid Power	5MW
Off-Grid Power	3MW
Government Use	2MW

Presently a total in excess of 100MW of Si-Solar cell panels are installed, providing ample experience of marketability and performance and offering the basis for a broader public awareness.

A recent summary of the present photovoltaic technology and a breakdown of the 1985 production figures was assembled by Maycock and Strivewald (Table 12).

A list of the present active photovoltaic cell manufacturers is given in Table 13 (reprinted from Alternative Sources of Energy, May 1986, Vol. 81).

Other industrial firms and institutions actively involved in photovoltaic research, development or commercialization are listed[41] in Table 14.

Table 12: Present Photovoltaic Production Figures for the Different Si-technologies.

Current PV Technology Summary and 1985 Production Figures

Cell Type	Efficiency		Advantages	Disadvantages	1985 Production by Company (MWe)[1]			
	Lab. Record	Prod. Range						
Single Crystal Silicon	18.1%	10-13%	• Well established and tested technology • Stable • Relatively efficient	• Uses a lot of expensive material • Lots of waste in slicing wafers • Costly to manufacture • Round cells can't be spaced in modules efficiently	Arco Solar (US) Sharp (Japan) CEL (India) Hoxan (Japan) Solec Int'l (US) BP Solar (UK) Pragma (Italy) Ansaldo (Italy) Nippon Elec (Jap) Solarex (US)	4.7 .9 .6 .5 4 4 3 3 3 2	Helios (Italy) Hitachi (Jap) Mitsubishi (Jap) Kyocera (Jap) Heliodynamica (Braz) Bharat (India) Silonex (Canada) Siemens (Germany) Isophoton (Spain) Komatsu (Japan) Other Total	.2 .2 .2 2 2 2 1 1 1 1 4 10.85
Polycrystal Silicon	18%	10-12%	• Well established and tested technology • Stable • Relatively efficient • Less expensive than single crystal Si • Square cells for more efficient spacing	• Uses a lot of expensive material • Lots of waste in slicing wafers • Fairly costly to manufacture • Slightly less efficient than single crystal	Solarex (US) Photowatt (Fr) AEG (Germany) Solavolt (US) Kyocera (Jap) Pragma (Italy) Other Total	1.9 1.0 8 5 4 2 .1 4.9		
Ribbon Silicon	15%	10-12½%	• Does not require slicing • Less material waste than single crystal and polycrystal • Potential for high speed manufacturing • Relatively efficient	• has not been scaled up to large volume production • Complex manufacturing process	Mobile Solar (US) Westinghouse (US) Total	1 .05 15		
Amorphous Silicon	11½%	4-8%	• Very low material use • Potential for highly automated and very rapid production • Potential for very low cost	• Pronounced degradation in power output (Staebler Wronksy effect) • Low efficiency	Sanyo (Jap) Fuji (Jap) ECD/Sharp (Jap) Arco Solar (US) Chronar (US)	3.9 2.8 .5 2 2	Kaneka (Jap) Taiyo Yuden (Jap) Solarex (US) Sovonics (US) Other Total	.2 .15 .1 .1 .3 8.45

[1] Figures from PHOTOVOLTAIC NEWS February 1986 Vol 5, No 2 Edited by Paul D. Maycock and Edward N. Stewart

Table 18: Industry Worldwide Involved in Solar Cell Development and Commercialization.

AEG Corp.
Route 22
Sommerville, NJ 08876

AEG-Telefunken
A47, 2000 Wedel
Germany

ARCO Solar Inc.
9351 Deering Ave.
Chatsworth, CA 91311

Acurex Corporation
485 Clyde Ave
Mountain View, CA 94042

Alpha Solarco
1014 Vine St.
Suite 2530
Cincinnati, OH 45202

Applied Research Center
100, Dainichigashi-Machi
Moriguchi-shi, Osaka
Japan

Applied Solar
Energy Corp.
15251 E. Don Julian Rd.
City of Industry, CA 91790

BP Solar Systems
Aylesbury Vale
Industrial Park
Farmborough Close,
Stocklake
GB-Aylesbury,
Buckinghamshire
England

Boeing Aerospace Co.
P.O. Box 3999, M588-43
Seattle, WA 98124

Chronar Corp.
P.O. Box 177
Princeton, NJ 08540

Electrolab Inc.
2103 Mannix
San Antonio, TX 75222

Energy Conversion
Devices
1675 W. Maple Rd
Troy, MI 48084

Entech Inc.
1015 Royal Lane
P.O Box 612246
DFW Airport, TX 75261

E-Systems
P.O Box 226118
Dallas TX 75266

Free Energy Systems Inc
Mount & Red Hill Roads
P.O. Box 3030
Lenni, PA 19052

Fuji Electric Co., Ltd.
New Yurakucho Bldg.
12-1 Yurakucho 1-Chome,
Chiyoda-ku
Tokyo, 100 Japan

Heliodinamica S.A.
PO Box 8085
01051 Sao Paulo - S.A.
Brazil

Hoxan Corporation
2 Nishi 1-Chome,
Kita 3-jo
Chuo-ku, Sapporo 060
Japan

Intersol Power
Corporation
11901 W Cedar Ave
Lakewood, CO 80228

Isofoton S.A.
Oficinas Comme
Comandante Zorita 13
Madrid 20
Spain

J.W. Yerkes
Industrial Design
273 Thompson Ave
Chatsworth CA 91311

Kanegafuchi Chemical
Industry Co., Ltd.
2-80 Yoshidacho
1-Chome
Hyogo-ku, Kobe 652
Japan

Komatsu Electronic
Metals Co., Ltd. 2612
Shinomiya
Hiratsuka
Kanagawa
Japan

Kyocera
International Inc.
8611 Balboa Ave
San Diego, CA 92123

Kyocera Corporation
Chiba-Sakura Plant
Sakura Dai-3 Kogyo
Danchi
Osaku 1-Chome
Sakura-shi
Chiba-Pref. 285,
Japan

Martin Marietta Corp.
Solar Energy Systems
P.O Box 179,
M.S 60450
Denver, CO 80201

Matsushita Battery
Industrial Co., Ltd.
Solar Battery Plant
21, Matsushita-Cho
Moriguchi, Osaka 570
Japan

Mobil Solar
Energy Corp.
16 Hickory Dr.
Waltham, MA 02254

Mitsubishi Electric
Corporation
Itami Works
1-1, Tsukaguchi-Honmachi
8-Chome, Amagasaki,
Hyogo, 661
Japan

-Photowatt
International S.A.
131 Route De
l'Empereur
Rueil Malmaison
France

Photon Technology
Heideveld 1
B-1511 Huizingen
France

Polycrystalline
Silicon Technology Corp.
1819 S. Dobson Rd.,
Dobson Ranch
Mesa, AZ 85202

Pragma SpH
Via Marino Ghetaldi 64
I-00143 Rome
Italy

Sanyo Electric
Company Ltd.
Sumoto Manufacturing
Headquarters, Amorton Dept
222-1 Kaminaizen,
Sumotor-shi Hyogo
Japan

Sharp Corporation
Photovoltaics Division
282-1 Hajikami
Shinjyo-cho
Kitakatsuragi-gun
Nara 639-21 Japan

Showa Shell
Sekiyu, k.k.
7-3, 2 Chome, Maruno
Chiyoda-Ku, Tokyo
Japan

Siemens AG,
Postfach 103
D-8000, Munich 1,
West Germany

Silicon Sensors Inc.
Highway 18 East
Dodgeville, WI 53533

Silonex Inc.
331 Cornelia St
Plattsburgh, NY 12901

Solar Cells Ltd.
3327 D. Mainway
P.O. Box 1025
Burlington, Ontario
Canada, L7D 3S9

Solarex Corp.
1335 Piccard Dr.
Rockville, MD 20850

Solar Generators
Singapore Pty Ltd.
151 Lorong Chuan
Singapore, 1955

Solartherm Inc.
1315 Apple
Silver Spring MD. 20910

Solavolt
International
PO Box 2934
Phoenix, AZ 85062 -

SOLEC International
12533 Chadron Ave
Hawthorne, CA 90250

Solenergy Corp.
171 Merrimac St
Woburn, MA 01801

Sovonics Solar
Systems
6180 Cochran Rd.
PO Box 39608
Solon, Ohio 44139

Spectrolab Inc.
12500 Gladstone Ave
Sylmar, CA 91342

Springborn
Laboratories, Inc.
Enfield, CT 06082

SunWatt Corp.
P.O. Box 1396
Carbondale, CO 81623

Suntronic/Solar
Electronic
P.O. Box 60 53 44
D-2 Hamburg 60
West Germany

Tideland Energy
Pty. Ltd.
100 Old Pittwater Rd.
Brookvale, N.S.W 2100
Australia

Utility Power Group
9410 De Soto Ave.,
Unit G
Chatsworth, CA 91311

Varian Associates
611 Hansen Way K 219
Palo Alto, CA 94303

Westinghouse
Electric Corporation
Advanced Energy
Systems Division
P.O. Box 10864
Pittsburg, PA 15236

Zontec BV
Lage Dijk 26
NL-5700 AA Helmond
Belgium

Zymet Inc.
33 Cherry Hill Drive
Danvers, MA 01923

Table 14: Solar Industry Related to Photovoltaic Commercialization.

USA

AAI Corp.
PO Box 6767
Balitmore, MD   21204
(301) 628-3481

Abacus Controls, Inc.
PO Box 893
Somerville, NJ   08876
(201) 526-6010

AFG Industries, Inc.
PO Box 929
Kingston, TN   37662
(615) 245-0211

American Power Conversion Corp.
89 Cambridge St.
Burlington, MA   01803
(617) 273-1570

Arctic Cold
3 Old Windsor Rd.
Bloomfield, CT   06002
(203) 242-2211

Arthur D. Little
Acorn Park
Cambridge, MA   02140
(617) 864-5770

A. Y. McDonald
4800 Chavenelle Rd.
PO Box 508
Dubuque, IA   52001
(319) 583-7311, Ext 227

Balance of System Specialists (BOSS)
7745 E. Redfield Rd.
Scottsdale, AZ 85260
(602) 948-9809

Best Energy Systems
Route 1, PO Box 106
Necedah, WI   54646
(608) 565-7200

Braden Wire & Metal Products, Inc.
PO Box 5087
San Antonio, TX   78201
(512) 734-5189

C & D Batteries
3043 Walton Rd.
Plymouth Meeting, PA   19462
(215) 828-9000, Ext. 305

Crystal Systems, Inc.
35 Congress St.
Salem, MA   01970
(617) 745-0088

Delco Remy
2401 Columbus Ave.
Anderson, IN   46011
(317) 646-7404

Dynamote Corp.
1200 West Nickerson
Seattle, WA   98119
(206) 282-1000

Energy Materials Corp.
PO Box 353
Ayre Rd.
Harvard, MA   01051
(617) 456-8707

Exide Corp.
101 Gibraltar Rd.
Horsham, PA   19044
(215) 441-7480

Gates Energy Products
1050 S. Broadway
Denver, CO 80217
(303) 744-4806

General Electric
PO Box 8661, Rm 114
Philadelphia, PA 19101
(215) 962-5835

Globe-Union, Inc.
Battery Division
5757 North Green Bay Ave.
Milwaukee, WI 53201
(414) 228-2581

Heart Interface
1626 S. 341st Pl.
Federal Way, WA 98003
(206) 838-4295

Helionetics
Delta Electronic Control Div.
17312 Eastman St.
Irvine, CA 92714
(714) 546-4731

Hydrocap Corp.
975 N.W. 95th St.
PO Box 380698
Miami, FL 33138
(305) 696-2504

Iota Engineering, Inc.
4700 S. Park Ave.
Suite 8
Tucson, AZ 85714
(602) 294-3292

March Manufacturing
1819 Pickwick Ave.
Glenview, IL 60025
(312) 729-5300

Norcold, Inc.
1510 Michigan St.
Sidney, OH 45365
(513) 492-1111

Nova Electric Manufacturing Co.
263 Hillside Ave.
Nutley, NJ 07110
(201) 661-3434

Opto Technology, Inc.
Solar Systems, Inc.
1674 S. Wolf Rd.
Wheeling, IL 60090
(312) 537-4277

Parker McCrory
Parmak Division
2000 Forest St.
Kansas City, MO 64108
(816) 221-2000

Photovoltaic Energy Systems, Inc.
2401 Childs Lane
Alexandria, VA 22306
(703) 780-9236
(703) 780-9736

Polar Products
680 Stone Canyon Rd.
Lost Angeles, CA 90077
(213) 476-0082

Polaroid Corp.
730 Main St.
Cambridge, MA 02139
(617) 577-2255

Power Sonic Corp.
PO Box 5242
3100 Spring St.
Redwood City, CA 94063
(415) 364-5001

Pulstar Corp.
Baird Center
619-P S. Main St.
Gainsville, FL 32601
(904) 373-5707

Roger Ethier Assoc.
205 Franklin St.
Alexandria, VA 22314
(703) 683-2657

Silicon Materials, Inc.
999 E. Arques Ave.
Sunnyvale, CA 94086
(408) 737-7100

Silicon Sensors, Inc.
Highway 18 East
Dodgeville, WI 53533
(608) 935-2707

Solar Contractors & Builders, Inc.
8 Charles Plaza #805
Baltimore, MD 21201
(301) 727-6740

Solar Design Assoc.
PO Box 653
Lincoln, MA 01773
(617) 259-9426

Solar Usage Now, Inc.
Box 306
420 E. Tiffin St.
Bascm, OH 44809
(419) 937-2226

Solarwest Electric
232 Anacapa St.
Santa Barbara, CA 93101
(805) 963-9667

Solec International, Inc.
12533 Chadron St.
Hawthorne, CA 90250
(213) 970-0065

Solenergy Corp.
171 Merrimac St.
Woburn, MA 01801
(617) 938-0563

Sollos, Inc.
1519 Comstock Ave.
Los Angeles, CA 90024
(213) 820-5181

Specialty Concepts
9025 Eton Ave., Suite D
Canoga Park, CA 91304
(213) 998-5238

Spire Corp.
Patriots Park
Bedford, MA 01730
(617) 275-6000, Ext. 223

Surrette Storage Battery Co.
PO Box 3027
Salem, MA 01970
(617) 745-4444

Teledyne Inet
2750 W. Lomita Blvd.
Torrace, CA 90509
(213) 325-5040

3M Corp.
3M Center
St. Paul, MN 55144
(612) 733-1110

Tideland Signal Corp.
4310 Directors Row
Box 52430
Houston, TX 77052
(713) 681-6101

Topaz, Inc.
Powermark Division
9192 Topaz Way
San Diego, CA 92123
(619) 279-0831

TriSolar Corp.
10 DeAngelo Dr.
Bedford, MA 01730
(617) 275-1200

United Energy Corp.
420 Lincoln Center Dr.
Foster City, CA 94404
(415) 570-5011

William Lamb Co.
North Hollywood, CA 91601
(213) 980-6248

Wilmore Electronics Co.
PO Box 1329
Hillsborough, NC 27278
(919) 732-9351

Windworks
Box 44A, Route 3
Mukawongo, WI 53149
(414) 363-4088

Zomeworks
PO Box 712
Albuquerque, NM 87103
(505) 242-5354

JAPAN

Electro Technical Laboratories
1-1-4, Umerzono, Sakura-mura,
Shinji-gun
Ibaraki-ken, Japan

Hitachi Ltd.
Nippon Building
No. 6-2,2-Chome, Ohtemachi
Chiyoda-ku,
Tokyo 100, Japan

New Energy Development Organization (NEDO)
Suhshine Building
3-1-1, Higashi Ikebukuro,
Toshima-ku
Tokyo, Japan

Nippon Electric Co. (NEC), Ltd.
1753, Shimonumabe,
Nakahara-ku
Kawasaki-shi
Kanagawa 211, Japan

Institute of Space and
Astronautical Science
6-1, Komaba, 4-Chome, Meguro-ku
Tokyo 153, Japan

Japan Solar Energy Company, Ltd.
11-17 Koga-honmachi
Fushimi-ku
Kyoto 612, Japan

Kyoto Ceramic Co., Ltd. (Kyocera)
52-11 Inoue-cho, Higashino
Yamashina-ku
Kyoto 607, Japan

Ministry of International Trade
and Industry (MITI)
Sunshine Project Headquarters
1-3-1 Kasumigaseki, Chiyoda-ku
Tokyo 100, Japan

Osaka University
Machikaneyama, Toyonaka-shi
Osaka, Japan
Dr. Yoshihiro Hamakawa, Electrical Eng. Dept.

Toshiba Corporation
1 Komukai, Toshiba-cho
Saiwai-Ku
Kawasaki 210, Japan

Tokyo Denki Co., Ltd.
1-14-10, Uchikanda, Chiyoda-ku
Tokyo 101, Japan

Tokyo Institute of Technology
12-1, 2-Chome, Ohkayama
Meguro-ku
Tokyo 152, Japan

In Europe the following firms are involved in photovoltaics:

Country	*Company*	*Technology Activity*	*Affiliation*
Belgium	Belgosolar (90% government owned)	Cells/Modules	—
	E.N.E. Energie Nouvelle et Environnement	Cells/Modules	Solarex
England (UK)	Lucas—BP Solar System	Modules/Systems	—
	Solapax	Systems (Import modules from U.S.)	Solarex
France	Societe Francaise de Photopiles	Modules	Photowatt
	Photon	Cells/Modules	Solarex
	Total Oil	Systems	Photon Power
Germany	Wacker Chemitronics	Polycrystalline silicon refining	No
	AEG Telefunken	Modules	No
	Siemens	Modules	No
Italy	Ansaldo (100% government owned)	Cells/Modules	—
	ENI (75% government owned)		
	a) Solaris	a) Solar Grade Silicon Arc Furnace b) Ingot Casting SEMIX c) Cells/Modules d) Systems	Solarex
	b) Pragma	Solar Grade Silicon	Solarex
	ENEA (government agency)	Research & Experimental Systems	—
	Adriatica Componenti Electtronici	a) Modules b) Solar Grade Silicon	Siemens
Netherlands	Holec Solar Energy	System	Solarex
Switzerland	—	Fully-Integrated PV Production Plant	ENI (Italy) Standard Oil (Solarex)
	Photonetics	Modules	Societe Roma d' Electrict Parsan, Inc

*Information based on testimony by Dr R. R. Ferber of JPL to U.S. House of Representatives Subcommittees on Science and Technology (June 1982)

5 Illustration of Typical Applications

The following examples may illustrate some typical applications for solar cells. Most economical today is the use in remote areas where previously batteries or diesel-powered generators were employed. Examples are shown in Figs. 71 – 83.

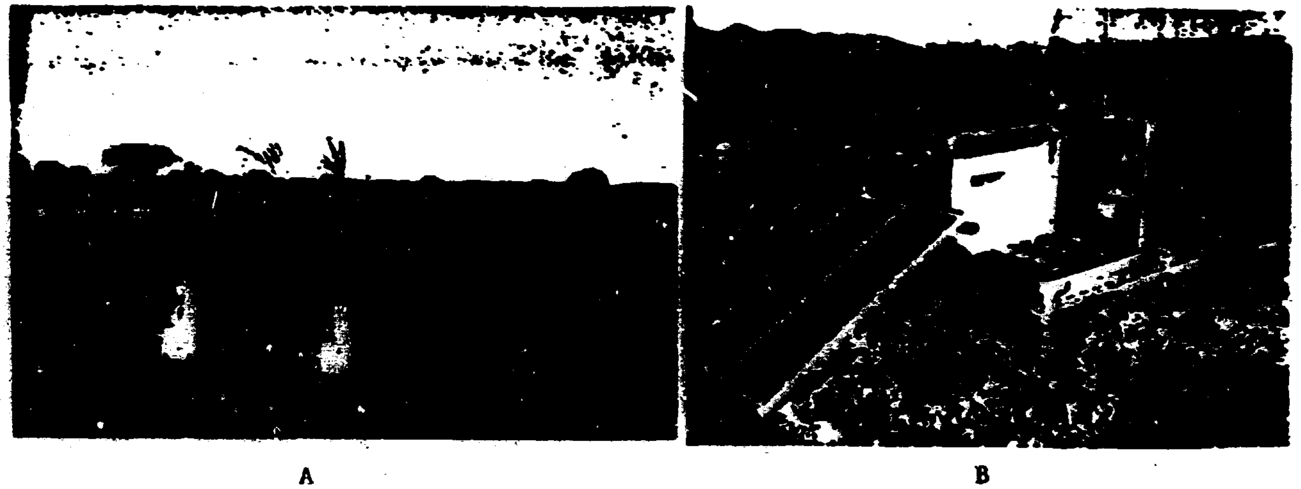

Figure 71: Agricultural irrigation, (Heliodynamica) (A) and rural telephone (B) (Solavolt International).

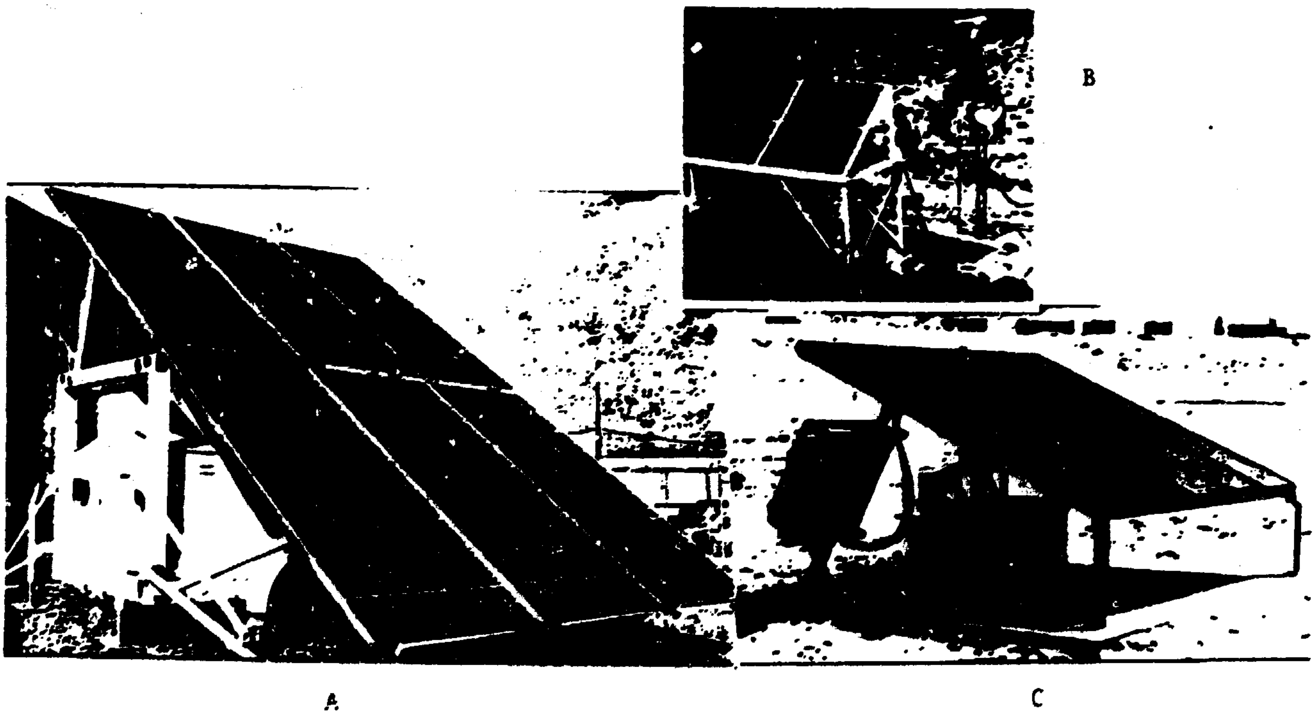

Figure 72: Military application (Integrated Power Co.) for microwave transmitters (Solarex) (A) and cathodic protection of oil or gas pipes (Mobil Solar) (B).

A

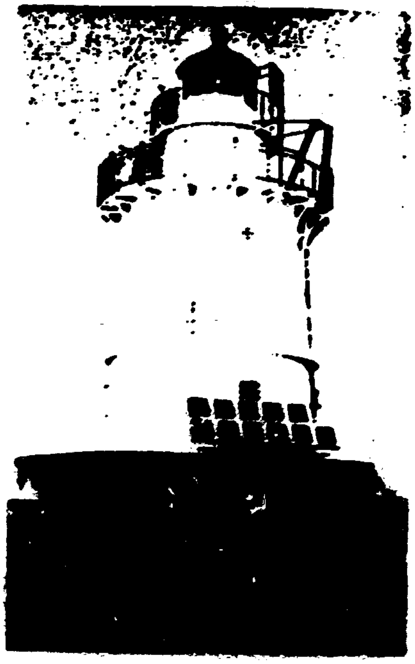

B

Figure 73: Remote power in alpine lodge (ARCO Solar) (A) and navigation light (Solarex) (B).

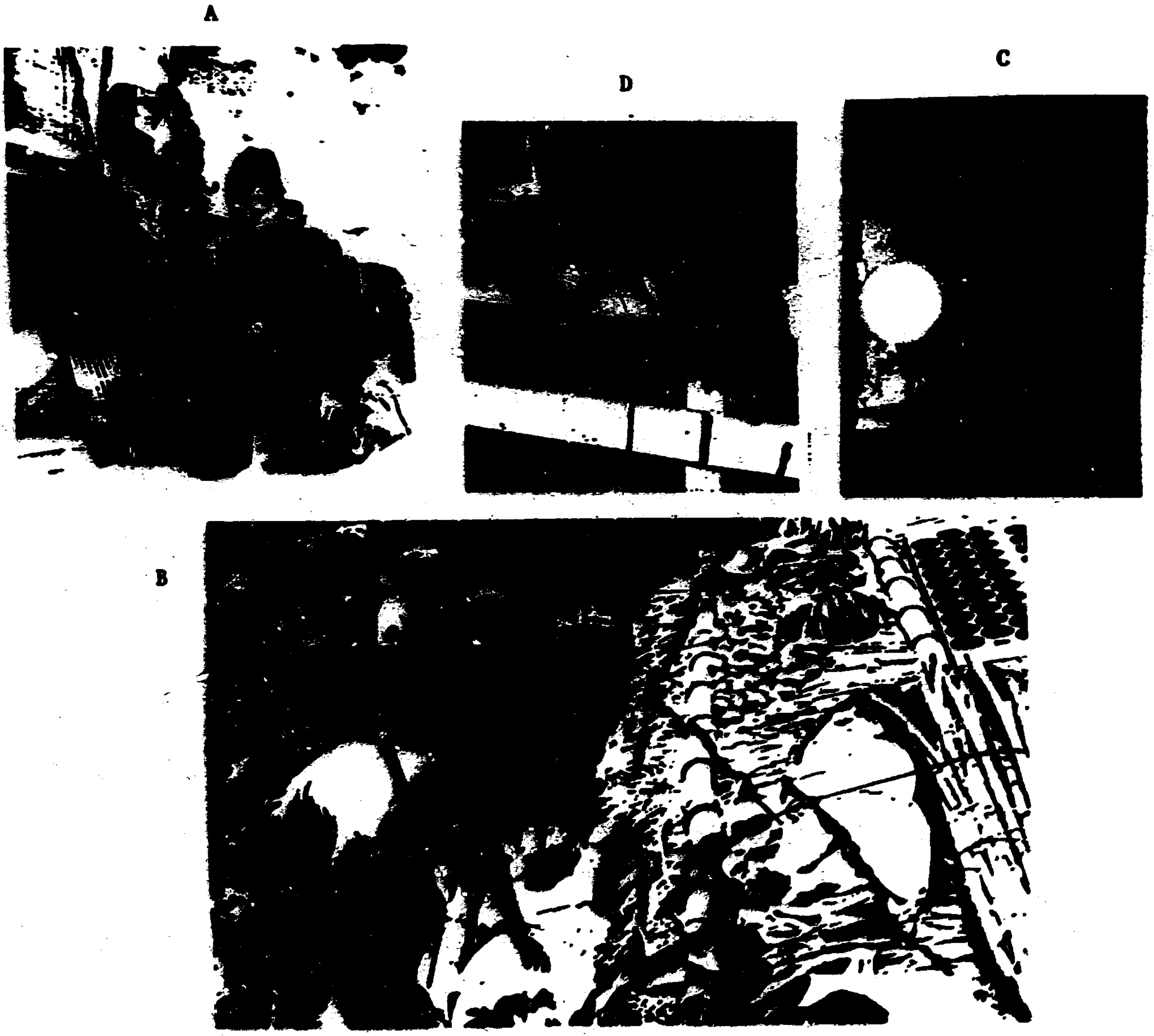

Figure 74: Remote communications (Sovonics (A) and Arco (B)); billboard lighting on freeways (Kyocera) (C), electric fence for farmers (Solarex) (D).

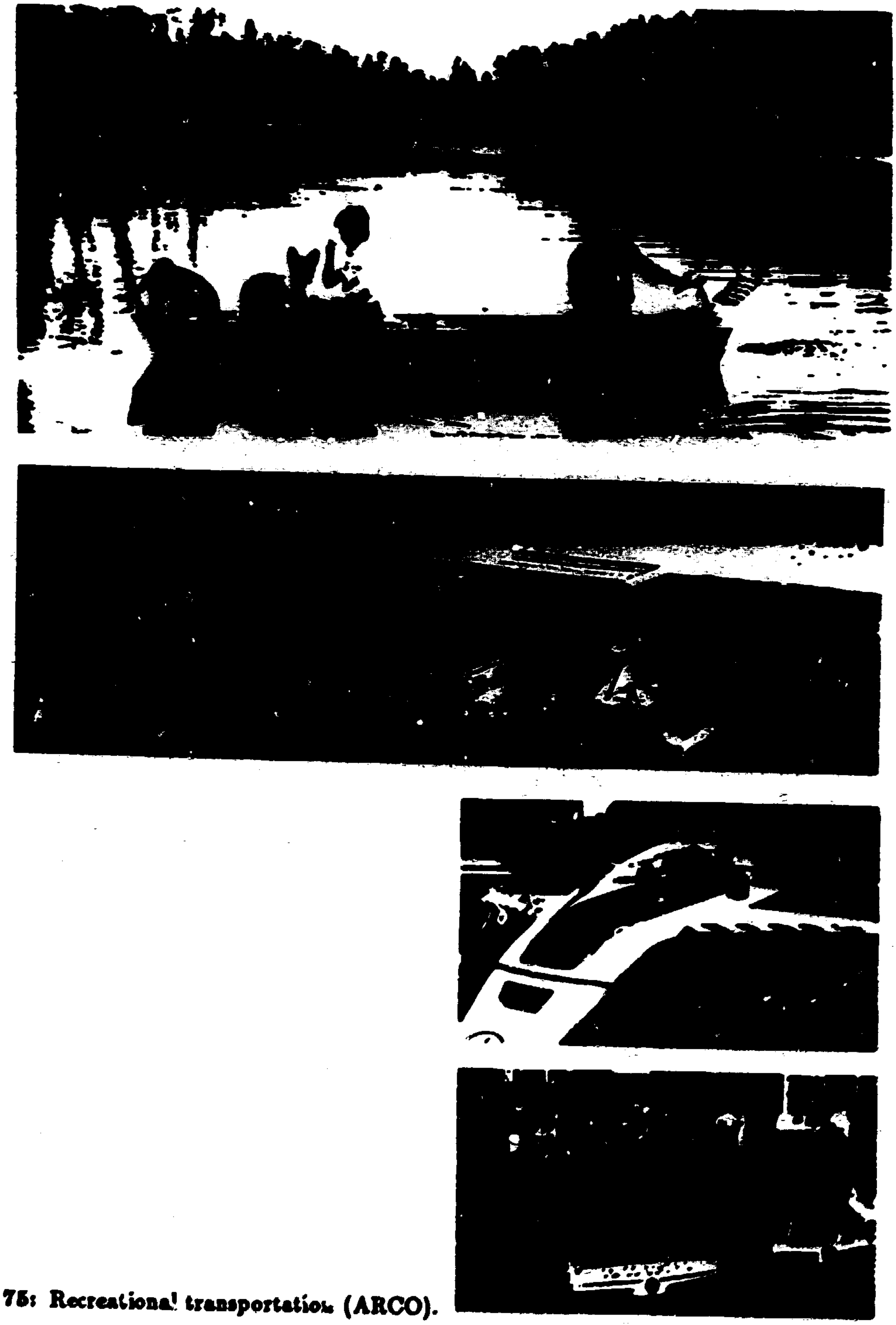

Figure 75: Recreational transportation (ARCO).

Figure 76: Remote use in small villages (Solarex) (A and B) and remote lighting (Mobile Solar) (C).

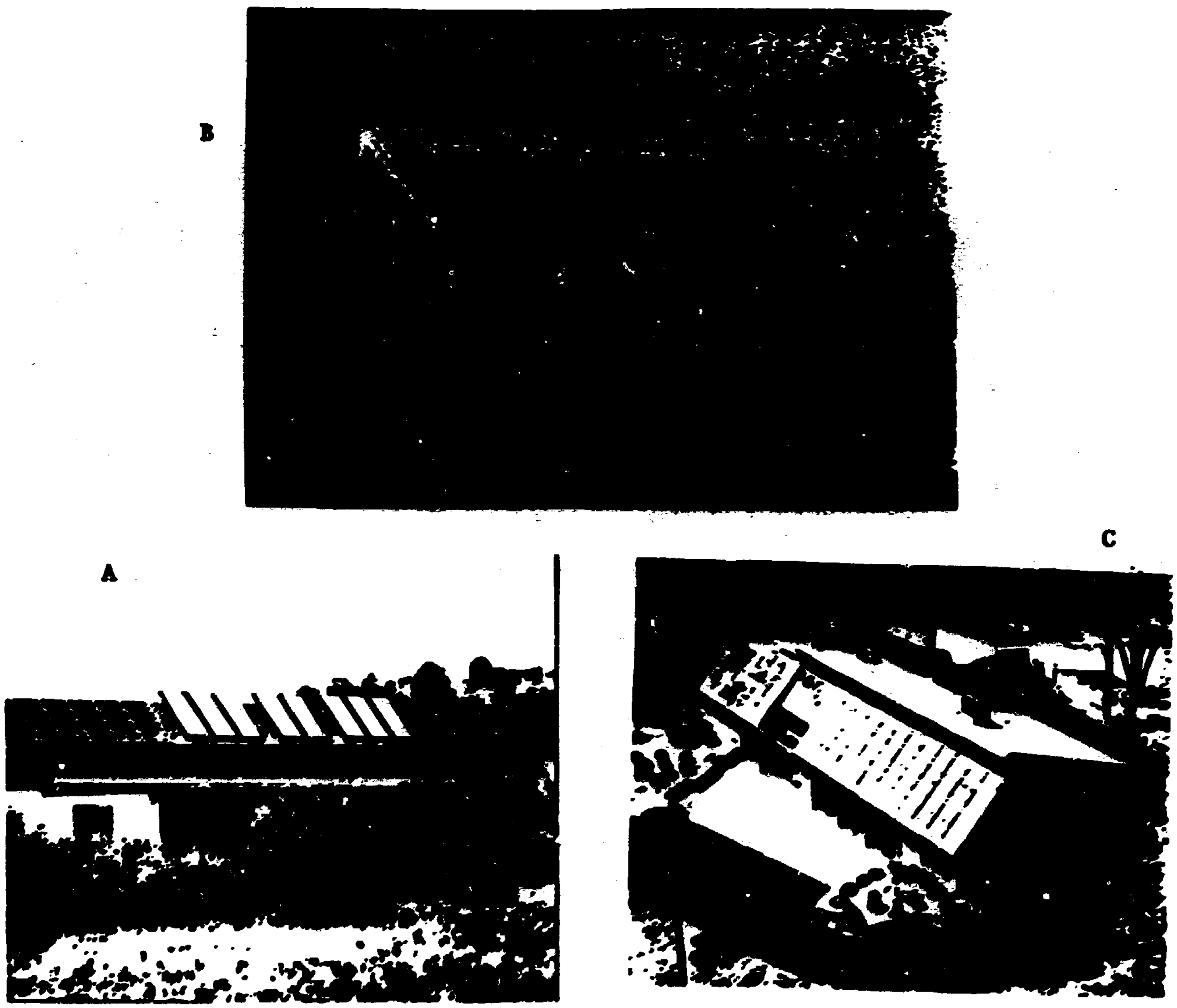

Figure 77: Remote solar home by Kyocera International, Inc. (A); desalination to produce drinking water in Jeddah, Saudi Arabia, using Mobile Solar Ribbons, (B), and Carlisle House in Massachusetts with 7.3 kW solar roof panels, feeding excess power into the utility grid.

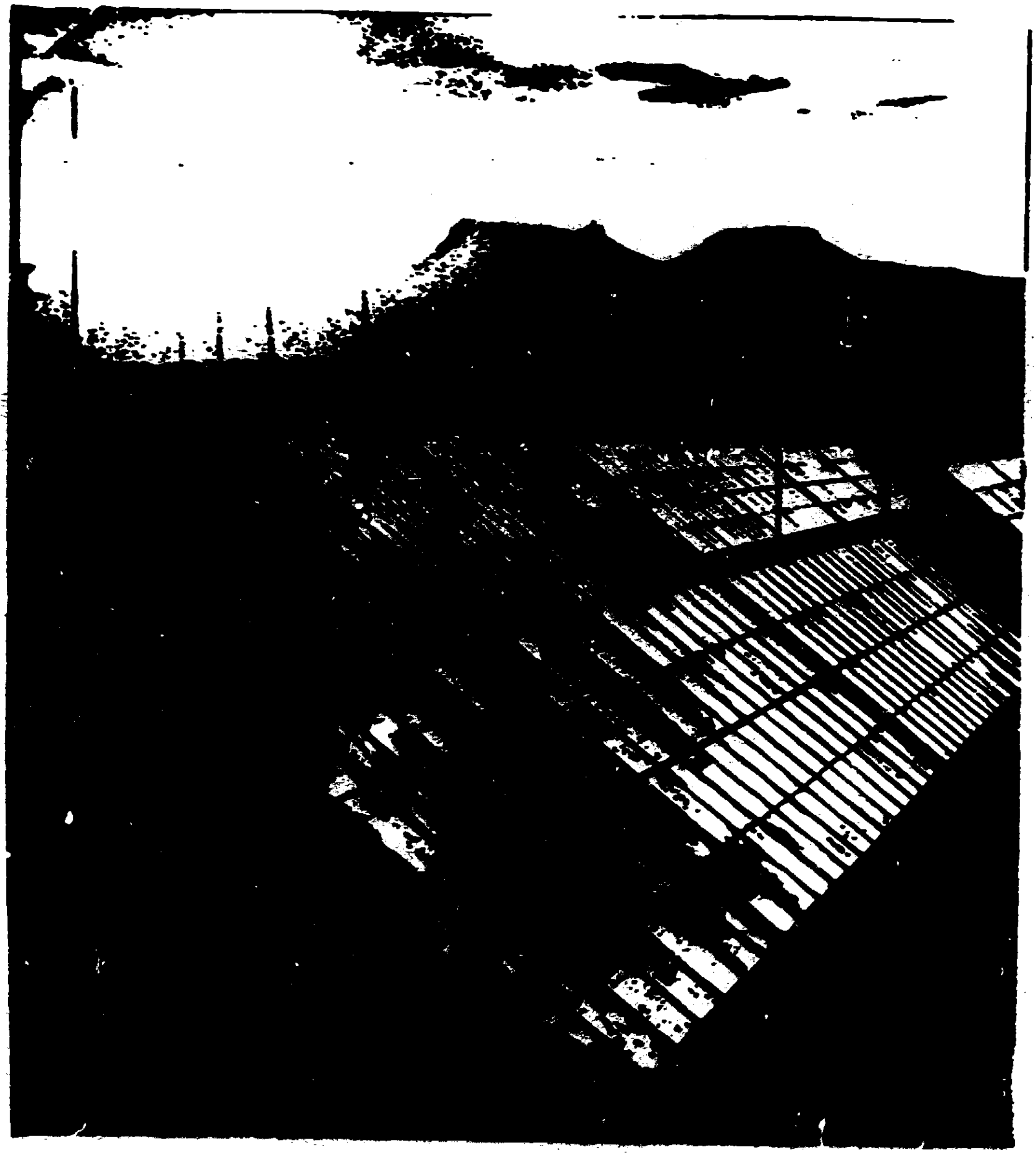

Figure 78: Stand alone power station by Solarex.

Figure 79: Mirror assisted 6.5 MW collection system for the Southern California Edison Co. power utility at Carisa, California, with 11% module efficiency (ARCO Solar).

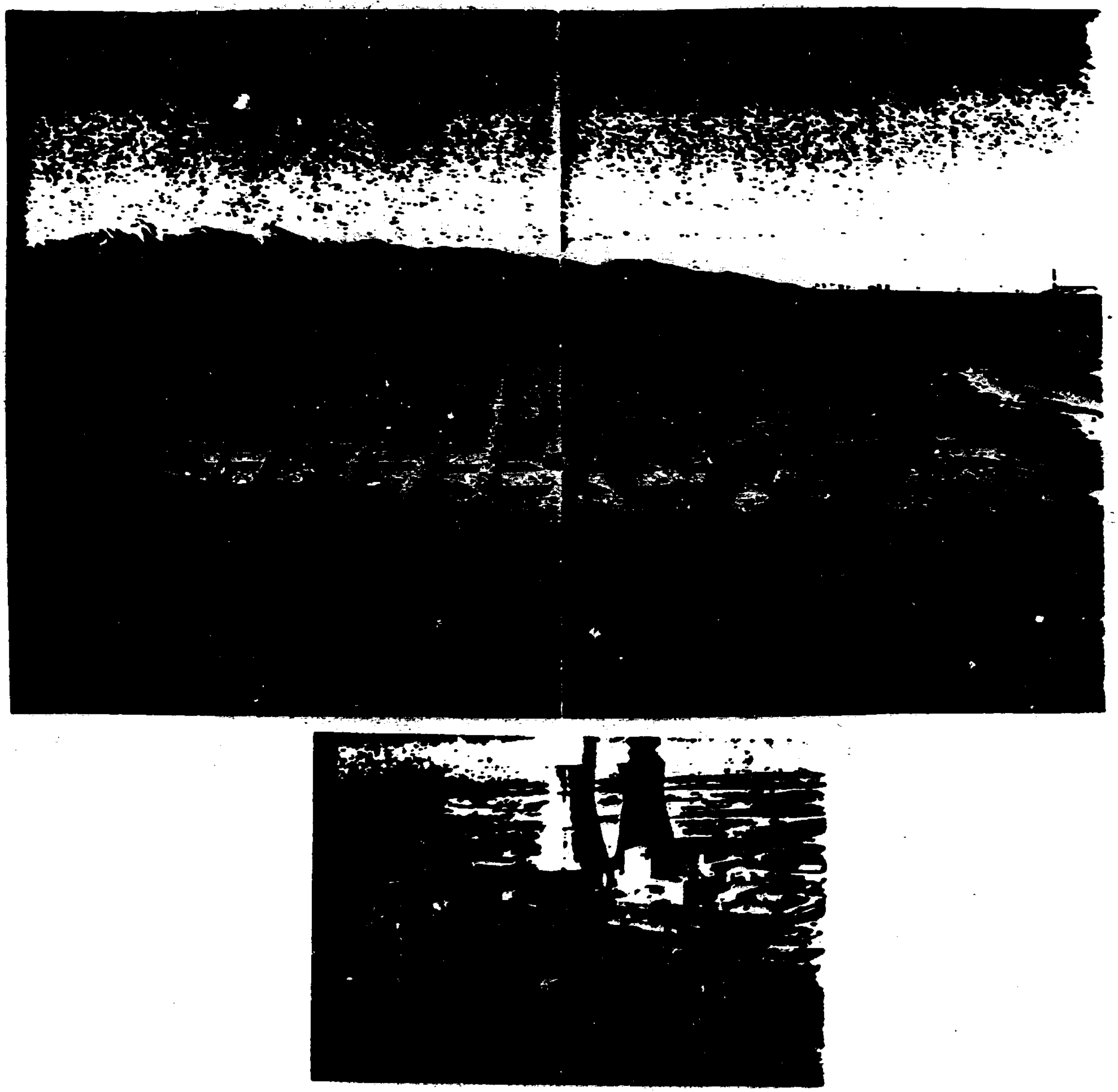

Figure 80: 1 megawatt power utility installation for the Southern California Edison Co. in Lugo, California (A) (two axis tracking) and the now operating 2 megawatt plant for the Sacramento Municipal Utility District (SMUD) (B), both by ARCO Solar.

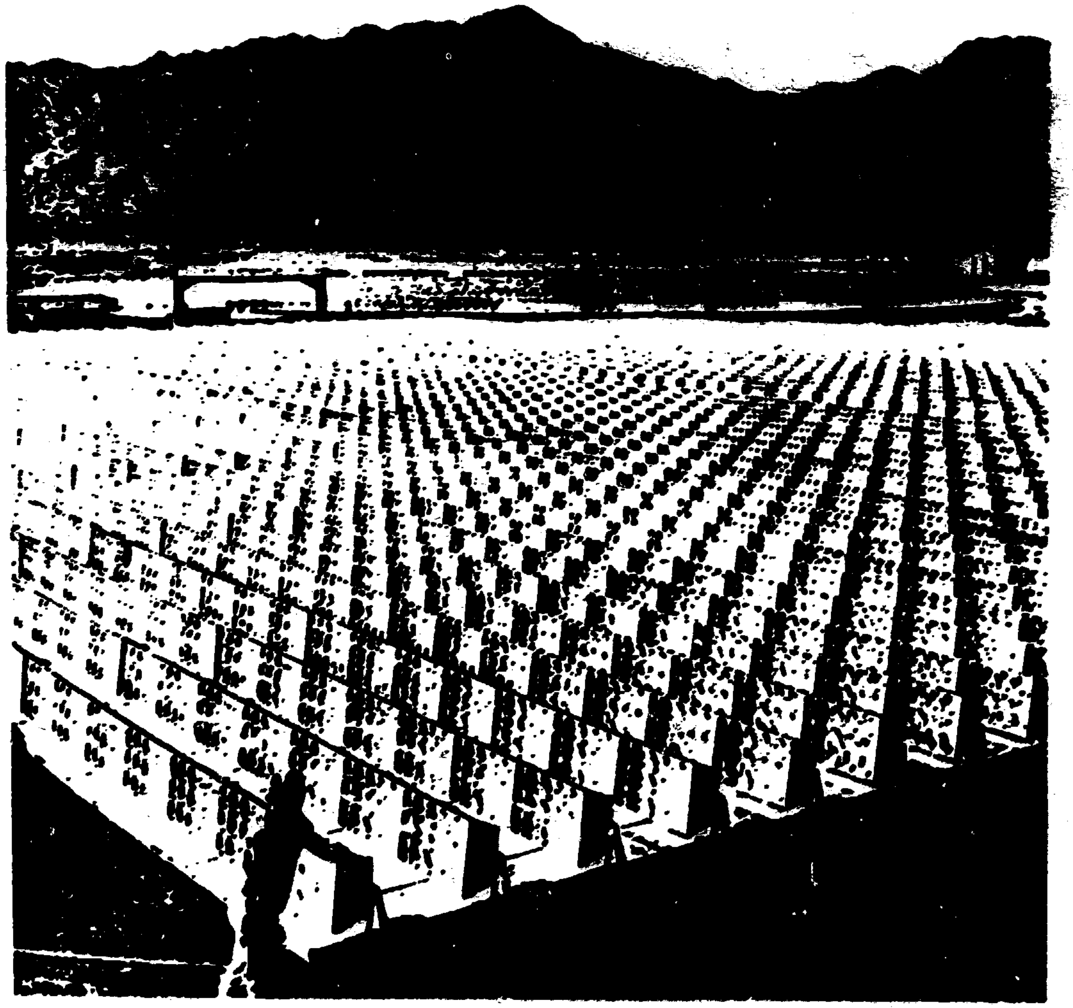

Figure 81: Example for a concentration deployment at the Energy farm in Borrero Springs desert (al.) providing heat and electricity for an ethanol plant (United Energy Corp.)

Figure 82: Amorton experimental housing (Japan).

Solarex modules provide 300 kW of power for Georgetown University's Intercultural Center in Washington, D.C.

Figure 33: Commercial building installation at Georgetown University, USA, using Solarex Modules).

6 Long Term Projections and Prospects for Developing Countries

From the preceding discussion summarizing the present achievement, it is evident that the technology has arrived at a point in the learning curve that makes it virtually certain that even without external pressure the photovoltaic alternative to large scale electric energy production will become reality. Even competing with the very low cost central power utility market, photovoltaic cogeneration is less than a factor of 5 away from an unassisted entry, compared to a factor of 100 a little more than a decade ago.

There are sufficient interim markets to bridge the way to the final goal, so that a relatively smooth progress could be predicted. In addition, there are external pressures from environmental aspects, ranging from nuclear risks to the simply unacceptable danger of doubling the CO_2 content of our atmosphere, which will force us to limit the burning of fossil fuels within the next two decades.

The question arises, however, if sufficient time and resources are available to guarantee an orderly and timely development of the technology. Compared to the high technology of the early solid state diodes and transistors, the technology of highly efficient inexpensive and long lasting solar cells may be coined as *ultrahigh technology*. With all the knowledge acquired we still are lacking some of the most basic parts in the puzzle to predict with near certainty which material to choose, which process to apply, which design to select to produce such a desirable cell for the solar panels of the next century. We recognize some of the handicaps of the present technology as being acceptable, and we can live with them, but, looking ahead our research efforts mirror the intense desire to achieve still another breakthrough.

It is the hope for such a breakthrough which at the same time instills hesitation for large investments into critical size factories which may be outdated before amortized in the necessarily slow interim markets.

Assistance is therefore essential to proceed with research and development. This assistance, if not provided at sufficient levels, can be crucial for possibly failing to form the basis for a healthy world economy which is based to a large extent on energy, and without doubt will have to be based on solar cell technology in the next century.

The goal to achieve the entry into the solar cell large scale energy technology is a goal which is equally important for all nations. Contributions to achieve this goal can be made by many means, whether it is passive by learning how to use this technology as a consumer, or active by researching new cells or by educating the necessary cadres. It will have to become a political movement which will involve all of us, the population of this globe, as consumers, as educators, as economists, as technologists, as researchers. It is almost too late now, since we know that the introduction of a new energy technology takes close to half a century. But knowing that the needs are undisputed and the penalties of not acting promptly will not only be very severe for our children, but as severe in our lifetime, we must convince all of us to step forward and to accept the greatest challenge for humankind yet, namely to bring swiftly to reality the economical utilization of solar cells for major electric power generation.

7 References

1. Smith, W., Nature (London) 7, 303 (1973).
2. Rappoport, P., Phys. Rev. 96, 246 (1954);

   Chapin, D. M., C. S. Fuller and G. L. Pearson, J. Appl. Phys. 25, 676 (1954);

   Prince, M. B., J. Appl. Phys. 26, 534 (1955);

   Rappoport, P., J. J. Loferski and E. G. Lindner 17, 100 (1956).
3. Reynolds, D. C., G. Leies, L. L. Antes and R. E. Marburger, Phys. Rev. 96, 533 (1954);

   Reynolds, D. C. and S. J. Czyzak, Phys. Rev. 96, 1705 (1954).
4. Wolf, M., Proc. 25th Power Source Symp., 120-124 (1972).
5. Shiozawa, L. R., G. A. Sullivan, and F. Augustine, 7th IEEE Photovoltaic Spec. Conf., 30-46 (1968).
6. Solar Cells, *Outlook for Improved Efficiencies*, Nat. Acad. Sci., Washington, D.C. (1972).
7. Proceedings of the 18th IEEE Photovoltaic Spec. Conf. (1985) and of the 7th SERI R & D Review Meeting, May 1986.
8. Fahrenbruch, A. L. and R. H. Bube, *Fundamentals of Solar Cells*, Academic Press, New York (1983).
9. Loferski, J. J., J. Appl. Phys. 27, 777 (1956).
10. Wolf, M., Energy Conversion 11, 63 (1971).
11. Christensen, E., *Flat Plate Solar Array Project*, 10 Years Progress, DOE, JPL, NASA, Oct. 1985.
12. Devaney, W. E., R. A. Michelsen and W. S. Chen, Proc. 18th IEEE Photovolt. Spec. Conf., 1733 (1985).
13. Cusano, D. A., Solid State Electr. 6, 217 (1963).
14. E.Spenke, *Electronic Semiconductors*, McGraw Hill Book Co., New York (1958).
15. Böer, K. W., J. Crystal Growth 59, 111 (1982).
16. Fonash, S. J., *Solar Cell Device Physics*, Academic Press, New York (1981).
17. Böer, K. W., J. Solar Energy 19, p.525 (1977).
18. Böer, K. W., phys. stat. sol. (a) 87, 719 (1985).
19. Böer, K. W., phys. stat. sol. (a) 66, 11 (1981).
20. Böer, K. W., phys. stat. sol. 40, 355 (1977).
21. Ali, A. Y. and K. W. Böer, Proc. 18th IEEE Photovolt. Spec. Conf. (1985).
22. Böer, K. W., Phys. Stat. Sol. (a) 62, K1 (1980).

23. Wolf, M., 18th IEEE Photovolt. Spec. Conf., p.33 (1985).

24. Spitzer, M. B. and C. J. Keavney, 18th IEEE Photovolt. Spec. Conf., p.43 (1985).

25. Iles, P. A., Proc. 9th IEEE Photovolt. Spec. Conf., 1-5 (1972).

26. Lindmayer, J. and J. F. Allison, Comsat. Techn. Rev. 3, 1 (1973).

27. Arndt, R. A., J. F. Allison, J. G. Haynos and A. Meulenberg, Jr., Proc. 11th IEEE Photovolt. Spec. Conf., p.40 (1975).

28. Green, M. A., et. al., Proc. 17th Photovolt. Conf., p.386 (1984) and Proc. 18th Photovolt. Spec. Conf. (in print) (1985).

29. Suiton, R. A., Y. Kwark, P. Gruenbaum and R. M. Swanson, Proc. 18th IEEE Photovolt. Spec. Conf. (1985), p.61 and recent communications.

30. Lammert, and Schwarz, Techn. Rep. TR-EE 75-37, Purdue University (1975).

31. Swanson, R. M., 18th IEEE Photovolt. Spec. Conf., p.604 (1985).

32. Sinton, R. A. et al., 18th IEEE Photovolt. Spec. Conf., p.61, (1985).

33. Böer, K. W. in *Solar Energy Handbook*, W. C. Dickinson and P. N. Chererisonoff, Eds., Marcel Dekker, Inc., New York (1978), Chapter 3.

34. Shockley, W. and H. J. Queisser, J. Appl. Phys. 32, 510 (1961).

35. Wolf, M., Energy Conversion 11, 63 (1971).

36. Johnson, J. E. et al., 18th IEEE Photovolt. Spec. Conf., p.1112 (1985).

37. Rohatgi, A. et al., 18th IEEE Photovolt. Spec. Conf. (1985), p.50.

38. Ravi, K. V. et al., 18th IEEE Photovolt. Spec. Conf., p.1222 (1985).

39. Uno, F. M. et al., 18th IEEE Photovolt. Spec. Conf., p.968 (1985).

40. Rohatgi, A. et al., 18th IEEE Photovolt. Spec. Conf., p.782 (1985).

41. Maycock, P. D. and E. N. STirewalt, *Photovoltaic Revolution*, Rodale Prewss, Emmanus, PA (1985).

42. Hamakawa, Y., in *Tetrahedrically-Bonded Amorphous Semiconductors*, ed. D. Adler and H. Fritzsche, Plenum Publ. Co., New York (1985).

43. Spear, W. E. and P. G. LeComber, Solid State Com. 17, 1193 (1975).

44. Madan, A., S. R. Ovshinski and E. Benn, Phil. Mag. B40, 259 (1979).

45. Hanak, J. J., 18th IEEE Photovolt. Spec. Conf., p.89 (1985).

46. Arya, R. R., 18th IEEE Photovolt. Spec. Conf., p.1710 (1985).

47. Carlson, D. E. and C. R. Wronski, Appl. Phys. Lett. 28, 671 (1976).

48. Catalano, T., A. Priester and B. Fangham, Proc. 16th IEEE Photovolt. Spec. Conf., 1421 (1982).

49. Nakano, S. et al., Techn. Digest of Internat'l. PVSE Conf., Kobe, Japan, 583 (1984).

50. Yang, J. et al., 18th IEEE Photovolt. Spec. Conf., p.1519 (1985).

51. Okinawa, H. et al., Proc. 16th IEEE Photovolt. Spec. Conf., 1111 (1982).

52. Okuda, K., H. Okamoto and Y. Hamakawa, Jpn. J. Appl. Phys. 22, L605 (1983).

53. Yablonovitchi, E. and G. D. Cody, IEEE Trans. El. Dev. ED-29, 300 (1982).

54. Staebler, D. L. and C. R. Wronski, J. Appl. Phys. 51, 3262 (1980).

55. Nakano, S. et al., Proc. 16th IEEE Photovolt. Spec. Conf., 1124 (1982).

56. Carlson, D. E., R. W. Smith, P. J. Zanzucchi and W. R. Frenchu, Proc. 16th IEEE Photovolt. Spec. Conf., 1372 (1982).

57. Ullal, H. S., et al., 17th IEEE Photovolt. Spec. Conf., 359 (1984).

58. Adler, D., J. Phys. 42 Suppl. 10, C4-3 (1981) and Solar Cells 9, 133 (1983).

59. Dalal, V. L., Proc. 17th IEEE Photovolt. Spec. Conf., 86 (1984).

60. Ovshinski, S. R., Proc. 18th IEEE Photovolt. Spec. Conf. (1985).

61. Nakamura, G. et al., J. Non-Cryst. Solids 59-60, 1111 (1983).

62. Tanner, D. P. et al., 18th IEEE Photovolt. Spec. Conf., p.1301 (1985).

63. Mitchell, K. W. et al., 18th IEEE Photovolt. Spec. Conf., p.1359 (1985).

64. Yamagishi, H. et al., 18th IEEE Photovolt. Spec. Conf., p.1573 (1985).

65. McMahon, T. J. and Xi, 18th IEEE Photovolt. Spec. Conf., p.1579 (1985).

66. Bennett, M. S., 18th IEEE Photovolt. Spec. Conf., p.1584 (1985).

67. Kobe, T. et al., 18th IEEE Photovolt. Spec. Conf., p.1586 (1985).

68. Hack, M. and M. Shur, 18th IEEE Photovolt. Spec. Conf., p.1588 (1985).

69. Catalano, T. et al., 18th IEEE Photovolt. Spec. Conf., p.1378 (1985).

70. Plättner, R. et al., 18th IEEE Photovolt. Spec. Conf., p.1596 (1985).

71. Tawada, Y. et al., 18th IEEE Photovolt. Spec. Conf., p.1712 (1985).

72. Sabiski, E., H. Mahan and T. McMahon, 16th IEEE Photovolt. Spec. Conf., 1106 (1982).

73. Sabisky, E. et al., 18th IEEE Photovolt. Spec. Conf., p.474 (1985).

74. Chang, K. I. et al., 18th IEEE Photovolt. Spec. Conf., p.122 (1985).

75. Hamaker, H. C. et al., 18th IEEE Photovolt. Spec. Conf., p.327 (1985).

76. Edenburn, M. W. and E. C. Boes, Proc. 17th Photovolt. Spec. Conf., 473 (1984).

77. Hamaker, H. C., et al., Proc. 18th IEEE Photovolt. Spec. Conf. (1985).